12-31-2007

Optimization of optical computed tomography techniques for the synthesis of particle aggregate models

Patrick Anthony Giordano Jr.
Rowan University

Optimization of Optical Computed Tomography Techniques for the Synthesis of Particle Aggregate Models

by

Patrick Anthony Giordano Jr.

A Thesis Submitted to the

Graduate Faculty in Partial Fulfillment of the

Requirements for the Degree of

MASTER OF SCIENCE

Department: Electrical and Computer Engineering

Major: Engineering (Electrical Engineering)

Approved:

Members of the Committee

_____

In Charge of Major Work

_____

_____

For the Major Department

_____

For the College

Rowan University
Glassboro, New Jersey

ABSTRACT

Patrick A. Giordano Jr.
OPTIMIZATION OF OPTICAL COMPUTED TOMOGRAPHY TECHNIQUES FOR THE SYNTHESIS OF PARTICLE AGGERGATE MODELS
2007/08
Dr. Shreekanth Mandayam
Master of Science in Engineering (Specialization in Electrical Engineering)

The characterization of 3-D shapes of particles in geomaterial aggregate mixtures is important for understanding the micro-mechanics of granular materials. Also, numerical synthesis of 3-D particle shapes from their corresponding shape descriptors is required for developing discrete element models (DEMs) that can be used to predict particle contact-forces, and ultimately the shear strength of the aggregate mixture.

Previous work has shown that Fourier-based 3-D shape descriptors can be constructed for aggregate mixtures, using a statistical combination of 2-D projections. Furthermore, optical tomography methods using the Algebraic Reconstruction Technique (ART) algorithm has proved capable of synthesizing 3-D shapes from 2-D projections, with accuracy comparable to that obtained by an X-ray microtomograph (the "gold" standard).

This thesis extends and revalidates prior work using images obtained from a larger set of geomaterial mixtures – an extensive sand database has been constructed. Inexpensive optical microscopy methods for synthesizing composite 3-D shapes representative of the entire mixture using multiple 2-D images of particles scattered on an image plane, is explored. An optimization technique based on the Euclidean distance

metric has been developed for selecting a subset of such 2-D images for synthesis using the ART algorithm. Results demonstrating the success of this technique are shown to depend on the statistics of the particle mixtures. The algorithm is successful in synthesizing particles similar in shape to the optical and X-ray tomography methods for those aggregate mixtures with fairly homogeneous shapes.

ACKNOWLEDGEMENTS

I would like to thank Dr. Shreekanth Mandayam for the opportunity to work on this project. It has been a fun and academically challenging journey for which he has guided me, and for that I will always be thankful. I would like to thank Dr. Sukumaran and Dr. Polikar for taking time out of their busy schedules to be a part of my committee, their help and guidance has provided me with the necessary tools not only to complete my graduate work, but to make me a better engineer.

I want to thank my parents for their guidance and patience throughout my life. Their love and pride gave me the drive to do my very best and I would not be where I'm today without them. I want like to thank my family and friends for always being supportive and inquisitive about my work, willing to help at every twist and turn. I would also like to thank all those that have helped and assisted me with this project; Phil Mease, Dan Barrot, George Lecakes and Kevin Garrison. My thanks go to the National Science Foundation (Award Numbers 0421000 and 0324437) for their support, in making this project possible.

TABLE OF CONTENTS

LIST OF FIGURES

LIST OF TABLES

CHAPTER 1 : INTRODUCTION

The task of shape characterization can either be simple or difficult given the complexity of the shape. The most common shapes such as the circle, square, and triangle can be easily described. All that is needed to describe the shape is its name, and there will be adequate information to recreate that shape. It is possible to observe, for example, a square with a given length of 10 cm. With the added information about the length of one of the sides of the square and a priori information that all sides in a square are the same length, all the information required to specifically describe the observed shape is known. The problem lies however, when the shape falls outside of those commonly known. As the complexity increases, it becomes only possible to describe the shape as an "n-sided" polygon. At this point, it becomes impossible to be able to accurately describe the shape by a name alone. Take for example a square; the name by itself carries adequate information to describe its shape, whereas with the case of an "n-sided" polygon, there are an infinite number of possibilities, hence, "n-sided."

One method to describe an arbitrarily complex shape would be to create a set of numbers that can describe the boundary of the shape. This could be a simple task where the length and angle of each part of the shapes boundary is found and used to describe itself, or complex where there is a way to relate features using a smaller set of numbers. A set of numbers offers a quantitative way to examine shape characteristics and allows for the use of computers to quantify the results. These numbers can be used as the descriptors, which describe the overall shape of the object. From these descriptors it is also possible to track the trends that would allow for "rounder" shapes to be placed in a different group then those shapes that may be more "angular".

1.1 Applications involving shape characterization

The significance of shape characterization can be effectively seen in the law enforcement community, where the proper classification of fingerprints can be the difference in proving guilt or innocence. Another application includes facial recognition, where a person's face is digitally mapped so that a computer will be able to correctly distinguish one person from another. This can be done in many ways, for instance, a person's distance between eyes can be measured or the roundness of their face can all be used as descriptors. However, the goal is to choose descriptors whose values are different for every person that the system could ever see.

An area of application for civil engineering is in the characterization of geomaterial aggregates. The properties of a particular soil are affected by the shape characteristics of the thousands of particles in the soil. The size and shape of these sand particles determine the interaction behaviors of the mixture. This can affect the load characteristics of the particles as well as the flow characteristics.

1.2 Motivation

The requisite for an automated shape description system is generally found in applications using computer vision. Most of the work in this area has focused on 2-D shape characterization.

The focus of this thesis is built upon describing the 3-D shapes of particle aggregate mixtures, particularly sand particles. The geomaterial properties of a particular soil are affected by the shape characteristics of sand grains of that soil. The size and

shape of these sand particles determine the interparticle interaction of the mixture. This can affect the load as well as the flow characteristics of the particles. There are three major categories that affect the stress and strain behavior of different soil mixtures; inherent particle characteristics, geology and environmental factors [1]. This is depicted in Figure 1-1.

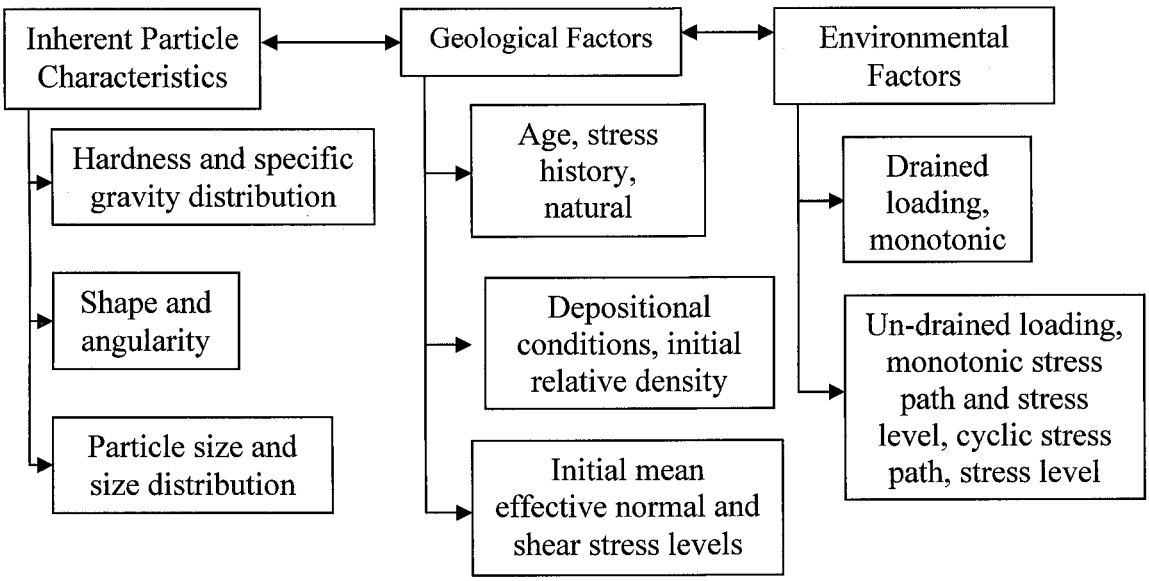

Figure 1-1: Factors affecting the stress-strain behavior of soil [1].

These factors can then be quantified for deeper analysis by using standard techniques readily used in practice. One such example is sieve analysis which is a device used to calculate the particle size as well as the size distribution of the mixture. The process begins with the soil being placed on a mesh screen and is sifted such that the soil with a size smaller than the mesh will fall through. These particles are then sifted again using a finer mesh until the lowest level of desired measurement is achieved. During this process the mass retained on each of the aforementioned mesh grids is recorded. The measurement of specific gravity distribution can also be measured using water displacement techniques.

The friction angle, also known as the particle to particle interaction inside a mixture, is solely affected by the shape of the sand particles. Friction angles are crucial to the understanding of the properties of soils because there is a direct correlation between them and the overall strength of the mixture. One of the most important pieces of information about a particle mixture is the overall minimum and maximum void ratios. Void ratios can be described as the space present when a load is placed on a mixture of particles, which is highly dependent on the shape characteristics of the particles [1]. When analyzed, more jagged sands will yield higher shear strength than a mixture whose characteristics are more rounded in nature.

The shape and angularity of a particle has yet to be effectively described mathematically. There are two current methods used to solve this problem, radius expansion and spherical harmonics. However, these techniques are only useful for characterizing the 2-D boundaries. Qualitatively, the relationship between shear strength and shape exists, however quantification of shape parameters would allow for a better relationship to be obtained. Once the ability for particle reconstruction in 3-D is made more readily possible, more detailed models can be obtained for observing the inter particle microstructure interaction, which will ultimately lead to better models for predicting the shear strength of a particle mixture.

The major difficulty lies in the fact that finding valid data which describes the 3-D characteristics of a mixture is non-trivial and very arduous. One of the current methods involves using optical microscopy; however, these models can only be used reliably for charting behavior trends due to the high level of inaccuracy [2]. For the highest level of accuracy it is essential to achieve a reliable 3-D model. This is in practice done with

expensive equipment such as an X-ray tomography system. In Figure 1-2 an X-ray tomographic reconstruction of a single particle of Melt sand can be observed. One of the noticeable features of this particle is the extremely high level of detail in the final reconstructed model. This high level of detail comes at the cost of an even higher level of computational complexity which can range from one to five hours, and this is only for the scanning phase.

Figure 1-2: X-ray tomographic reconstruction of a single particle of Melt sand.

The notion of describing 3-D shapes by finding a set of shape numbers is far from a trivial task. When we discuss the objects that we wish to model in 3-D, we are looking at the non-trivial, flat and continuous, but in fact, complex objects which exist in not only for the x and y axis, but in the z-axis as well. This makes the collection of points necessary for the objects reconstruction very difficult due to the immense volume of coordinates. Directly reconstructing the 3-D particles is impractical when thousands of particles from the different soil mixtures are needed such that the mixture can be accurately characterized. To circumvent this growing complexity it is necessary to find a practical and reliable 2-D solution for this problem. The equipment for this procedure is relatively inexpensive when compared to a tomographic X-ray imaging system, and

would only consist of and optical microscope and digital camera. This practical and reliable 2-D technique must also be able to find distinct numerical descriptors which can characterize the different shapes of sand, as well as be able to accurately reconstruct the original particle mathematically. The optical tomography approach to solving this 3-D problem will allow for massive particle synthesis with very low computational complexity and hardware costs.

1.3 Objectives, scope, and organization

The goal of this thesis is to develop techniques for the synthesis of particle aggregates using algebraic reconstruction techniques from images obtained using optical microscopy. This work is intended to demonstrate measurable improvement, compared to previous work, in shape characterization for particle aggregates. Specifically, the research objectives are to:

1. Design and develop automated optical 3-D tomography system, for the shape characterization of particle aggregates.
2. Design and develop experimental protocols and databases of optical and X-ray tomography scans of a set of geomaterial aggregate mixtures.
3. Demonstrate the ability of the optical microscopy techniques to reconstruct 3-D shapes.
4. Demonstrate the consistency, separability and uniqueness of the 3-D shape-descriptor algorithm by exercising the method on a varying set of particle aggregate mixtures.

The reconstruction algorithm, validated in previous research was done so using four aggregate mixtures, which were scanned on the optical and X-ray tomography system and will be used to further refine the premise of particle synthesis using random images drawn from a mixture such that it can be validated.

This thesis is organized as follows. Chapter 1 describes the problems associated with 3-D shape description and the specific application for geomaterial aggregates. Chapter 2 discusses the method used for sand particle characterization and common tomographic reconstruction techniques for 3-D objects. Chapter 3 describes the use of a correlation metric based on the Euclidean distance to enable the 3-D reconstruction algorithm, which was developed for the single particle case and verified using the X-ray tomographic scanner, to have the ability to create specific, separable composite models for each of the aggregate mixtures. Chapter 4 contains the results of the synthesized composite models using the 3-D characterization and reconstruction algorithms, on images drawn from a collection of different particles of sand from the same mixture. The experimental setups are also described in this chapter as well as further refinements. Chapter 5 has a summary of accomplishments and recommendations for future work and is the conclusion of this thesis.

1.4 Expected contributions

A comprehensive database of the 3-D shapes of 7 aggregate mixtures, obtained from X-ray and optical tomography methods will be developed. It is also expected that an optical and X-ray tomography system be designed and optimized for automation under a specific set of protocols. This thesis will also address the issues that arise from the optical

tomography reconstruction of multiple facets of multiple images, so that synthesis of 3-D particles can further be optimized to the point where statistical manipulation of the numerical shape descriptors can be used to synthesize composite models.

CHAPTER 2 : BACKGROUND

In order to be effective, shape description techniques must possess the following qualities' [3].

Uniqueness:

The algorithm must be able to distinguish between different shapes. This is done by assigning a set of numbers which are unique to each shape.

Parsimony:

The algorithm should use the smallest possible set of numbers to describe a particular shape. This will reduce the descriptor values overall noise susceptibility.

Independence:

Each descriptor should be independent of the next. One descriptor should not be based on the outcome of another.

Invariance:

The descriptors should not be dependent upon the orientation of the shape. Similar shapes should have similar descriptors even if they are rotated, translated, or scaled versions of themselves.

For most applications a good method will encompass the four qualities listed above. There are however, certain cases for which invariance is not important. Such a case would be when identification is necessary of the orientation of a shape. For the 2-D shape characterization technique, attempts are made such that the four listed qualities are

achieved, where possible. The following three qualities enhance the overall robustness of the technique [3].

Reconstruction:

The collected descriptors can be used to reconstruct a shape, as well as possibly reducing the overall amount of data necessary for storage and processing purposes.

Interpretation:

This is the amount of physical relationship between the descriptor and the actual shape [4]. Here it is possible to see if certain values of the descriptors lead to different shape characteristics when used for reconstruction.

Automatic Collection:

Lends to the algorithm's ability to automatically collect and analyze data for external and internal processing procedures. This will also lead to less if any human error and ultimately makes processing faster [4].

2.1 Previous work

The majority of the previous work in this field of 2-D shape descriptions has been summarized in the following Table 2-1

Table 2-1: Summary of previous techniques used in shape description.

Proponents	Method	Explanation	Application
Wentworth [5]	Elongation and flatness, roundness of sharp corners	One of the first to characterize form and roundness. Opened the field for many of the subsequent studies	Used a variety of sand types including, conglomerate, breccia, and sandstone

Wadell [5]	Sphericity	First method developed to measure the sphericity of a particle to characterize its form	Wadell attempted to quantify the shape of quartz particles
Sebestyn and Benson [3]	"unrolling" a closed outline	The concept of creating a 1-D function from a 2-D boundary. Introduced by Benson into the field of geology.	Benson introduced this concept to geology using a paleontology application
Ehrlich and Weinberg [6]	Radius expansion	Introduced Fourier analysis for radius expansion into sedimentology.	Used a range of particles from smooth to very angular
Medalia [3]	Equivalent ellipses	Fits an ellipse to have similar properties to the actual shape. Does not need outline.	Tested on carbon black aggregates for both 2-D and 3-D
Davis and Dexter [3]	Chord to perimeter	Measures chord lengths between various points along an outline.	Measured irregularities of many soils
Zahn and Roskies [3]	Angular bend	Zahn and Roskies discretized an outline into a series of straight lines and angles	Developed method using arbitrary closed curved shapes.
Garboczi, Martys, Saleh, and Livingston [7,8]	Spherical harmonics	A process similar to 3-D Fourier analysis, and requires 3-D information.	Applied to aggregates used in concrete captured using X-Rays
Sukumaran and Ashmawy [9]	Shape and angularity factor	Compares shapes to circles and measures their deviation. Uses a mean and standard deviation of many particles to compare mixes.	Algorithms applied to various types including Michigan Dune, Daytona Beach and a few kinds of Ottawa.
Corriveau [4]	3D shape characterization using multiple projective representations	Determines 1D Fourier Transforms of the boundaries of multiple projections of a 3D shape to generate statistical 3D shape descriptors.	Algorithm applied to various sand types such as Michigan Dune, Daytona Beach, #1 Dry and Standard Melt

Barrot [10]	3D Shape reconstruction from single particle multiple projective representations	An algebraic reconstruction technique (ART) for the synthesis of three-dimensional models of particle aggregates from projective representations	Algorithm applied to Michigan Dune, Daytona Beach, #1 Dry, Standard Melt, Kahala Beach, Ala Wai, Rhode Island sand aggergates

The subsequent section will illustrate in further detail the 2-D techniques from Table 2-1. These techniques only require images from an optical microscope for processing. Two methods from this section were implemented in the 3-D shape characterization technique described by [4]. Sections 2.3-2.6 contain an explanation of a pair of techniques used for obtaining 3-D shape descriptors from 3-D data, the technique for 3D shape characterization for particle aggregates using multiple projective representations described in [10].

2.2 2-D shape description techniques

There are two categories of shape description techniques; the first is boundary description, where the "edge" or boundary is used to describe the shape of the particle. For this to be successful the boundary must first be transformed generally into a 1-D function by using a technique such as "unrolling". The other category involves a technique which attempts to describe the shape by its planar surface, but, the entire image must maintain orientation invariance for this case to be valid [3]. The following sections will describe both the boundary and planar techniques of shape description.

2.2.1 Boundary techniques

Boundary shape description techniques can be disassembled into two main sub categories; Fourier analysis techniques and distributional techniques. The Fourier analysis technique involves converting the boundary into a periodic function so that the transform can be applied. When this condition is met, the technique then will allow for reconstruction through the inverse Fourier transform property, as well as data compression through the exclusion of the high frequency values that correspond to the fine detail of the shape. As long as the low frequency values containing the general shape information are stored, Fourier analysis can be a parsimonious, effective shape description technique that offers reconstruction, not available to simpler generic shape description techniques. In the following Figure 2-1, the concept of retaining the low frequencies while excluding the high frequency detail information is illustrated.

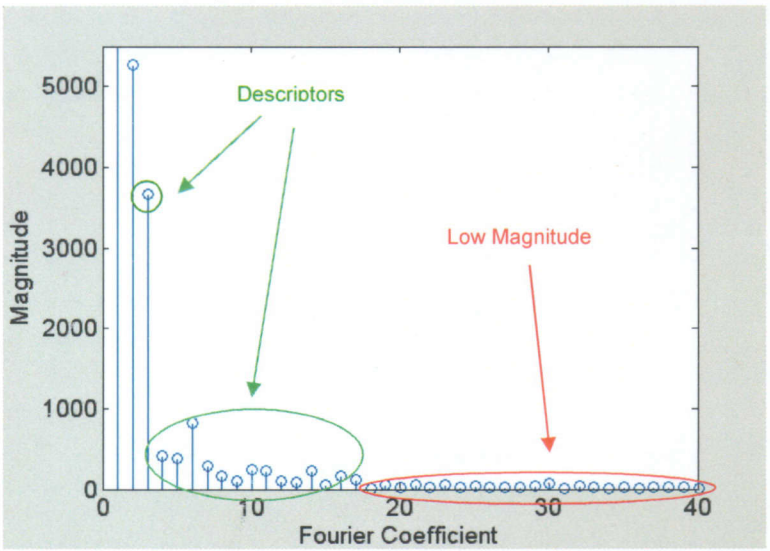

Figure 2-1: Fourier analysis with resulting descriptors.

Distributional approaches do not inherently allow reconstruction, but are often more invariant to orientation, since they are not concerned about the sequence of the boundary. Also the distributional approaches are usually more statistically friendly proving more useful for such cases. The rest of this section will describe the boundary description methods and then offer possible Fourier or distributional analyses that could be done amid them.

2.2.1.1 Radius expansion

A common technique used for describing the boundary of a shape is radius expansion. The radius expansion method attempts to describe the shape by first finding the centriod of the object, and then traversing the border at specified angles, all the while calculating the distances to the border [3, 11], and can be seen in Figure 2-2. The distance can be calculated in polar coordinates, first at zero degrees, and then continually checked at certain degree intervals all around the border. The number of degrees between each point observed decides the resolution of this technique.

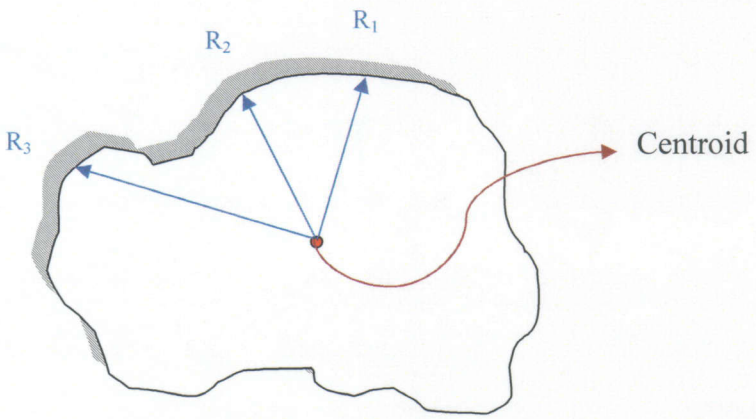

Figure 2-2: Illustration of radius expansion.

Once all of the points are gathered, using a set angle, a periodic function can then be created and further analyzed. The problem lies, innately in the shape that is being analyzed, specifically when two or more values exist for a specific angle [5] which is illustrated in Figure 2-3.

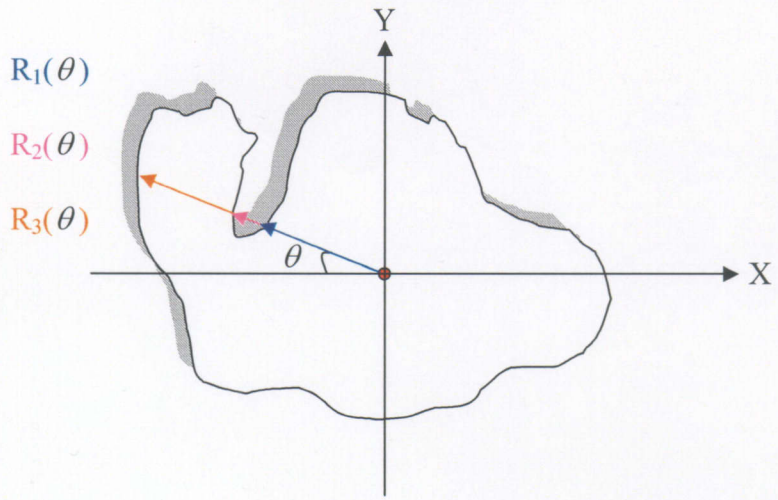

Figure 2-3: Multiple valued radius expansion solution.

Since the methods' end result is a periodic function, the Fourier series analysis can be performed effectively. A distributional approach may be used as well, such as finding a radius histogram of the shape. This distribution tracks how many times certain radius ranges occur, but fails to include the angles at which they take place, therefore, would not be usable for reconstructing the. Another disadvantage is that two dissimilar shapes may have similar distributions. Take for instance, a star and a kidney shape. Although they are visually very different, they both have many large and small

amplitudes and could appear to be the same object when only comparing their radius distributions.

2.2.1.2 Angular bend

Angular bend is another method that can be utilized by the Fourier and distribution analyses. Firstly, a point is chosen on the boundary as well as the step size utilized to step to the next point. The angle that separates the two discrete points is then recorded until the entire boundary has been measured allowing for reconstruction using Fourier series. The only difference from the radius expansion technique thus far is that compression is not possible. Since all of the errors are cumulative in the reconstruction. So this follows that the accuracy of each point is dependent upon the accuracy of the previous point. If the Fourier series were to be truncated then the reconstruction cannot be guaranteed to be accurate. The reconstructed boundary will either not be fully connected or cross over itself. The distributional approach as like before, finds a histogram, in the case of radius distribution it is the slopes and cannot be used for reconstruction because the order in which the slopes were taken is not recorded [6]. Figure 2-4 illustrates the overall procedure.

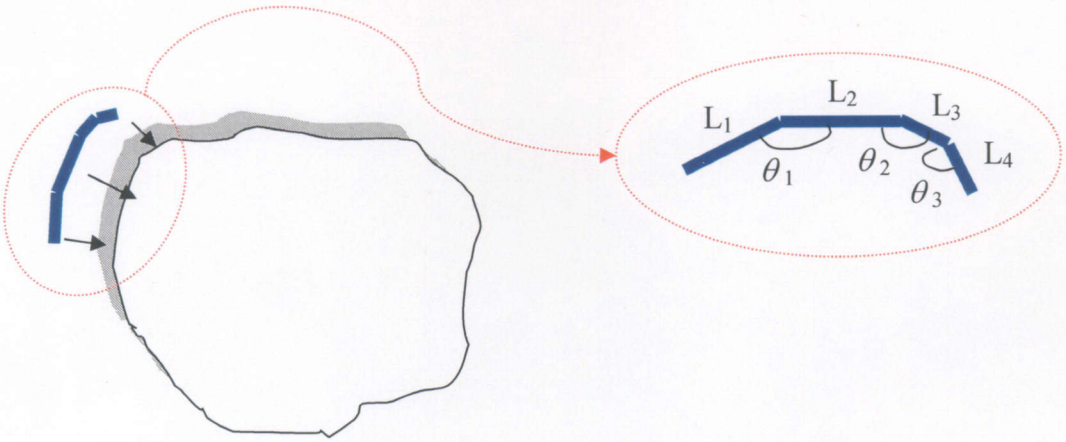

Figure 2-4: Example using angular bend.

2.2.1.3 Complex coordinates

For boundary characterization using the Fourier analysis technique, the final method to be discussed is complex coordinates. Complex coordinates also, like angular bend traverses the boundary beginning at a chosen starting point and collecting the x and y coordinate pairs which make up the boundary. To reduce this problem to 1-D the coordinate pairs can be reduced to a complex pair by setting the y axis to imaginary creating a new set of points in the form $x + jy$. This conversion will create a 1-D complex periodic function that will make it a candidate for Fourier analysis. This is a more advantageous to use over the previous techniques since the function decays faster in the Fourier domain allowing for greater data compression, without sacrificing accuracy in the final solution. Based on the qualities discussed earlier, this technique is the most promising of the three boundary methods previously discussed and consequently was used in [4]. Figure 2-5 shows an example of this method.

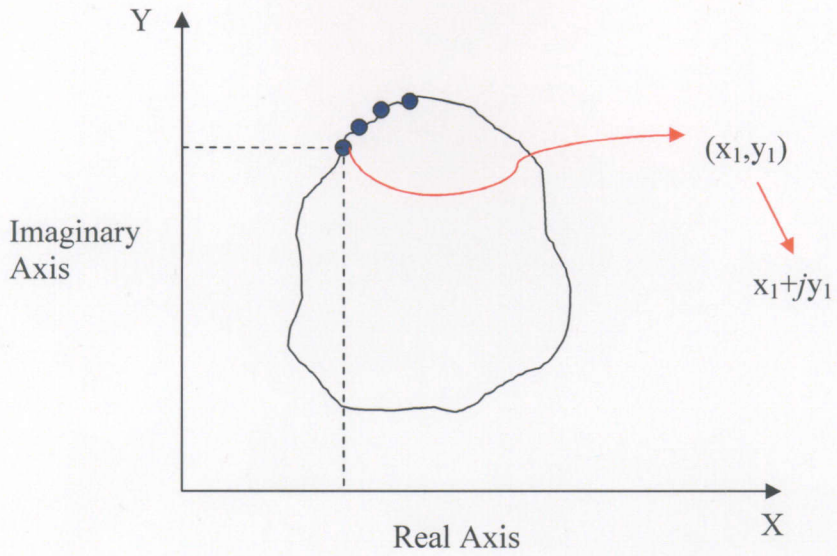

Figure 2-5: Example illustrating the complex coordinates boundary method.

2.2.1.4 Chord to perimeter

The chord to perimeter technique can only be used to compile a distribution and cannot be used in conjunction with a Fourier series analysis which is designed to compare the shape to that of a circle, which can be described and recreated quite easily. This technique is done by calculating the distance between two points along the boundary, as well as, the distance of the perimeter that it encases. This can be better described in Figure 2-6; where the red line is the calculated distance between the two points and the bottom hashed blue line represents the perimeter length.

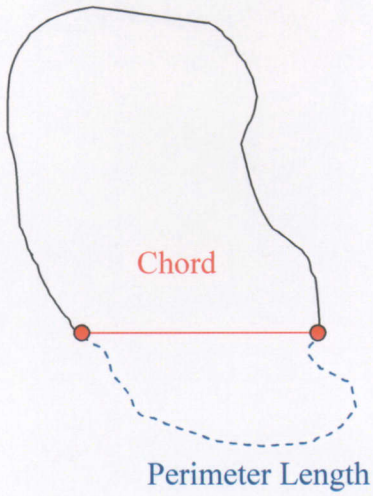

Figure 2-6: Example of the chord to perimeter technique.

From these measurements, a ratio can be calculated by taking the perimeter covered between the two points and dividing by the total perimeter. This determines the irregularity of the boundary. Small ratios are used to measure small irregularities and as the ratio reaches one they begin to measure large irregularities. When these values are compared with those obtained from a circle, an asphericity spectrum can be created. The asphericity spectrum is simply a way to measure how similar a shape is to a circle. One limitation to this is that the objects being examined must be fairly round for the method to work properly, or else unusable results will be obtained [3]. This method also cannot be used with Fourier analysis consequently making reconstruction from the descriptors impossible.

2.2.2 Planar surface

Planar surface techniques use the entire image in its analysis, making it un-necessary to locate the boundary. The major problem with this method is that the location of an object

in a picture could affect its calculations. In most shape description applications, this could be a detrimental flaw and must be corrected in order to design effective shape description algorithms.

2.2.2.1 Equivalent ellipses

The method of equivalent ellipses, shown in Figure 2-7, attempts to describe a complicated shape by using an ellipse, calculating the moments of inertia and the principle axes of the object. In using ellipses to characterize the object two factors must be met; the first is anisomery, which is the ratio of the long and short axis, the second factor is bulkiness. Bulkiness is the ratio of the area between the original object and that of the generated ellipse [3]. This method is advantageous since it is easily interpreted to physical characteristics of the shape.

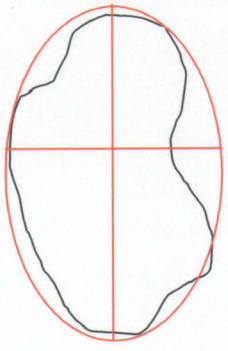

Figure 2-7: Equivalent ellipse technique.

2.2.2.2 2-D invariant moments

The final method discussed in this section uses a combination of 2-D moments. These 2-D invariant moments use mean, variance, and higher order moments to make statistically well-behaved descriptors [12, 13]. Since the assumption that similar shapes are expected to have similar moments, it can be concluded that they will be useful for characterization. As mentioned earlier, planar techniques, as such with 2-D invariant moments, are prone to errors due to scale and rotation changes. However, this problem was addressed by M. K. Hu where he proposed using a combination of moments to create a set of seven invariant moments, capable of characterizing any image [5].

The general equation for a two-dimensional moment of a continuous function, $f(x,y)$ is given as:

$$m_{pq} = \int_{-\infty}^{\infty} \int_{-\infty}^{\infty} x^p y^q f(x,y)\,dxdy \tag{2.1}$$

Where, p and q represent the order and x and y moments respectively. These moments can be centralized by subtracting out the means, and these central moments can be written as:

$$\mu_{pq} = \int_{-\infty}^{\infty} \int_{-\infty}^{\infty} (x-\bar{x})^p (y-\bar{y})^q f(x,y)\,dxdy \tag{2.2}$$

These continuous functions are not useful for discrete images, and can be discretized by summing the values over all the pixels instead of calculating the function integrals resulting in

$$\mu_{pq} = \sum_x \sum_y (x-\bar{x})^p (y-\bar{y})^q f(x,y) \tag{2.3}$$

where, p and q represent the order of the x and y moments respectively as seen in the continuous case Equation 2.1. The $f(x,y)$ refers to the image's gray level value of the pixel at each x and y. This equation obtains the contribution of each pixel to the central moment, which then sums all contributions to determine the final value of the moment. These moments can be normalized by dividing by the zeroth moments raised to the power of γ as defined below.

$$\eta_{pq} = \frac{\mu_{pq}}{\mu_{00}^{\gamma}} \tag{2.4}$$

where,

$$\gamma = \frac{p+q}{2} + 1 \tag{2.5}$$

The use of normalized moments ultimately lead to the creation of the Hu's invariant moments. The seven invariant moments are shown below. For the complete derivation of these equations please refer to the work done in [14].

$$\phi_1 = \eta_{20} + \eta_{02} \tag{2.6}$$

$$\phi_2 = (\eta_{20} + \eta_{02})^2 + 4\eta_{11}^2 \tag{2.7}$$

$$\phi_3 = (\eta_{30} - 3\eta_{12})^2 + (3\eta_{21} - \eta_{03})^2 \tag{2.8}$$

$$\phi_3 = (\eta_{30} - 3\eta_{12})^2 + (3\eta_{21} - \eta_{03})^2 \tag{2.9}$$

$$\begin{aligned}\phi_5 = {} & (\eta_{30} - 3\eta_{12})(\eta_{30} + \eta_{12})\left[(\eta_{30} + \eta_{12})^2 - 3(\eta_{21} + \eta_{03})^2\right] \\ & + (3\eta_{21} - \eta_{03})(\eta_{21} + \eta_{03})\left[3(\eta_{30} + \eta_{12})^2 - (\eta_{21} + \eta_{03})^2\right]\end{aligned} \tag{2.10}$$

$$\phi_6 = (\eta_{20} - \eta_{02})\left[(\eta_{30} + \eta_{12})^2 - (\eta_{21} + \eta_{03})^2\right] + 4\eta_{11}(\eta_{30} + \eta_{12})(\eta_{21} + \eta_{03}) \tag{2.11}$$

$$\phi_7 = (3\eta_{21} - \eta_{03})(\eta_{03} + \eta_{21})\left[(\eta_{30} + \eta_{12})^2 - 3(\eta_{21} + \eta_{03})^2\right] + (3\eta_{12} - \eta_{30})(\eta_{21} + \eta_{03})\left[3(\eta_{30} + \eta_{12})^2 - (\eta_{21} + \eta_{03})^2\right] \quad (2.12)$$

One of the most significant advantages of this method is its ease of implementation and its small number of descriptors. Having only a few descriptors will enhance the techniques ability to resistant to noise, in comparison with Fourier analysis, which usually needs at least ten and oftentimes more. Hu's 7 invariant moments are a fairly robust, easy-to-understand technique for describing shapes.

2.3 3-D shape description techniques

To describe 3-D shapes, most algorithms require the acquisition of the 3-D objects. In this section two previously used three-dimensional description methods are presented and it is assumed that the coordinates of the objects being analyzed have already been obtained using a 3-D imaging system. The most common method to capture such objects is the use of an X-ray computed tomography system. Though seemingly simple, to accomplish, factors such as cost and resolution of a system along with the time the reconstruction algorithm takes to build an object will vary depending on the utilized application. The two techniques being examined are spherical harmonics and three-dimensional invariant moments. Further discussions on the usefulness and efficiency of these algorithms presented will be noted at the end of this section.

2.3.1 Spherical harmonics

Spherical harmonics express a shape in a more useful mathematical form [7, 8]. The ability to characterize an object as a set of values can be extremely useful in models that oftentimes use only spheres or ellipsoids to represent 3-D shape. Assuming that a 3-D object has been obtained; this technique needs to locate the object using what is known as a "burning" algorithm. A burning algorithm is a process in which the object is separated from the background. The particle is then stored in a 3-D matrix, where each voxel, which by definition is a 3-D pixel, is represented by either a zero, for the background, or a one, for the object. The algorithm begins by searching the matrix until a one is discovered. This value of one will indicate the object has been discovered and then the algorithm will find all the adjacent voxels that are also labeled as ones. All matrix values that are found to contain the object are stored as x, y, and z coordinates. In this way the entire object can be captured as a sequence of coordinates.

Next, a center point which is common between all particle points must be located. The centroid may be used for this, and is calculated by summing the location values in each axis and then dividing by the total number of points. However, the center may not necessarily be the centroid and may be arbitrarily chosen, but it is important that the process remain consistent for all particles.

The characterization of the boundary shape can now be performed with the calculation of the center point. The distance from the center point to the aggregate surface is measured at specific angle intervals of ϕ (ranging from 0 to 2π) and θ (ranging from 0 to π). Once all distances for ϕ are measured, the value of θ is incremented and the process repeated. Once all values for θ have been used, a function $r(\theta,\phi)$ is created

from the data, which may be used for further analysis. The equation for spherical components is:

$$r(\theta,\phi)=\sum_{n=0}^{\infty}\sum_{m=-n}^{n}a(n,m)Y_n^m(\theta,\phi) \tag{2.13}$$

Where, $Y_n^m(\theta,\phi)$ is a spherical harmonic function of order (n,m) and $a(n,m)$ is a numerical coefficient. Orders for n are typically taken upwards of 30 for efficient characterization [6, 7].

2.3.2 3-D invariant moments

3-D invariant moments are nothing more than an extension of the 2-D invariant moments which were discussed earlier in this chapter. The equation for a 3-D moment is given by:

$$m_{pqr}=\int_{-\infty}^{+\infty}\int_{-\infty}^{+\infty}\int_{-\infty}^{+\infty}x_1^p x_2^q x_3^r \rho(x_1,x_2,x_3)\,dx_1dx_2dx_3 \tag{2.14}$$

Where, p, q, and r signify the order of the moment and $\rho(x_1, x_2, x_3)$ represents the density of the object. The density function is assumed to be piecewise and continuous, making it bounded [14, 15]. Equation 2.14 can be converted to a central moment, by subtracting out the centroid of the coordinates shown in the following two equations stated below.

$$\mu_{pqr}=\int_{-\infty}^{+\infty}\int_{-\infty}^{+\infty}\int_{-\infty}^{+\infty}(x_1-\bar{x}_1)^p(x_2-\bar{x}_2)^q(x_3-\bar{x}_3)^r \rho(x_1,x_2,x_3)\,dx_1dx_2dx_3 \tag{2.15}$$

Where,

$$\bar{x}_1=\frac{m_{100}}{m_{000}},\bar{x}_2=\frac{m_{010}}{m_{000}},\bar{x}_3=\frac{m_{001}}{m_{000}} \tag{2.16}$$

Finally the equation can now be normalized by

$$\eta_{pqr} = \frac{\mu_{pqr}}{(\mu_{000})^{\frac{p+q+r+3}{3}}} \tag{2.17}$$

Equation 2.17 can be used to generate 3-D moments; however, this comes at a high price, the computational complexity is very high even for lower order moments. As higher and higher order moments need to be calculated, their implementation becomes computationally prohibitive [14, 15].

The three-dimensional shape description techniques discussed all require that the 3-D data of the particle be captured, which is usually accomplished with an X-ray tomography system. Not only does each method rely on expensive equipment to do their analysis, but they also need significant processing power, in order to achieve results in a reasonable amount of time. Even if such technology is available, the specific nature of analyzing each individual grain of sand may not be completely necessary. The generalization acquired by using 2-D descriptors could actually yield more effective results, by using an estimation based on statistics.

2.4 Principal component analysis

The objective principal component analysis (PCA) is to take advantage of the similarities and differences contained within the data. In a multi-dimensional dataset, PCA isolates the most important components within the data which allows for dimensionality reduction with a small loss of discriminatory information. More importantly for the shape characterization application, it allows *n*-dimensional data to be visualized in 3-D which is known as PC-space.

PCA assumes that the most discerning information about a dataset lies along the axis with the greatest variance. Thus, the first principal component is the axis with the greatest variance, and each subsequent component would be the axis with the next greatest variance [16]. These components axes are found by calculating the mean vector, the mean of all instances about each descriptor, and covariance matrix of the data. Eigenvalues and eigenvectors of the covariance matrix are calculated and sorted in decreasing order by eigenvalue. The principal components consist of the projection of the data along the corresponding eigenvectors, with the eigenvectors having the greatest eigenvalues containing the most discerning information and those with the smallest eigenvalues merely contributing to the "noise" in the data, otherwise containing little or no relevant overall information. By projecting the data onto only the major principal components, the data's dimensionality can be reduced and separability between instances can be theoretically increased. Figure 2-8 shows PCA on a 2-D dataset. The two axes represent the data according to the data with the best variance chosen and are shown in red. In [4], PCA was applied to Fourier descriptor data to reduce the dimensionality from 15 dimensions to 3 dimensions and will be discussed more in the next section.

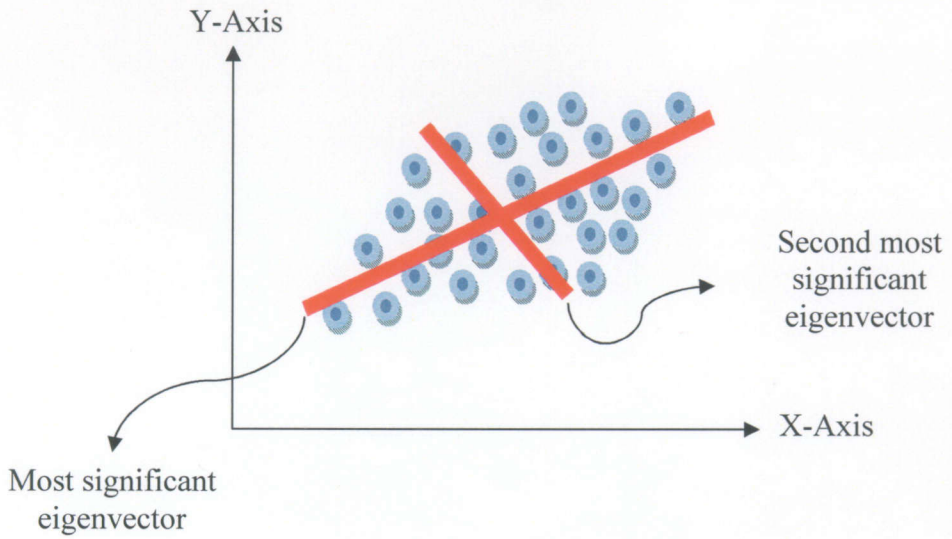

Figure 2-8: 2-D PCA example.

2.5 3-D shape characterization for particle aggregates using multiple projective representations

The primary technique described in [4] focused on finding a 2-D approach for acquiring 3-D shape descriptors, where the complex coordinate Fourier analysis and invariant moments were instituted. The benefit of this technique is that it does not rely on an expensive X-ray tomography unit, rather, a relatively inexpensive setup consisting of an optical microscope and digital camera. This section will focus solely on the complex Fourier analysis technique since reconstruction of projections is not possible with invariant moments.

This method of 3-D shape description combines the techniques of boundary unrolling, complex Fourier analysis and PCA to capitulate a method possessing the four most desired attributes of a shape characterization algorithm: uniqueness, parsimony, independence, and invariance. Also as a secondary attribute, it possesses the following: reconstruction and automatic collection. There are two major parts to this algorithm: statistical mix characterization and particle synthesis.

In the statistical mix characterization step, single projections of multiple particles are captured using a standard digital camera and microscope. This is done such that the sand is scattered on a surface and an image is captured of all the particles. Next, each image is processed so that only the boundary of each particle remains. The boundary for each particle is "unrolled" and converted into a complex periodic function, as discussed earlier in this chapter. The 1-D function for each particle is re-sampled and normalized to ensure that the same number of points (and corresponding frequencies) exist between all particles and that the magnitudes of the FFT's lie within the same range, providing invariance in the algorithm. After the desired Fourier coefficients are chosen, PCA is performed on the transformed data to yield the final number of descriptors which is constant for all of the particles. For each particle, the result would be n descriptors [D_1 D_2 ...D_n]. Due to the normalization and re-sampling step, the first descriptor of a particle would represent the same frequencies as the first descriptor of every other particle, with the only difference being variations in magnitude. The same holds true for the remaining second through n^{th} descriptors. This allows *distributions* of descriptors to be formed, allowing for the characterization of an entire mix of sand particles by simply using n

means and variances (the Central Limit Theorem allows for the assumption that these distributions are Gaussian).

Particle synthesis occurs in three steps: descriptor generation, projection formation, and projection combination. Descriptor generation is accomplished by generating a random number, multiplying by the variance of the desired descriptor, and adding the mean of the desired descriptor. A value for that descriptor is created that lies within the distribution found for that particular mix. The process is repeated n times (once for each of the n descriptors) to produce a descriptor set. The newly formed descriptor set is the input for the projection generation step, which is the reversal of the PCA, Fourier transform and "unrolling" steps mentioned earlier. Ultimately creating the boundary image of a projection, which may then be filled in or left as is depending on the requirements of the algorithm used for the projection combination step. In the final step of the process, informal algorithms were developed in [4], such as extrusion, rotation and a "tomographic" reconstruction algorithm for the purpose of projection combination. However, in this thesis the Algebraic Reconstruction Technique (a popular, formal tomographic reconstruction algorithm) has been used for the projection combination step used in particle synthesis and is discussed in the next section. Figure 2-9 shows the overall approach for this method.

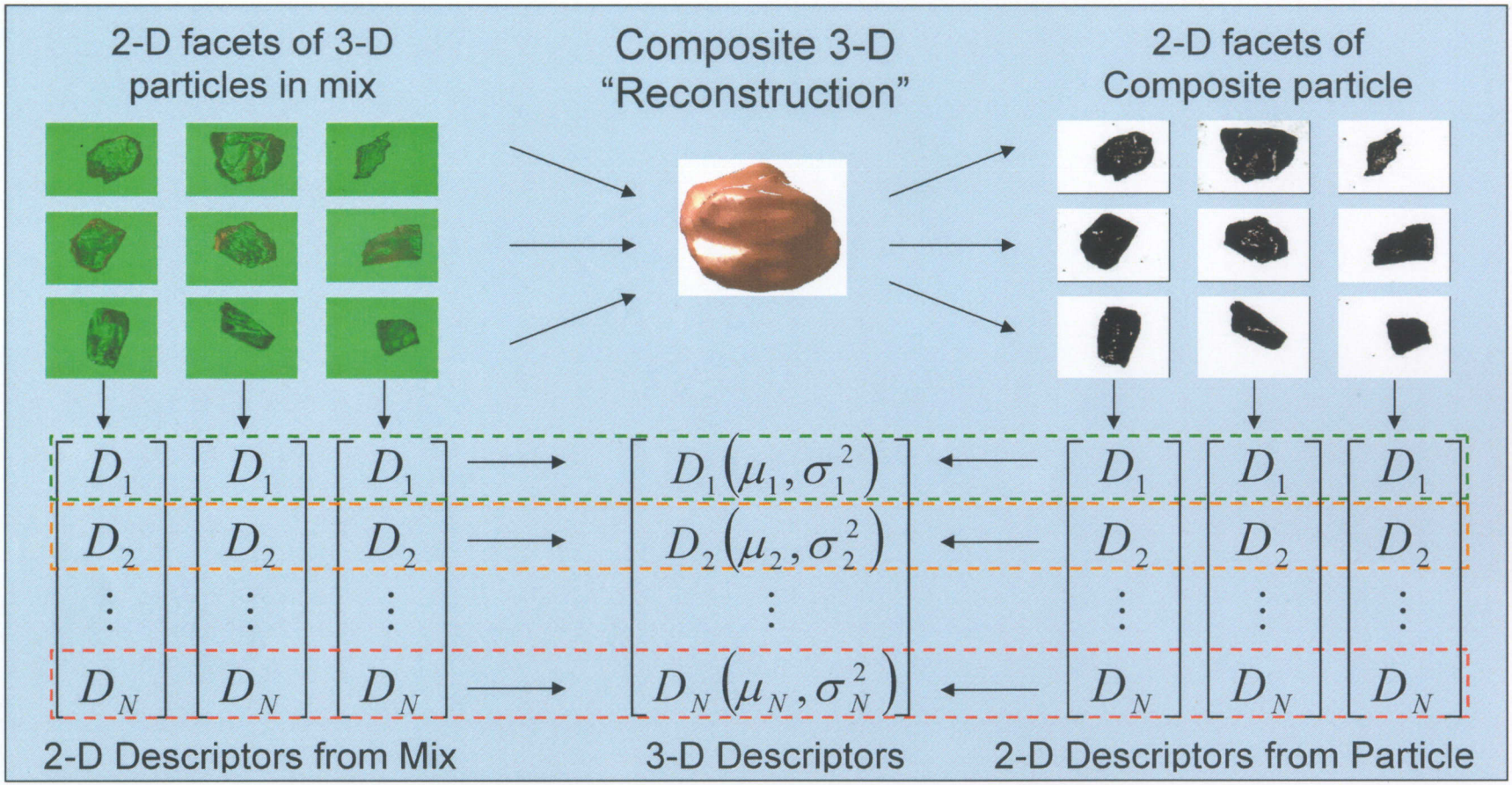

Figure 2-9: Overall approach for the 3-D shape characterization for particle aggregates using multiple projective representations method. *Upper-left*: optical images are taken of a mix of particles. *Bottom left*: Boundaries of each optical image are characterized using Fourier analysis to yield 2-D descriptors for each image. *Top center*: A 3-D composite particle with shape characteristics representative of the entire mix can be formed by combining several optical images. *Top right*: 2-D projections of the 3-D composite particle are taken. *Bottom right*: 2-D projections are characterized like the optical images. Bottom center: 2-D descriptors of the optical images and/or projections are combined to form 3-D descriptors in the form of statistical distributions. Both sets of images are expected to yield the same 3-D descriptors.

2.6 *Tomographic reconstruction methods*

Tomography can be described as the process of collecting the refraction or transmission data by illuminating an object from several different directions. There are several methods of performing reconstruction on the cross sectional images acquired through tomography, which can be performed in two ways; iterative or non-iterative. One of the most widely used methods is the non-iterative method, used in the Feldkamp algorithm for performing filtered backprojection (FBP). For the iterative methods, the algebraic reconstruction technique (ART) is used.

2.6.1 Filtered back projection (FBP)

In this section, the filtered backprojection (FBP) method of reconstruction will be discussed. It will begin with the definition of a projection, followed by the derivation of the Fourier Slice Theorem and concluded with the derivation of the FBP method for parallel projections.

2.6.1.1 Definition of a projection

A 2-D object may be described as a function $f(x,y)$ and a series of line integrals characterized by the parameters (θ,t). Figure 2-10 shows an object and the corresponding line integrals.

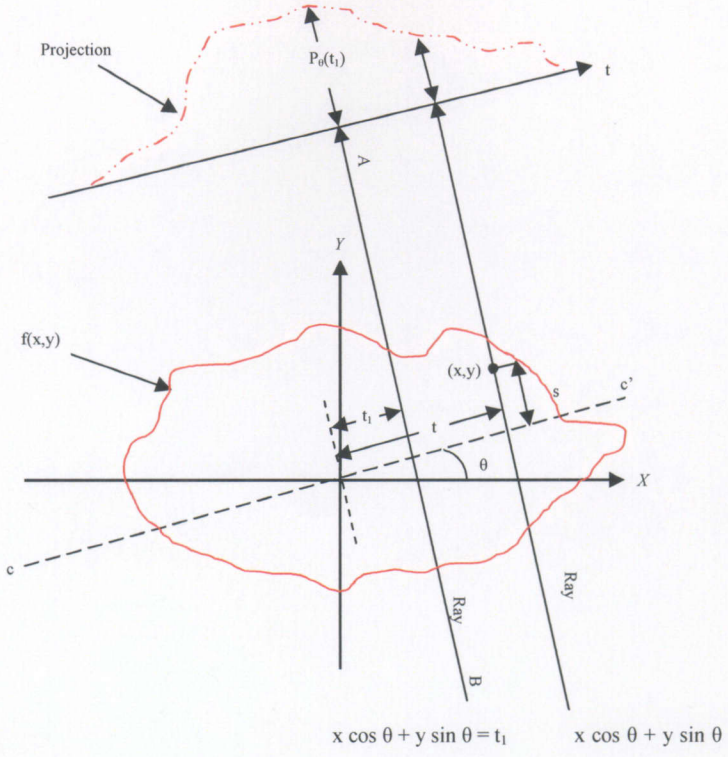

Figure 2-10: An object *f(x,y)* and its projection, $P_\theta(t)$[4].

The equation of the line AB shown in above Figure 2-10 is given by Equation 2.18

$$x\cos\theta + y\sin\theta = t \tag{2.18}$$

thusly this equation can be used to describe the line integral $P_\theta(t)$ as follows

$$P_\theta(t) = \int_{(\theta,t)line} f(x,y)ds \tag{2.19}$$

Equation 2.19 can then be re-written with the delta function,δ seen as

$$P_\theta(t) = \int_{-\infty}^{\infty}\int_{-\infty}^{\infty} f(x,y)\delta(x\cos\theta + y\sin\theta - t)dxdy \tag{2.20}$$

The function $P_\theta(t)$ is known as the Radon transform of the function *f(x,y)*. A projection is then formed by combining a set of line integrals. The most common types of projections are parallel and fan beam projections. Fan beam projections are easily

sorted into parallel beam, with current algorithms that are commonly found in high end scanning and reconstruction systems, and for that will not be discussed in the remainer of this section. Examples of parallel beam projections are shown in Figure 2-11.

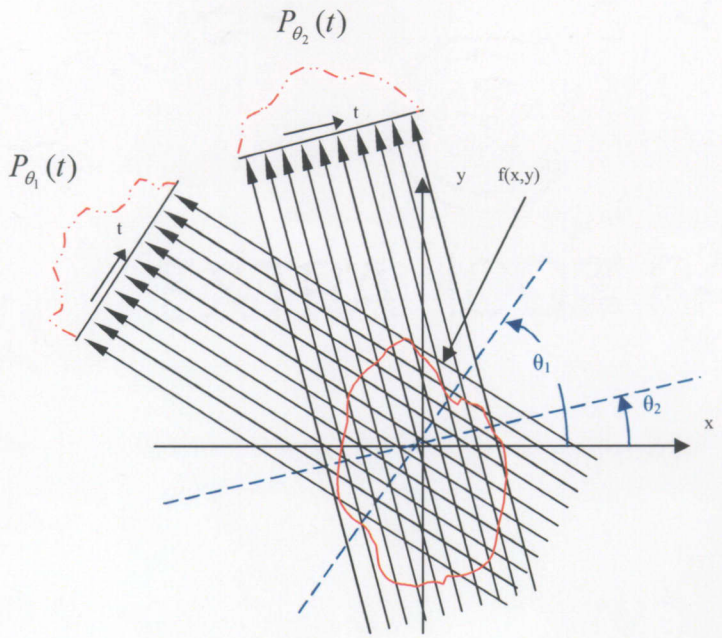

Figure 2-11: A pair of parallel projections taken at different angles.

2.6.1.2 Fourier slice theorem

The Fourier slice theorem is derived by taking the 1-D Fourier transform of a parallel projection and understanding that it is the same as a slice of the 2-D Fourier transform of the original object, thusly the Fourier slice theorem. This implies that given the projection data for an object, it should be possible to estimate the original object by inverting a 2-D Fourier transform.

The 2-D Fourier transform of the object can be described by Equation 2.21

$$F(u,v) = \int_{-\infty}^{\infty}\int_{-\infty}^{\infty} f(x,y)e^{-j2\pi(ux+vy)}dxdy \tag{2.21}$$

The Fourier transform of a projection, $P_\theta(t)$ is defined as:

$$S_\theta(\omega) = \int_{-\infty}^{\infty} P_\theta(t)e^{-j2\pi\omega t}dt \tag{2.22}$$

Consider the simplest example of the Fourier slice theorem which is where $\theta = 0$. Then, consider the Fourier transform along the line of the object in the ω domain given by $v = 0$, taking Equation 2.21 and reducing to the following:

$$F(u,0) = \int_{-\infty}^{\infty}\int_{-\infty}^{\infty} f(x,y)e^{-j2\pi ux}dxdy \tag{2.23}$$

Since the phase factor is no longer dependent on y, Equation 2.23 can be divided into two parts:

$$F(u,0) = \int_{-\infty}^{\infty}\left[\int_{-\infty}^{\infty} f(x,y)dy\right]e^{-2\pi ux}dx \tag{2.24}$$

The term of Equation 2.24 in brackets is the equation for a projection along lines of constant x (from the definition of a parallel projection):

$$P_{\theta=0}(x) = \int_{-\infty}^{\infty} f(x,y)dy \tag{2.25}$$

Substituting into Equation 2.25 into Equation 2.24 yields:

$$F(u,0) = \int_{-\infty}^{\infty} P_{\theta=0}(x)e^{-j2\pi ux}dx \tag{2.26}$$

On the right hand side of Equation 2.26 is the 1-D Fourier transform of the projection $P_{\theta=0}$; this gives the following relationship between the vertical projection and the 2-D transform of the object function:

$$F(u,0) = S_{\theta=0}(u) \tag{2.27}$$

This result is obtained regardless of the orientation between the object and coordinate system, leads to the Fourier Slice Theorem. The theorem states that the Fourier transform of a parallel projection of a 2-D object *f(x,y)* taken at an angle θ is the same as the Fourier transform of 2D the same object *F(u,v)* along a line at angle θ with respect to the *u* axis [17]. Figure 2-12 illustrates this concept.

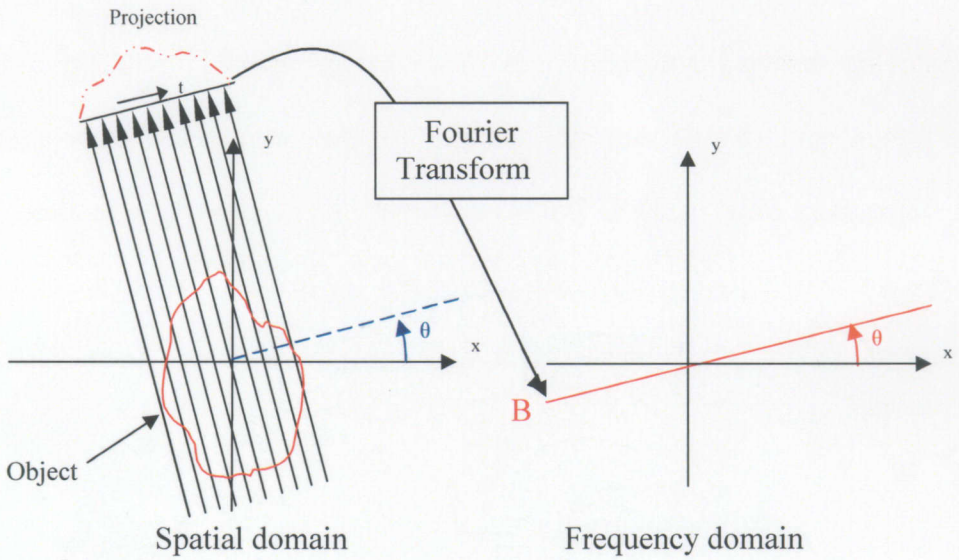

Figure 2-12: Fourier transform of a 1-D projection as related to a slice of the Fourier transform of a 2-D object by the Fourier slice theorem.

The derivation of the Fourier slice theorem can now be generalized by considering the coordinate system (*t,s*) to be a rotated version of the original (*x,y*) system as given by:

$$\begin{bmatrix} t \\ s \end{bmatrix} = \begin{bmatrix} \cos\theta \sin\theta \\ -\sin\theta \cos\theta \end{bmatrix} \begin{bmatrix} x \\ y \end{bmatrix} \tag{2.28}$$

In the (t,s) system a projection along lines of constant t is

$$P_\theta(t) = \int_{-\infty}^{\infty} f(t,s)ds \tag{2.29}$$

Substituting the definition of a projection given by Equation 2.29 into its Fourier transform given by Equation 2.22 yields

$$S_{\theta(\omega)} = \int_{-\infty}^{\infty} \left[\int_{-\infty}^{\infty} f(t,s)ds \right] e^{-j2\pi\omega t} dt \tag{2.30}$$

The RHS of (2.30) is the 2D Fourier transform at a spatial frequency of $(u = \omega\cos\theta, v = \omega\sin\theta)$or

$$S_\theta(\omega) = F(\omega,\theta) = F(\omega\cos\theta, \omega\sin\theta) \tag{2.31}$$

Equation 2.35 proves the Fourier slice theorem as well as is the core of straight ray tomography. So, if projections on an object are captured at angles, $\theta_1, \theta_2 \ldots \theta_k$, the function F$(u,v)$ on the radial lines can be determined by calculating their respective Fourier transforms. If an infinite number of projections are taken, the values for $F(u,v)$ would be known in the entire uv-plane. If $F(u,v)$ is known, the object function $f(x,y)$ can be recovered using the inverse Fourier transform seen in Equation 2.32:

$$f(x,y) = \int_{-\infty}^{\infty} \int_{-\infty}^{\infty} F(u,v)e^{j2\pi(ux+vy)} dudv \tag{2.32}$$

Take the function $f(x,y)$, and assume that it is bounded by $-\frac{A}{2} < x < \frac{A}{2}, -\frac{A}{2} < y < \frac{A}{2}$, now Equation 2.32 can be rewritten as follows:

$$f(x,y)=\frac{1}{A^2}\sum_m\sum_n F\left(\frac{m}{A},\frac{n}{A}\right)e^{j2\pi((m/A)x+(n/A)y)} \tag{2.33}$$

$$where\ -\frac{A}{2}<x<\frac{A}{2},-\frac{A}{2}<y<\frac{A}{2}$$

however, when preformed in practice only a finite number of Fourier coefficients will be known, so (2.33) can be written as

$$f(x,y)=\frac{1}{A^2}\sum_{m=-N/2}^{N/2}\sum_{n=-N/2}^{N/2} F\left(\frac{m}{A},\frac{n}{A}\right)e^{j2\pi((m/A)x+(n/A)y)} \tag{2.34}$$

$$where\ -\frac{A}{2}<x<\frac{A}{2},-\frac{A}{2}<y<\frac{A}{2}$$

N is arbitrarily assumed to be an even integer, which will define the spatial resolution in the reconstructed image. If the N^2 Fourier coefficients $F(\frac{m}{A},\frac{n}{A})$ are known, Equation 2.34 can be implemented using the FFT algorithm. Since the number of projections taken is finite, the function $F(u,v)$ is only known along a finite number of radial lines, like in Figure 2-13. In order to use the equation seen in 2.35, interpolation between the radial points must be performed. The error resulting from this interpolation translates into image degradation, as the higher frequency components have a greater interpolation error than the low frequency ones. This is due to the distance between the radial points increasing as the distance from the center increases.

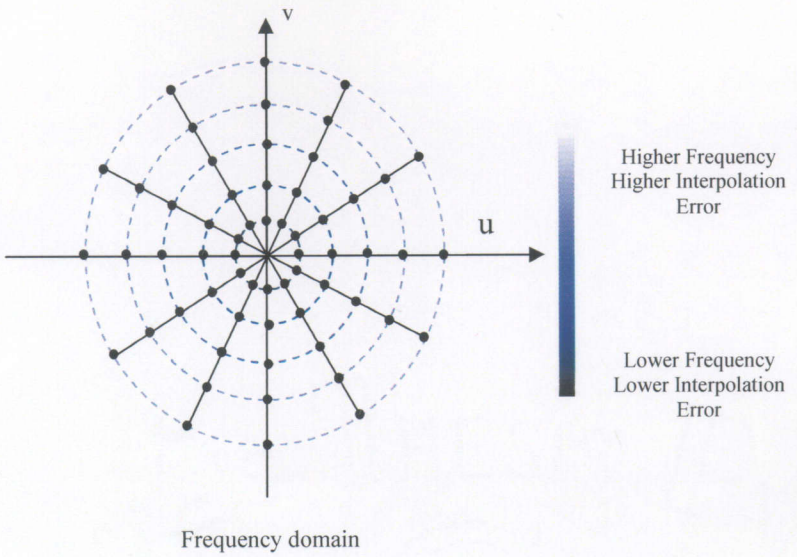

Figure 2-13: Estimation of the Fourier transform of a 2-D object. Each radial line is the FFT of a projection where the dots represent the actual location of the object's Fourier transform.

2.6.1.3 The rationale behind the FBP algorithm

The justification behind the filtered backprojection algorithm is rather intuitive and straightforward because each projection can be considered as a nearly independent measurement of the object. This can be better illustrated after taking the Fourier transform of each projection at its associated angle. The reason the projections are said to be nearly independent is ultimately seen in the result where the only information that is common between two projections at different angles is the 0^{th} frequency or DC term.

The act of measuring a projection can be considered a 2-D filtering operation, due to the Fourier Slice Theorem. For instance, take a single projection and its Fourier transform. By the Fourier Slice Theorem, this projection gives the object's two-dimensional Fourier transform along a single line. If the values resulting from the Fourier transform of this projection are inserted into their proper places and all other

projections are set to zero, a very simple (yet very distorted) reconstruction can be obtained by simply performing the inverse Fourier transform. The previous example was merely to demonstrate that the reconstruction formed is equivalent to the original object's Fourier transform multiplied by the filter shown in Figure 2-14b.

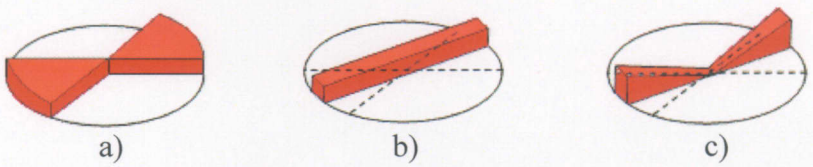

Figure 2-14: Frequency domain data available from one projection. a) Shows the ideal situation where a reconstruction could be formed by adding the reconstruction from each angle until the entire Fourier domain is filled. b) Shows what is actually measured. The filtered backprojection algorithm takes the data shown in b) and weights it so that the data in c) are an approximation to those in a).

A simple reconstruction procedure is simply the sum of object projections filtered by pie-shaped wedges as illustrated in Figure 2-14a. Due to the property of linearity inherent in the Fourier transform, this summation may be performed in either the spatial or frequency domain. When processed in the spatial domain, the result is backprojection.

The name of this algorithm implies two steps: the filtering step, which can be thought of as a simple weighting of each projection in frequency, and the backprojection step, which is finding the elemental reconstructions corresponding to each wedge filter mentioned earlier. The filtering step is done to take the value of the Fourier transform of the projection, $S_\theta(\omega)$, and multiply it by the width of the wedge at its corresponding frequency. Therefore, if there were K projections over 180° at a given frequency ω, each wedge would have a width of $\frac{2\pi|\omega|}{K}$. The effects of this weighting are demonstrated in Figure 2-14c. Comparing this to Figure 2-14a, it can be seen that the weighted projection

$\frac{2\pi|\omega|}{K} S_\theta(\omega)$ has the same "mass" as the pie-shaped wedge. Accordingly, the weighted projections are indeed approximations to the pie-shaped wedge, but the error can be made arbitrarily small by using a sufficient number of projections.

The final reconstruction is then achieved by summing the spatial domain representations of the weighted projections. Accordingly each projection only gives the Fourier transform of the object along a single line, this inversion can be performed very quickly, which is better known as backprojection, since it can be perceived as the smearing of each filtered projection over the image plane. The entire FBP algorithm can be written as the following:

For each of the K angles, θ, between 0 and 180°

Measure the projection, $P_\theta(t)$

Fourier transform $P_\theta(t)$ to find $S_\theta(\omega)$

Multiply $S_\theta(\omega)$ by the weighting function $\frac{2\pi|\omega|}{K}$

Sum over the image plane the inverse Fourier transforms of the filtered projections (the backprojection process) [17]

2.6.1.4 The theory of the FBP algorithm

This section will address the theory behind the backprojection algorithm for parallel beam projections. The object function, $f(x,y)$ can be expressed in terms of its Fourier transform as

$$f(x,y) = \int_{-\infty}^{\infty}\int_{-\infty}^{\infty} F(u,v)e^{j2\pi(ux+vy)}dudv \tag{2.35}$$

The Cartesian coordinate system in the frequency domain, *(u,v)* may be exchanged for a polar coordinate system, *(ω,θ)* by substituting the following

$$u = \omega\cos\theta \tag{2.36}$$

$$v = \omega\sin\theta \tag{2.37}$$

and then changing the differential terms to

$$du\,dv = \omega\,d\omega\,d\theta \tag{2.38}$$

the inverse Fourier transform of Equation 2.37 may then be rewritten as

$$f(x,y) = \int_{0}^{2\pi}\int_{0}^{\infty} F(\omega,\theta)e^{j2\pi\omega(x\cos\theta+y\sin\theta)}\omega\,d\omega\,d\theta \tag{2.39}$$

Equation 2.39 may be split into two integrals considering θ from 0° to 180° and 180° to 360°

$$\begin{aligned} f(x,y) = &\int_{0}^{\pi}\int_{0}^{\infty} F(\omega,\theta)e^{j2\pi\omega(x\cos\theta+y\sin\theta)}\omega\,d\omega\,d\theta + \\ &\int_{0}^{\pi}\int_{0}^{\infty} F(\omega,\theta+180°)e^{j2\pi\omega(x\cos(\theta+180°)+y\sin(\theta+180°))}\omega\,d\omega\,d\theta \end{aligned} \tag{2.40}$$

and then using the property

$$F(\omega,\theta+180°) = F(-\omega,\theta) \tag{2.41}$$

Using this property Equation 2.40 can be written as follows

$$f(x,y) = \int_{0}^{\pi}\left[\int_{-\infty}^{\infty} F(\omega,\theta)|\omega|e^{j2\pi\omega t}d\omega\right]d\theta \tag{2.42}$$

where,

$$t = x\cos\theta + y\sin\theta \tag{2.43}$$

By Substituting the Fourier transform of the projection at angle θ, $S_\theta(\omega)$, for the two-dimensional Fourier transform $F(\omega,\theta)$, results in

$$f(x,y)=\int_0^{\pi}\left[\int_{-\infty}^{\infty} S_\theta(\omega)|\omega|e^{j2\pi\omega t}d\omega\right]d\theta \tag{2.44}$$

This can be again rewritten as seen in Equation 2.45 as

$$f(x,y)=\int_0^{\pi} Q_\theta(x\cos\theta+y\sin\theta)d\theta \tag{2.45}$$

where,

$$Q_\theta(t)=\int_{-\infty}^{\infty} S_\theta(\omega)|\omega|e^{j2\pi\omega t}d\omega \tag{2.46}$$

Equation 2.45 is an estimate of $f(x,y)$, given the projection data transform $S_\theta(\omega)$, and Equation 2.46 represents a filtering operation on the projection data, where the frequency response is given by $|\omega|$. Thus, $Q_\theta(\omega)$ is a "filtered projection". These filtered projections are then summed for different angles of θ to form the estimate of the original $f(x,y)$.

In Equation 2.47 each filtered projection, Q_θ is "backprojected", meaning for every point (x,y) in the image plane, there is a corresponding value of $t=x\cos\theta+y\sin\theta$ for a given value of θ. Q_θ contributes to the reconstruction of its value at t. The previous process can be better illustrated in Figure 2-15. For an angle θ, it can be easily be revealed that the value of t is the same for all *(x,y)* along the line LM. The significance of this is that the filtered projection, Q_θ, will make the same contribution

to the reconstruction at each of the pixels lying on this line. In other words, the filtered projection Q_θ can be considered to be backprojected over the image plane, or more simply put smeared back.

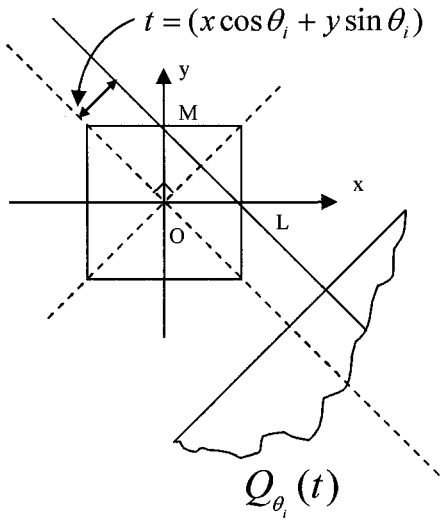

Figure 2-15: Filtered projection being backprojected onto the reconstruction plane along the lines of the constant, t. the filtered projection at a point t, makes the same contribution to all pixels that lie on the line LM in the x-y plane.

In theory, the integration must be carried out over all spatial frequencies, but in practice the amount of energy present in the high frequency components of the Fourier transform is negligible. For all practical purposes the Fourier transform of a projection can be considered to be bandlimited. Let Ω be a frequency higher than the highest frequency component in each projection, then by the sampling theorem the projections can be sampled at intervals of

$$T = \frac{1}{2\Omega} \tag{2.47}$$

without the introduction of significant error.

Assume that at large values of |t| the projection data is equivalent to zero. A projection can then be represented as

$$P_\theta(mT), \qquad m = \frac{-N}{2},\ldots,0,\ldots,\frac{N}{2}-1 \tag{2.48}$$

For a large value of N, the Fourier transform $S_\theta(\omega)$ of a projection can be approximated using the Fast Fourier Transform, FFT, algorithm by

$$S_\theta(\omega) \approx S\left(m\frac{2\Omega}{N}\right) = \frac{1}{2\Omega}\sum_{k=-N/2}^{N/2-1} P_\theta\left(\frac{k}{2\Omega}\right)e^{-j2\pi(mk/N)} \tag{2.49}$$

Equation 2.49 yields the samples of the Fourier transform of a projection, given its occurring samples in space. Subsequently, the "modified projection", Q_θ must be evaluated digitally. Since the Fourier transforms S_θ have been assumed to be bandlimited, Equation 2.47 can be approximated by

$$Q_\theta(t) = \int_{-\Omega}^{\Omega} S_\theta(\omega)|\omega| e^{j2\pi\omega t} d\omega \tag{2.50}$$

$$\approx \frac{2\Omega}{N}\sum_{m=-N/2}^{N/2} S_\theta\left(m\frac{2\Omega}{N}\right)\left|m\frac{2\Omega}{N}e^{j2\pi m(2\Omega/N)t}\right| \tag{2.51}$$

given that N is of a large quantity. To determine the projections Q_θ for only those t which the projections P_θ are sampled

$$Q_\theta\left(\frac{k}{2\Omega}\right) \approx \left(\frac{2\Omega}{N}\right)\sum_{-N/2}^{N/2} S_\theta\left(m\frac{2\Omega}{N}\right)\left|m\frac{2\Omega}{N}\right| e^{j2\pi(mk/N)} \tag{2.52}$$

$$k = -N/2,\ldots,-1,0,1,\ldots N/2 \tag{2.53}$$

This filtered projection may be multiplied with another function (such as a Hamming window) to reduce the effects of observation noise. The reconstructed object may be obtained from a discrete approximation to Equation 2.45 by

$$f(x,y) = \frac{\pi}{K}\sum_{i=1}^{K} Q_{\theta i}(x\cos\theta_i + y\sin\theta_i) \tag{2.54}$$

where the K angles θ_i are those for which the projections $P_\theta(t)$ are known.

2.6.2 Algebraic reconstruction algorithms

Tomographic reconstruction can also be approached by assuming that the cross sections are an array of unknowns, which can be solved by using a system of linear equations. In comparison to the previous technique, (FBP), this method lacks the ability for speed and accuracy. However, when a large number of projections are unavailable or not evenly distributed this method can still provide a solution. The algebraic reconstruction technique otherwise known as ART will be discussed in detail, as well as the simultaneous iterative reconstruction technique SIRT and simultaneous algebraic reconstruction technique SART.

2.6.2.1 Image and projection representation

By observing Figure 2-16, an image function which can be represented by $f(x,y)$, is superimposed with a square grid. Set the value for $f(x,y)$ to be constant within a given cell, and contain a value of f_j (this is the constant value in the j^{th} cell). Next, let N be the total number of cells. In algebraic techniques, a ray is defined as a line with a measurable

width, τ. The i^{th} ray in Figure 2-16 is highlighted to illustrate this concept. For most cases τ will be the same as a cell width. The line integral from the FBP method is now replaced as a *ray-sum* in the ART technique.

Projections will be given a single index representation, like the image. Let p_i be the ray-sum measured with the i^{th} ray as shown in Figure 2-16. The relationship between the f_j's and the p_i's can be expressed in the following form

$$\sum w_{ij} f_j = p_i, \qquad i = 1, 2, \ldots, M \tag{2.55}$$

where, M is the total number of rays (in *all* the projections) and w_{ij} is the weighting factor which represents the contribution of the j^{th} cell to the i^{th} ray integral. More simply put, w_{ij} is the part of the j^{th} cell that is within the area of the i^{th} ray, as shown for one of the cells in Figure 2-16. Notice that the majority of the w_{ij}'s are equal to zero since only a few cells contribute to any given ray-sum.

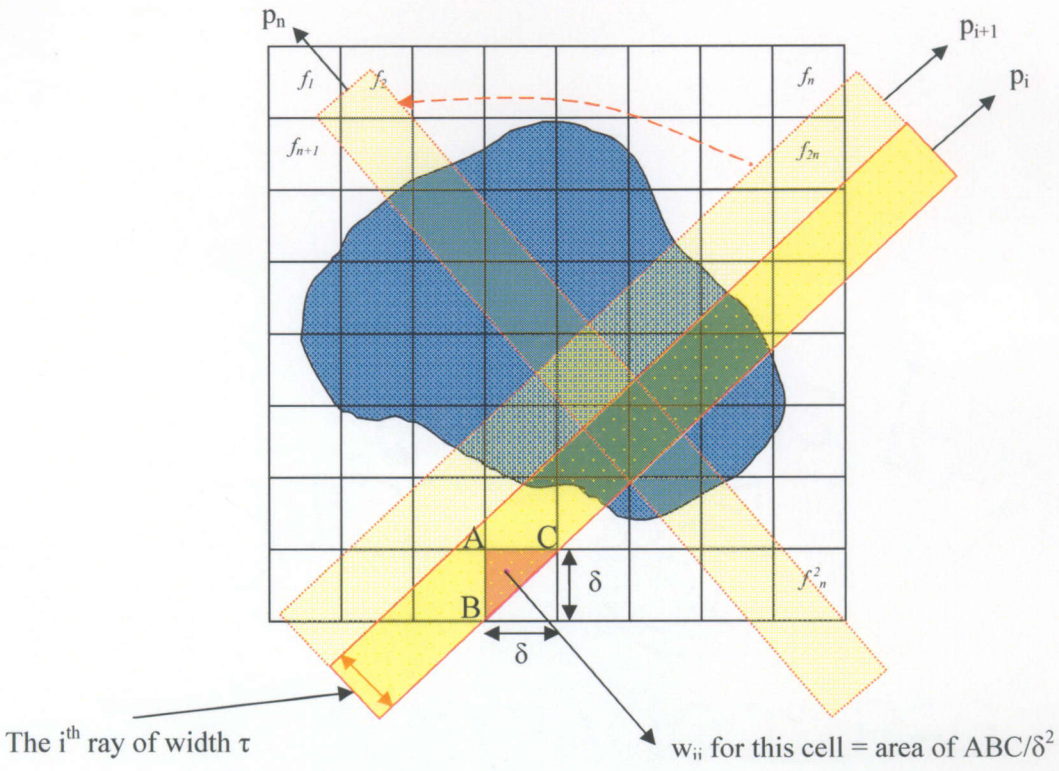

Figure 2-16: Image shown with a grid superimposed onto it, where image values are assumed to be constant within a cell.

One of the problems that we face as mentioned in previous chapters is computational complexity. If the values represented by M and N are small, standard matrix inversion methods could be used to solve the system of linear equations, though in practice the values for M and N can be as large as if not exceeding 65,536 for a 256x256 image. The size of the weight matrix would then be 65,536x65,536, making direct matrix inversion practically impossible, but more importantly infeasible. This impracticality is also the case when there is noise present in the measurement data, and when $M < N$ (even for small N) and a least squares method must be used. Unfortunately, in the case where M and N are large, even these methods may be computationally impractical. By today's

standards a 256x256 image is nearly obsolete, with the emphasis on higher resolution images.

To solve the problem of large M and N values, there exists and iterative method for solving Equation 2.55, that is based on the "method of projections" which was first proposed by Kaczmarz [18] and the clarified by Tanabe [19]. To explain these methods Equation 2.55 has be expanded

$$\begin{aligned} w_{11}f_1 + w_{12}f_2 + w_{13}f_3 + \ldots + w_{1N}f_N &= p_1 \\ w_{21}f_1 + w_{22}f_2 + w_{23}f_3 + \ldots + w_{2N}f_N &= p_2 \\ &\vdots \\ w_{M1}f_1 + w_{M2}f_2 + w_{M3}f_3 + \ldots + w_{MN}f_N &= p_M \end{aligned} \tag{2.56}$$

A grid representation with a total of N cells gives image N degrees of freedom. As a result, an image, represented by (f_1, f_2, ... , f_N), may be considered to be a single point in an N- dimensional space. Equation 2.56 represents multiple hyperplanes in this space for each ray-sum, and when a unique solution to the system exists, it will be the intersection of these hyperplanes. Consider the case of two variables f_1 and f_2 shown in Figure 2-17, which satisfy the following equations

$$\begin{aligned} w_{11}f_1 + w_{12}f_2 &= p_1 \\ w_{21}f_1 + w_{22}f_2 &= p_2 \end{aligned} \tag{2.57}$$

The process involved for determining the solution as shown in Figure 2-17 is to begin with an initial guess, project this first guess onto the first line, project the new point onto the second line, project this latest point onto the first again, etc. The iterations will always converge to the same point, if a unique solution exists.

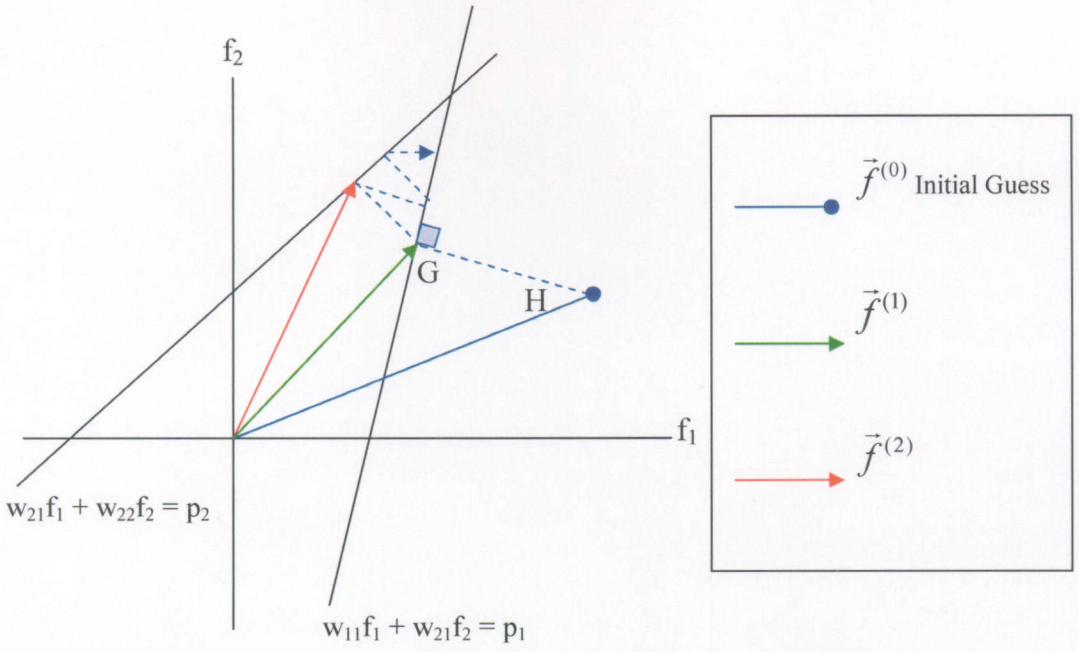

Figure 2-17: Kaczmarz's method of solving algebraic equations, shown for solving two unknowns. Starting with an initial guess, the point is then projected onto the first of the lines. The result is projected then onto the second line, re-projected onto the first, etc, until convergence is achieved [4].

Implementing this method on a computer begins making an initial guess. This is denoted by $f_1^{(0)}, f_2^{(0)}, \ldots, f_N^{(0)}$, or in vector format as $\vec{f}^{(0)}$ and is assigned a value of zero for all f_i's. The vector $\vec{f}^{(0)}$ is then projected onto the first equation, seen in Equation 2.57, to yield $\vec{f}^{(1)}$, which is projected onto the second equation in (2.58) to give $\vec{f}^{(2)}$ and so on. When $\vec{f}^{(i-1)}$ is projected onto the hyperplane given by the *i*th equation to yield $\vec{f}^{(i)}$, the process can be described mathematically by

$$\vec{f}^{(i)} = \vec{f}^{(i-1)} - \frac{\left(\vec{f}^{(i-1)} \cdot \vec{w}_i - p_i\right)}{\vec{w}_i \cdot \vec{w}_i} \vec{w}_i \tag{2.58}$$

where, $\vec{w}_i = \left(w_{i1}, w_{i2}, \ldots, w_{iN}\right)$ and $\vec{w}_i \cdot \vec{w}_i$ is the dot product of $\vec{w}_i$ with itself. To derive Equation 2.58, begin with the first entry in Equation 2.56

$$\vec{w}_1 \cdot \vec{f} = p_1 \tag{2.59}$$

Equation (2.59) represents the hyperplane that is perpendicular to the vector $\vec{w}_1$. This is shown in Figure 2-18 where $\overrightarrow{OD}$ is the same as $\vec{w}_1$.

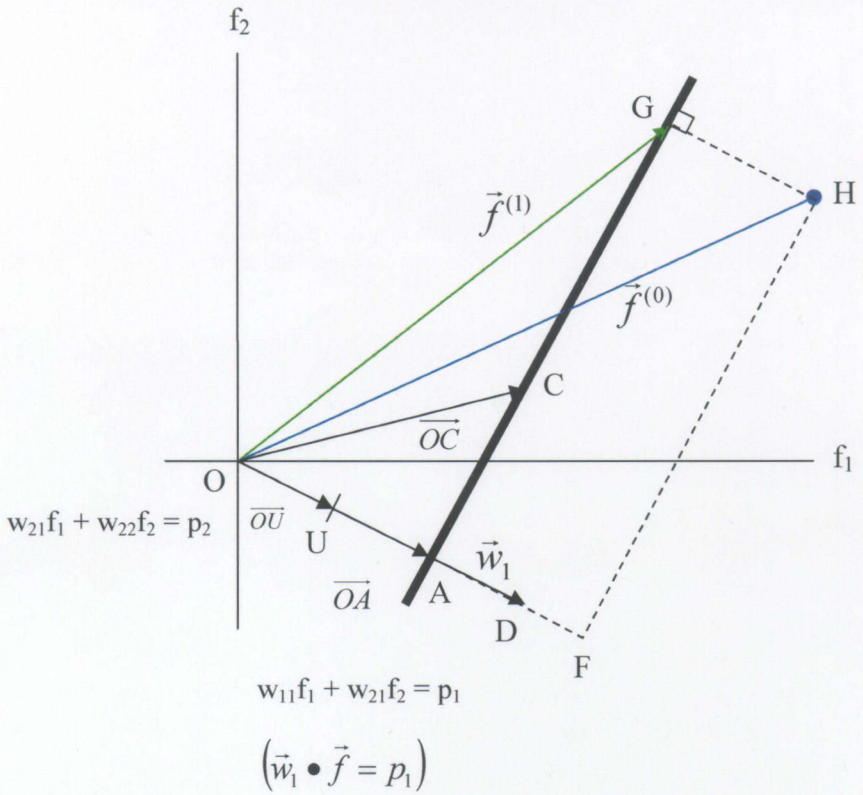

Figure 2-18: Plot of the hyperplane $\vec{w}_1 \cdot \vec{f} = p_1$ (represented by the bold line), which is perpendicular to $\vec{w}_1$.

Equation 2.59 states also that the projection of a vector $\overrightarrow{OC}$ (for any point C on the hyperplane) on the vector $\vec{w}_1$ is of constant length. The unit vector $\overrightarrow{OU}$ along $\vec{w}_1$ is given by

$$\overrightarrow{OU} = \frac{\vec{w}_1}{\sqrt{\vec{w}_1 \cdot \vec{w}_1}} \tag{2.60}$$

With that the perpendicular distance of the hyperplane from the origin is

$$\begin{aligned}\left|\overrightarrow{OA}\right| &= \overrightarrow{OU}\cdot\overrightarrow{OC} = \frac{1}{\sqrt{\vec{w}_1\cdot\vec{w}_1}}\left(\vec{w}_1\cdot\overrightarrow{OC}\right) \\ &= \frac{1}{\sqrt{\vec{w}_1\cdot\vec{w}_1}}\left(\vec{w}_1\cdot\vec{f}\right) = \frac{p_1}{\sqrt{\vec{w}_1\cdot\vec{w}_1}}\end{aligned} \tag{2.61}$$

To obtain $\vec{f}^{(1)}$, $\vec{f}^{(0)}$ is subtracted from $\overrightarrow{HG}$

$$\vec{f}^{(1)} = \vec{f}^{(0)} - \overrightarrow{HG} \tag{2.62}$$

where, the length of $\overrightarrow{HG}$ is

$$\begin{aligned}\left|\overrightarrow{HG}\right| &= \left|\overrightarrow{OF}\right| - \left|\overrightarrow{OA}\right| \\ &= \vec{f}^{(0)}\cdot\overrightarrow{OU} - \left|\overrightarrow{OA}\right|\end{aligned} \tag{2.63}$$

substituting for $\overrightarrow{OU}$ and $\overrightarrow{OA}$ yields

$$\left|\overrightarrow{HG}\right| = \frac{\vec{f}^{(0)}\cdot\vec{w}_1 - p_1}{\sqrt{\vec{w}_1\cdot\vec{w}_1}} \tag{2.64}$$

Because $\overrightarrow{HG}$ is in the same direction as the unit vector $\overrightarrow{OU}$, $\overrightarrow{HG}$ can then be expressed in the following form

$$\overrightarrow{HG} = \left|\overrightarrow{HG}\right|\overrightarrow{OU} = \frac{\vec{f}^{(0)}\cdot\vec{w}_1 - p_1}{\sqrt{\vec{w}_1\cdot\vec{w}_1}}\vec{w}_1 \tag{2.65}$$

substituting Equation 2.65 into Equation 2.62 yield the result found in Equation 2.59.

For real-world applications a large number of projections and reconstructions of large area (in the case of 2-D images) are necessary to achieve adequate results, problems with the calculation, storage and fast retrieval of the weight coefficients w_{ij} occur when using Equation 2.62 when this is the case. To construct an image of a size of 100x100

from 100 projections and 100 rays per projection, the number of minimum number of required weights would be 10^8, which can make fast storage and retrieval a problem when reconstruction speed is an issue.

The size that the weight matrix can grow to, under modest image sizes, has led to the development of multiple algebraic approaches to approximate Equation 2.58, in which three cases will be discussed, for the first Equation 2.58 will be re-written accordingly

$$f_j^{(i)} = f_j^{(i-1)} + \frac{p_i - q_i}{\sum_{k=1}^{N} w_{ik}^2} w_{ij} \tag{2.66}$$

where,

$$q_i = \vec{f}^{(i-1)} \cdot \vec{w}_i \tag{2.67}$$

$$= \sum_{k=1}^{N} f_k^{(i-1)} w_{ik} \tag{2.68}$$

Taking the (i-1)th solution is projected onto the ith hyperplane, the value for the gray level of the jth element is calculated by correcting the current value $\Delta f_j^{(i)}$ which is given by

$$\Delta f_j^{(i)} = f_j^{(i)} - f_j^{(i-1)} = \frac{p_i - q_i}{\sum_{k=1}^{N} w_{ik}^2} w_{ij} \tag{2.69}$$

Hence the p_i value is the measured ray-sum, q_i is the computed ray-sum based on the (i – 1)th solution. To find Δf_j for the j^{th} cell, the difference is calculated between the

measured and computed ray-sums, normalizing by $\sum_{k=1}^{N} w_{ik}^2$, then assigning this value to all of the cells within the i^{th} ray, each value weighted by the appropriate w_{ij}.

2.6.2.2 Algebraic reconstruction technique (ART), simultaneous iterative reconstruction technique (SIRT), simultaneous ART (SART)

For the greater part of ART implementations, the $w_{ik}'s$ in Equation 2.69 are replaced with 1's and 0's, which corresponds to the center of the k^{th} image cell being within the i^{th} ray. The denominator then is given by $\sum_{k=1}^{N} w_{ik}^2 = N_i$, or the number of cells whose center is within the i^{th} ray. $\Delta f_j^{(i)}$ is then given by

$$\Delta f_j^{(i)} = \frac{p_i - q_i}{N_i} \tag{2.70}$$

It follows in Equation 2.70 that the q_i's are still calculated using Equation 2.69, however the binary approximation for the w_{ik}'s is used instead. A relaxation factor λ is used to dampen correction overshoot, which generates salt and pepper noise because of the approximations for the $w_{ik}'s$. This factor lies in the interval [0,1], but usually is chosen to be much less than one. [20] The final form of $\Delta f_j^{(i)}$ is

$$\Delta f_j^{(i)} = \frac{p_i - q_i}{N_i} \lambda \tag{2.71}$$

SIRT uses Equation 2.70 as well, but in contrast does not update the value of the j^{th} cell immediately. Instead it computes the change $\Delta f_j^{(i)}$ in the j^{th} pixel for all equations

in Equation 2.56, and at the end of the iteration the change for each cell is the average value for all computed changes for that cell. This method provides superior reconstructions, however, with a loss in convergence speed.

SART can produce reconstructions of decent quality and numerical accuracy as quick as in a single iteration. To accomplish this traditional pixel basis is discarded in favor of bilinear elements in order to reduce errors in the approximation of ray integrals of a smooth image by finite sums. For circular reconstruction regions, partial weights are assigned to the first and last picture elements on each ray. The correction terms are then simultaneously applied for all the rays in one projection in order to further reduce the noise resulting from the inconsistencies associated with real projection data.

CHAPTER 3 : APPROACH

As mentioned previously, the goal of this thesis is to develop techniques for the synthesis of particle aggregates using algebraic reconstruction techniques from images obtained using optical microscopy and is broken down accordingly into four specific tasks.

1. Design and develop automated optical 3-D tomography system, for the shape characterization of particle aggregates.
2. Design and develop experimental protocols and databases of optical and X-ray tomography scans of a set of geomaterial aggregate mixtures.
3. Demonstrate the ability of the optical microscopy techniques to reconstruct 3-D shapes.
4. Demonstrate the consistency, separability and uniqueness of the 3-D shape-descriptor algorithm by exercising the method on a varying set of particle aggregate mixtures.

This chapter will address the issues with the current method of particle synthesis as well as provide a possible solution, and will be structured in the following manner; approach for the overall project, particle characterization, the tomographic reconstruction algorithm, particle synthesis, problems associated with current techniques, proposed optimized technique utilizing the Euclidean distance metric.

3.1 Overall research methodology

The overall project can be broken down into three major phases. The first phase is the determination of statistical 3-D descriptors that can be used to characterize entire sets of

aggregate mixes. Second, is to synthesize particle aggregates for all sets of mixes. The final phase of the project is to use the synthesized aggregates in a Discrete Element Model (DEM) for the purpose of predicting contact forces and shear strength. Figure 3-1 illustrates this process.

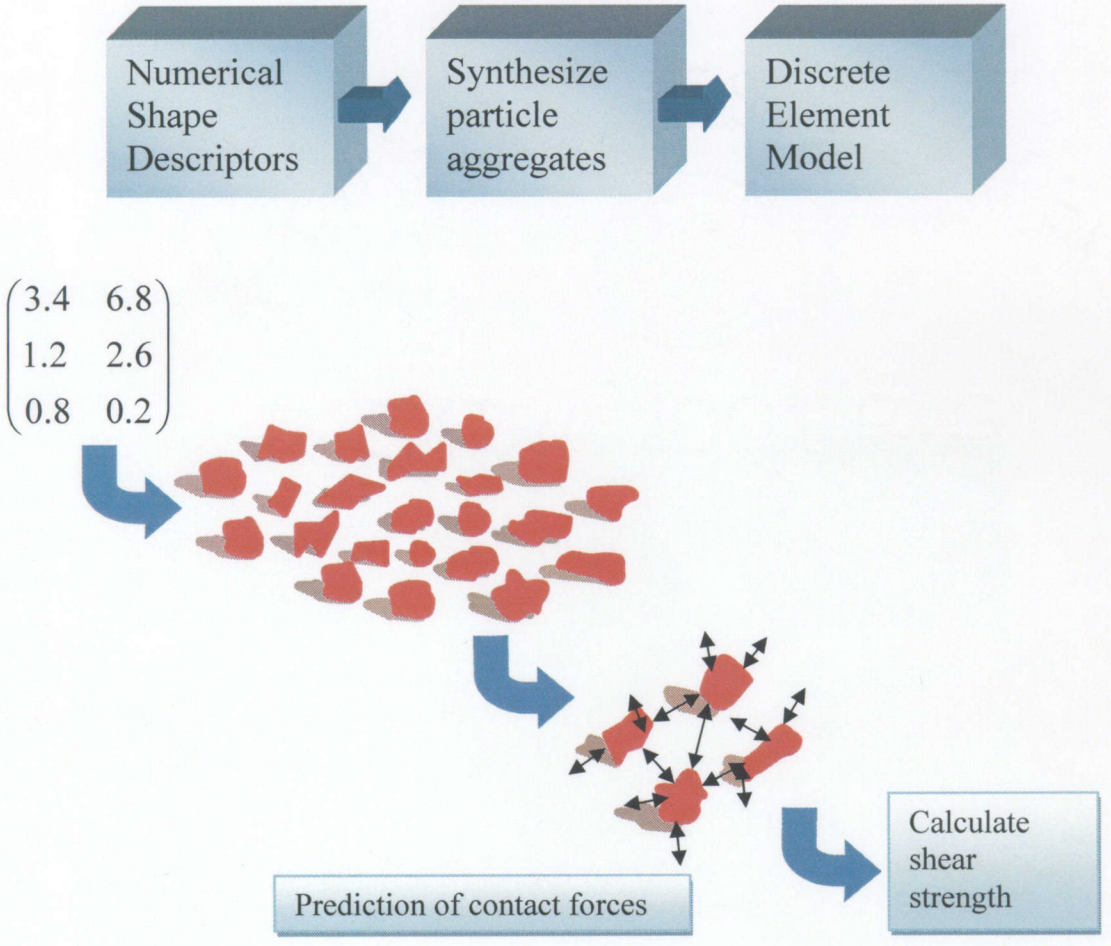

Figure 3-1: Overall approach for aggregate mix characterization, synthesis and discrete element modeling of shear strength and contact forces.

3.2 Particle characterization

Particle characterization is the first step in the overall approach with the determination of the 3-D descriptors done in [4]. The premise was that an aggregate mix could be represented statistically by a relatively small set of statistical 3-D descriptors. This goal was accomplished using a large number of 2-D images of particles, from the specific mix to be characterized. Each particle inside the image was then processed such that only the boundary of the object remained, then that boundary was "unrolled" by changing the coordinates of each boundary point, represented by the form (x , y), in the image into a complex quantity $x + jy$, by setting the "x" axis to the real component and setting the "y" axis to the imaginary component. This boundary conversion in complex coordinates allowed for the boundary to be expressed as a periodic, 1-D function, since the starting point is also the ending point. In order to ensure scale invariance and for direct coefficient comparison between different particles to be possible, each 1-D function had to be re-sampled and the amplitude normalized. The preceding procedure ensures that images with the same *shape* will produce the same Fourier coefficients, regardless of scale; satisfying the invariance condition set forth in earlier in this thesis. To transform these 1-D functions into the frequency domain, the Discrete Fourier Transform (DFT) is used, and is described in Equation 3.1

$$X_n = \sum_{k=0}^{N-1} x_k e^{-j2\pi kn/N} \tag{3.1}$$

where x_k is the original 1D function, X_n is the transformed function, N is set for the total number of samples, and both n,k each range from 0,1,...N-1.

Principal Component Analysis (PCA) is then used to reduce the number of descriptors which fulfills the requirement of parsimony, which states that the algorithm should use the smallest possible set of numbers to describe a particular shape. PCA will reduce the descriptor values overall noise susceptibility, which is accomplished by using Equation 3.2

$$\vec{x} = \vec{m} + \sum_{i=1}^{d'} a_i \vec{e}_i \tag{3.2}$$

where, $\vec{x}$ is the transformed data set, $\vec{m}$ is the mean vector of the original data, a and e are the eigenvalues and eigenvectors of the scatter matrix (*number of images * covariance of the data*) of the original data, and $d \leq d'$, d being the dimensionality of the transformed data.

The final descriptor values are then used to calculate the mean and variance for each descriptor D_1, D_2... D_n, where n is the total number of descriptors used to adequately describe the shape of the particle. The descriptors are then assumed to be statistically independent of each other, which has been tested and proved in [4]. The descriptors may then be used to synthesize sets of 2-D projections and ultimately 3-D particle synthesis models [4]. Figure 3-2 illustrates the concept of sand particle characterization and the premise behind particle synthesis.

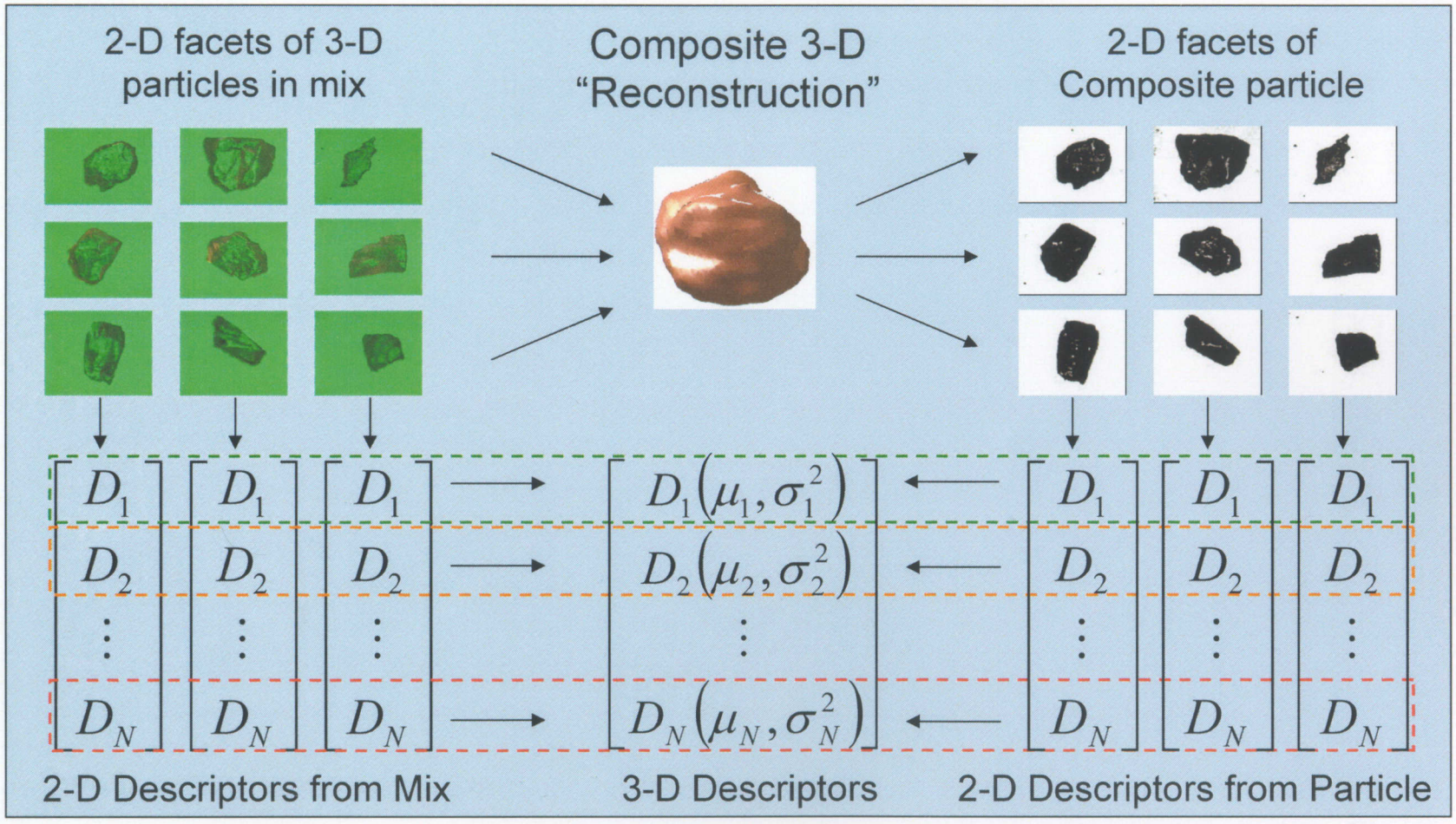

Figure 3-2: Approach for sand particle characterization using the 3-D statistical descriptor technique.

3.3 Tomographic reconstruction

To ultimately synthesize particles, a reconstruction algorithm is necessary. The algebraic reconstruction technique (ART) was chosen for the optical and microscopy systems since it is a constrained optimization method, such that the solution is the best fit for the given set of constraints. ART allows for a solution even with poor input projections and missing angular data. 2-D ART is given by Equation 3.3

$$\Delta f_j^{(i)} = f_j^{(i)} - f_j^{(i-1)} = \frac{p_i - q_i}{N_i} \tag{3.3}$$

where, $\Delta f_j^{(i)}$ is the correction to the j^{th} cell, $f_j^{(i-1)}$ is $(i\text{-}1)^{th}$ solution, $f_j^{(i)}$ is the i^{th} solution, p_i is the measured ray-sum along the i^{th} ray, q_i is the computed ray-sum for the same ray based on the $(i\text{-}1)^{th}$ solution, and N_i is the number of image cells whose centers are within the i^{th} ray. 3-D models are created by reconstructing 2-D slices of the object, given by the set of projections, and then stacking the resulting cross sections to create the 3-D model. Figure 3.3 illustrates this concept.

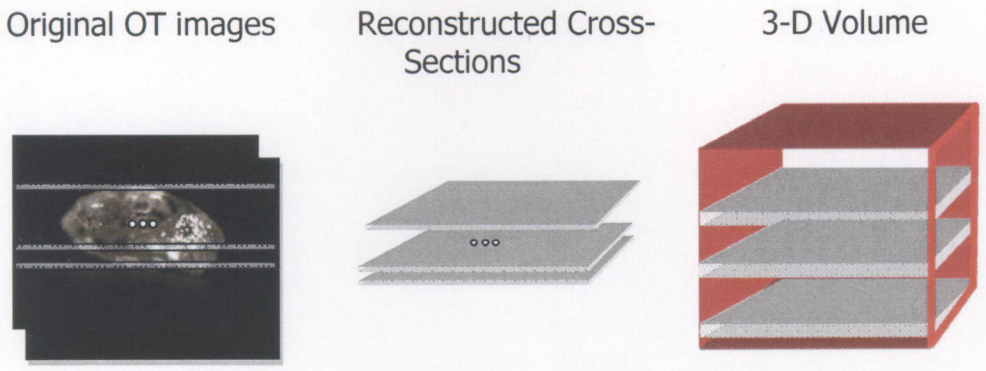

Figure 3-3: Illustration of the process of 2-D ART to create 3-D objects. Every row of pixels is treated as a set of 1-D projections. ART is then preformed of each set and thusly 2-D slices of the final 3-D object are created. The final step is to stack the reconstructed cross-sectional images.

3.4 Particle synthesis

Particle synthesis is the process in which 2-D projections are randomly generated to create composite 3-D particles. To create the random projections, statistical information must be extruded from the individual particle aggregate mixes. Each synthesized projection must retain the generalized shape parameters of the mix. For example, a random projection from the Dry #1 sand mix must be separable from a projection randomly generated from the statistical information from the Rhode Island mixture. Values for the Fourier descriptors are randomly generated by using a Gaussian distribution specific to the aggregate mixture being evaluated. This distribution produces the 1-D Fourier transform of the "unrolled" boundary for a projection. The inverse Fourier Transform is then calculated, the 1-D function is truncated so it is no longer periodic, and then "rerolled" to form the 2-D boundary. To create an image, the boundary is filled, resulting in a 2-D projection of a particle. After the desired number of

projections has been created, they are combined using a tomographic reconstruction algorithm to synthesize the final particle. Figures 3-4 and 3-5 illustrate the projection generation process from the beginning.

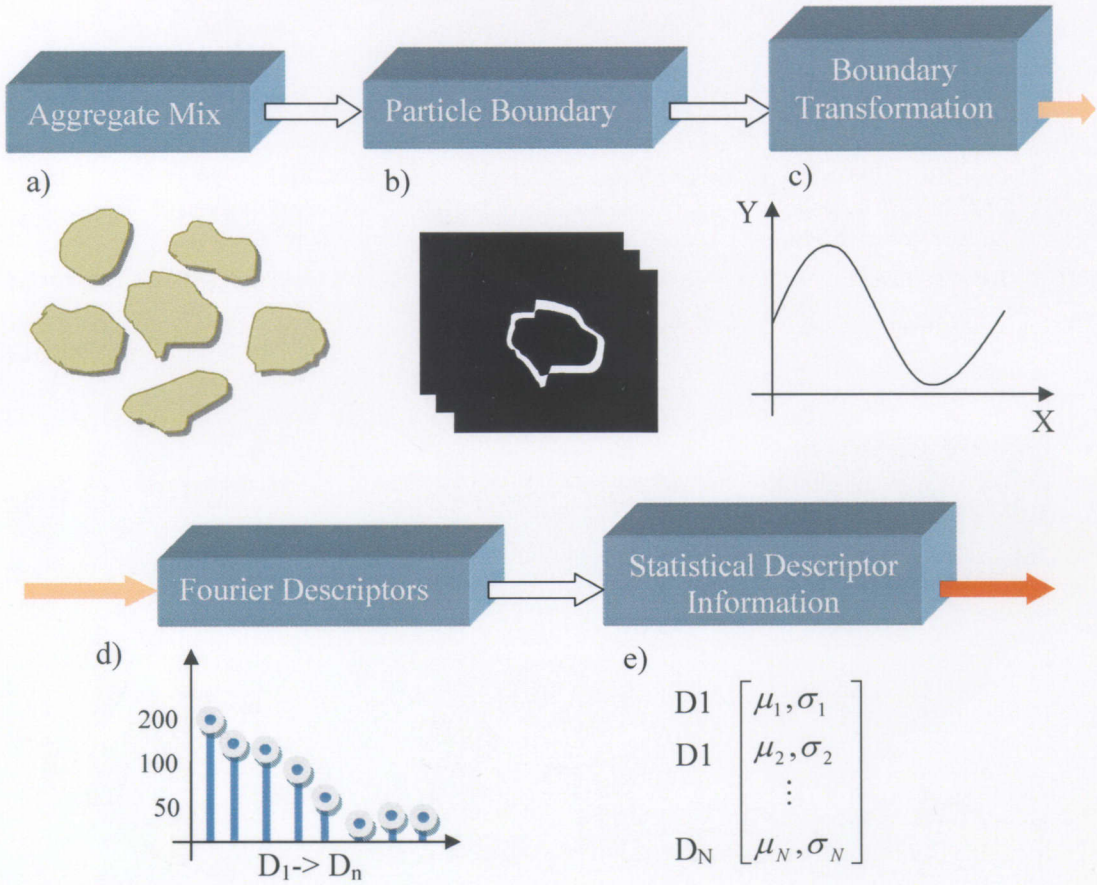

Figure 3-4: Illustration of the first phase of particle synthesis. a) A specific particle aggregate mixture is chosen. b) Multiple images from the mixture are taken and the boundary of the object is isolated. c) The boundary is un-rolled to a 1-D periodic function. d) The 1-D function is processed by the Fourier transform, this occurs for all images. Principal component analysis is performed to lower the dimensionality of the Fourier descriptors for each boundary image. e) The means and the variances for each descriptor over the entire mix are recorded for synthesizing 2-D images.

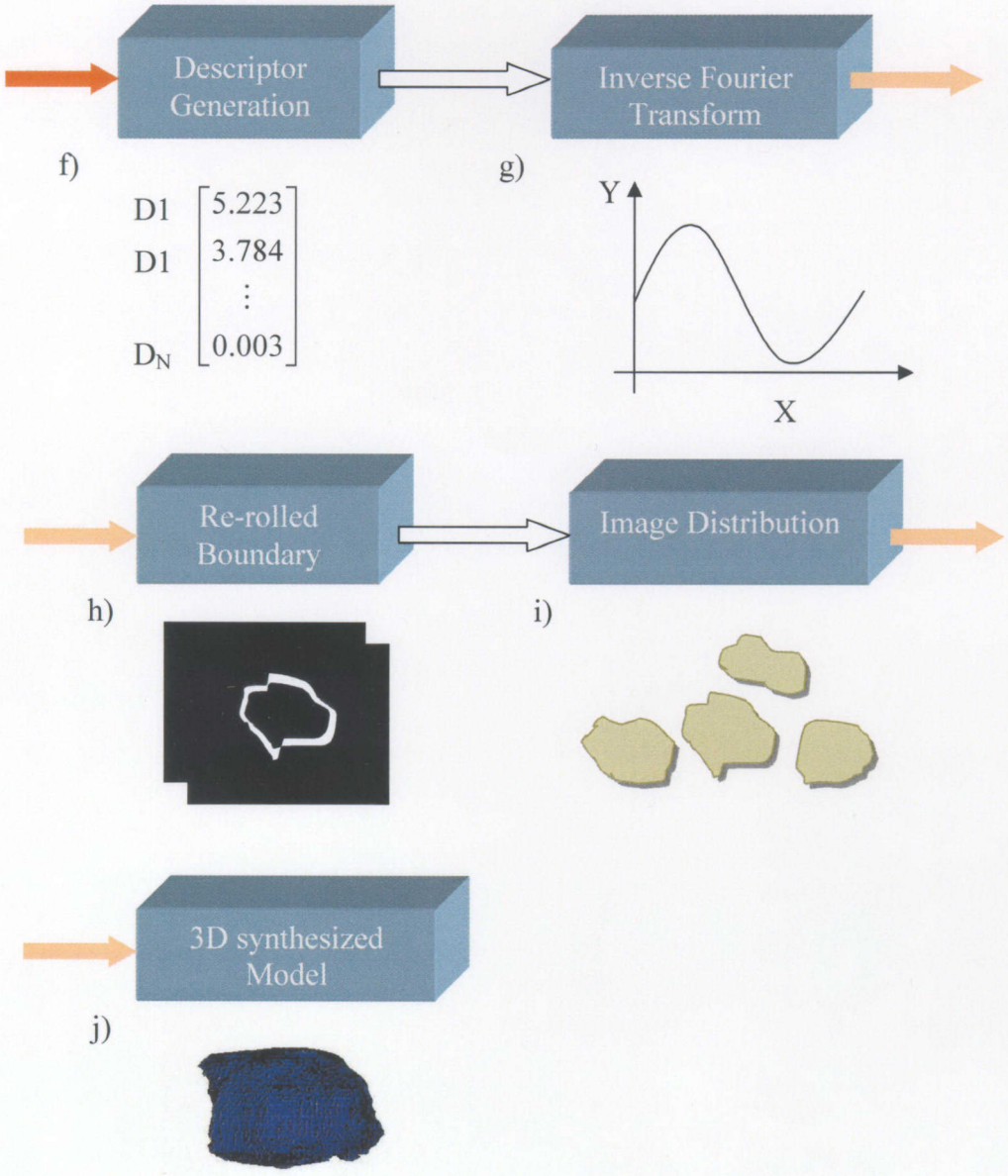

Figure 3-5: Final phase of particle synthesis. f) Based on the Gaussian distribution random descriptors are generated that fall within the parameters of the aggregate mix. g) The descriptors are then passed through the inverse Fourier transform. h) The 1-D function is then re-rolled into the boundary image of the new synthesized particle. i) To create multiple images steps f) through i) are repeated until the necessary number is aquired. j) The final 3-D, synthesized particle, is created using the ART mentioned section 3.3.

3.5 Issues associated with previous particle synthesis methods

There exists within the generation of synthesis particle models, a problem that ultimately results in a severe loss of surface resolution and whose 3-D models show no statistical difference when compared against the synthesized models from different aggregates. Previous work has validated that the optical tomography system in tandem with ART, can produce models that are statistically similar to the X-ray computed tomography system. The 3-D synthesis models in contrast to the OT models are created using the optical microscopy (OM) system which captures projections that consists of hundreds of images each of different particles. These 2-D images are no different from the images captured from the optical tomography system which deals with a single particle at multiple projection angles. The goal is to take the necessary number of images from a specific mix and use them as the 2-D projections for ART. Currently, the projections are chosen at random, however this selection procedure poses a significant problem: there is nothing stopping the outliers from being selected consequently causing poor reconstructions. The following is a result of having a high variance in the size metrics of two images. Figure 3-6, shows a random selection of projections and the resulting high variance in sizes.

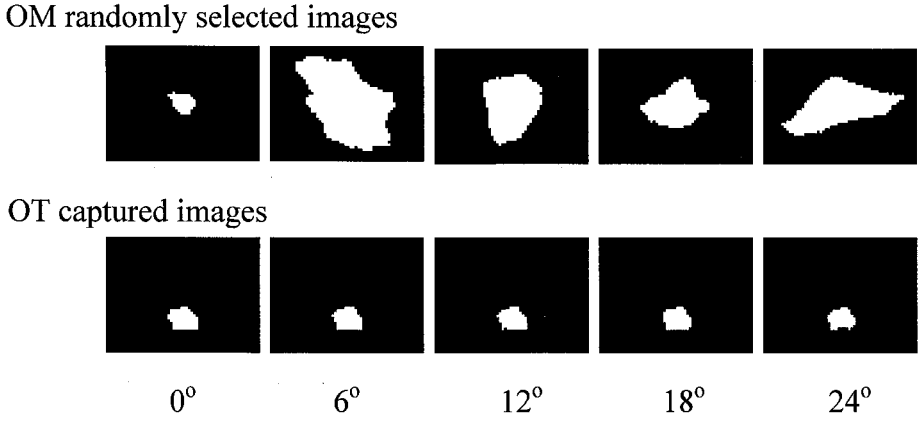

Figure 3-6: Observed size variance for OM images.

As mentioned in section 3.3. The 2-D ART algorithm takes a single row of pixels from the object and treats it as a 1-D projection, so that the 2-D cross section can be formed. When the top of the smallest image is reached, there no longer exists data for that specific projection angle which will provide less information for the cross section calculation and ultimately cause the reconstructions to become poorly synthesized as seen in Figure 3-7.

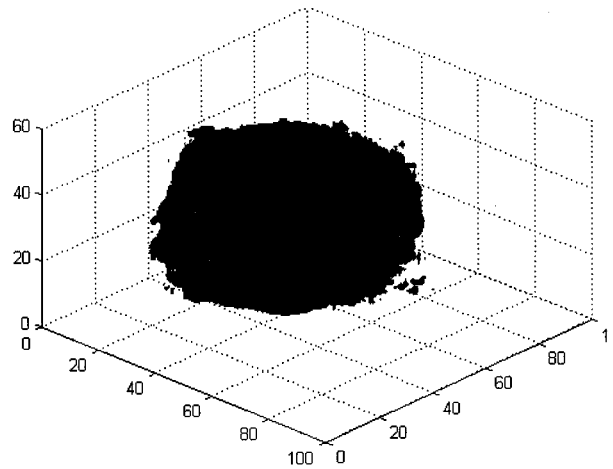

Figure 3-7: A poorly synthesized Daytona Beach sand particle, created using random OM projections.

3.6 Proposed optimization technique for particle synthesis

A possible solution to the aforementioned problem is to best correlate the known angles from an OT set of images to that of the images found in the OM dataset. Previous work has shown the ability of ART to adequately reconstruct a model from the 2-D images captured on a scanning platform, to that of a high-end X-ray scanner which creates accurate models of the specimen. The information stored between the projection angles of the OT image set can be used in selecting proper OM images, allowing for an evaluation of the ability of ART to work in the case of particle synthesis. The imposed minimum required number of images for the ART is 60, which is taken every 6^{o} from 0^{o} to 360^{o}. This interval allows for reduced redundancy in the projection data. Each image will go through the process of finding the boundary and calculating the Fourier descriptors. To find the best set of 60 images from the OM set, the same Fourier descriptor technique is employed on the 300 OM images, and a total of 128 descriptors are calculated for each image where the first 32 are used for comparison purposes. The scale invariance, as well as rotation invariance, ensures that we get the best optimized match for the boundary of the OT image. Each OT image is then checked against the entire OM database to find the best fit. To accomplish this, the shortest possible distance must be achieved between the real and imaginary components of the Fourier descriptors between the OT and OM images where each of the 32 descriptors has been assigned an equal weight in the determination of the shape of the particle. The sum of the distances between the real components and the imaginary components will yield the overall total distance, which is summarized in Equation 3.4.

$$a_{mn} = \sum_{i=1}^{32} \sqrt{(D_i b_{m_{"real"}} - D_i a_{n_{"real"}})^2 + (D_i b_{m_{"imj"}} - D_i a_{n_{"imj"}})^2} \quad (3.4)$$

where,

a_{mn} is the matrix of distances, n is the current OT image, m is the current OM image and n runs from 1-60 while m runs from 1-300. D_i stands for the descriptor value with i running from 1-32. b and a stand for OM an OT respectively. The real and imaginary values for each the OT and OM are calculated over i number of descriptors denoted by D_i.

The distance value a_{mn} is recorded for each OT image for a corresponding OM image. Each OM image is tested against all of the OT images forming a matrix of distances as seen in Figure 3-8.

$$\begin{pmatrix} a_{11} & \cdots & a_{1n} \\ \vdots & \ddots & \vdots \\ a_{m1} & \cdots & a_{mn} \end{pmatrix}$$

Figure 3-8: Illustration of the resulting distance matrix formed by Equation 3.4.

The selection procedure starts at the first OT image, where the shortest Euclidean distance between the descriptors is found. The chosen OM image will then be taken out of the selection procedure and will result in the top 60 OM images that most closely resemble a known successfully reconstructed OT model, allowing for ART to be

evaluated for particle synthesis. The overall procedure for this process is illustrated in Figure 3-9.

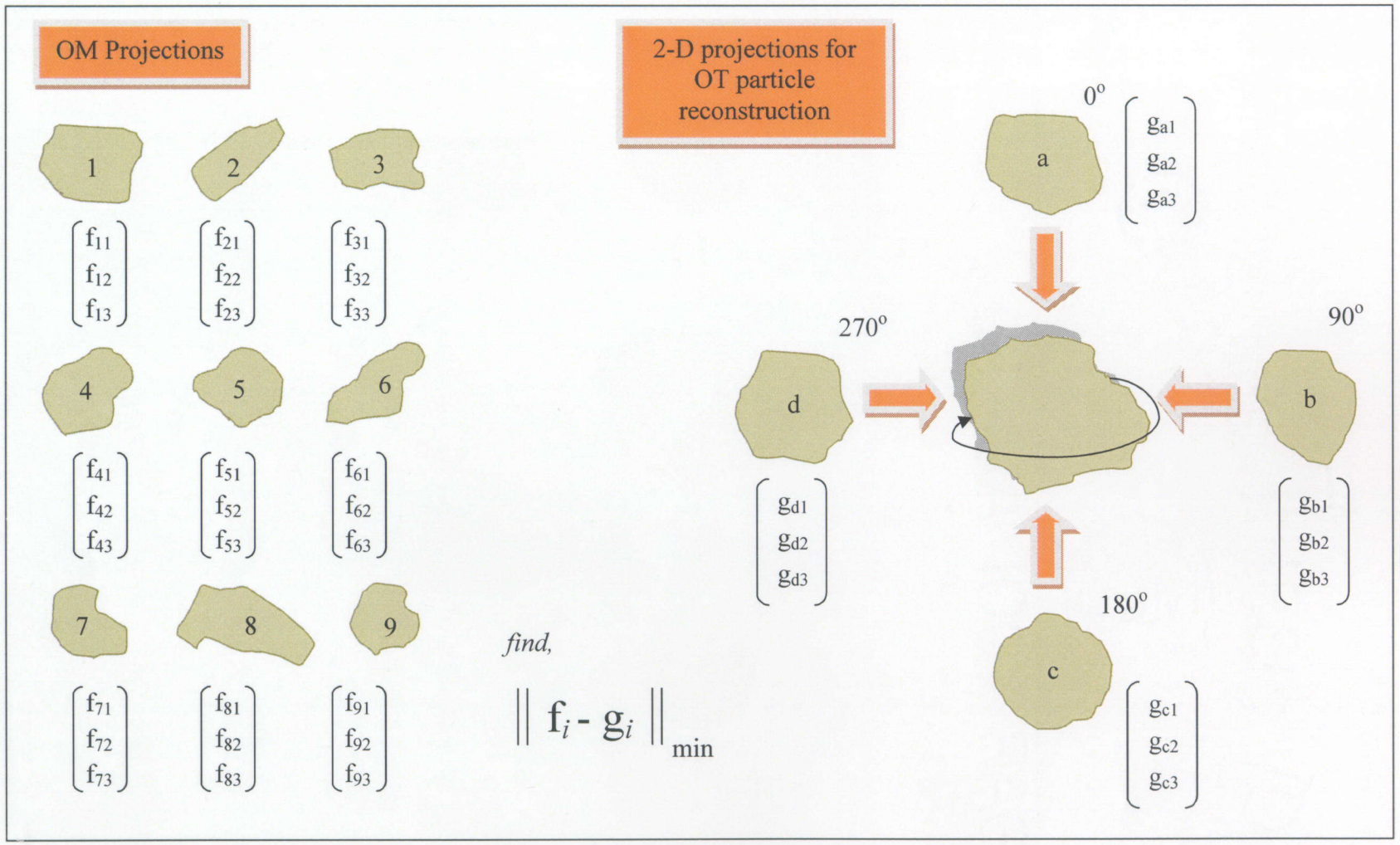

Figure 3-9: Illustration of the improved synthesis selection procedure.

CHAPTER 4 : RESULTS

To test the synthesis procedure, three primary systems must be designed and optimized; the OT, OM and X-ray CT system and will also be crucial in the formation of a comprehensive online database. This section will be outlined in the following way: OT system, X-ray CT system, OM system, online database, synthesis results, validation tests, and discussion.

4.1 OT system

The first system that will be addressed is the optical tomography system (OT). Figure 4-1 shows the OT system used to capture the projection data.

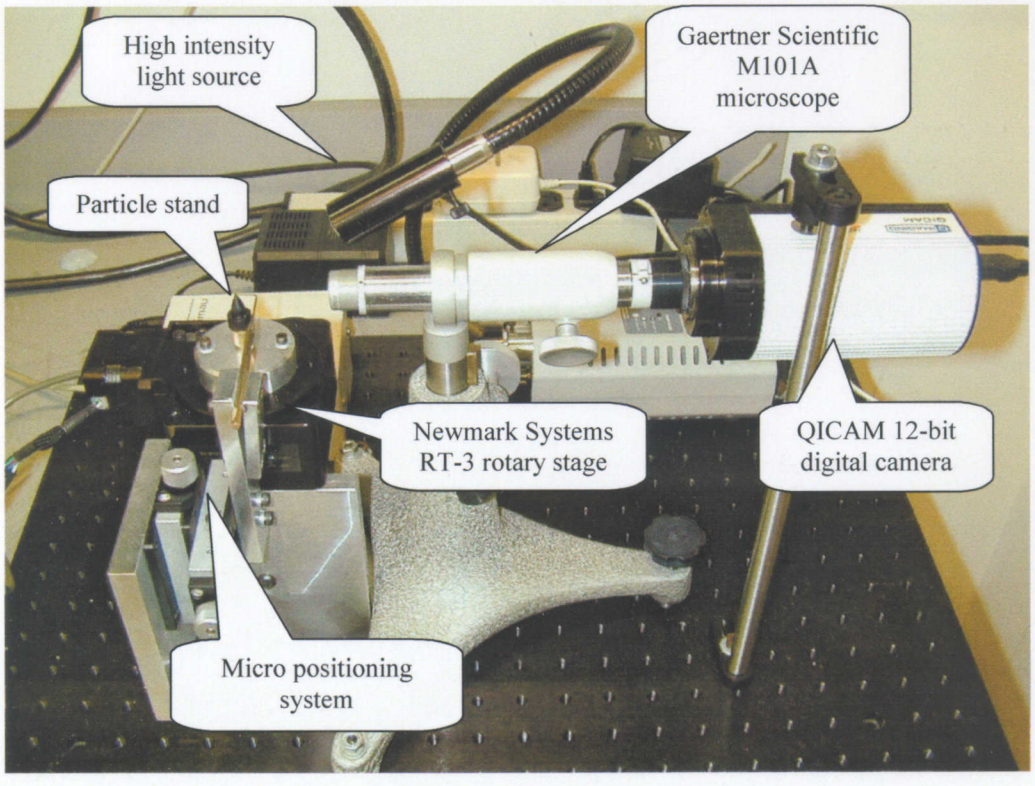

Figure 4-1: The optical tomography system. A single particle is rotated to create multiple images at different angles for the full rotation of the particle.

The OT system consists of a QICAM 12-bit digital camera, a Gaertner Scientific M101A microscope, and a Newmark Systems RT-3 rotary stage. The particles are placed on an aluminum base that has been painted flat black, to reduce reflections, and are mechanically centered using a high precision X-Y stage and stylus system. This system allows for the imaging of sand particles at 360° around the *z*-axis. Figure 4.2 shows the typical output of the scanning procedure of the OT system.

Figure 4-2: Michigan Dune sand particle. For illustration purposes every 60° is shown. The actual system outputs in 1° increments for a total of 360 images.

The OT system works by capturing the light transmitted and scatted through the object and reconstructing the volumetric model using ART. Since light is being used the system is very sensitive to external light sources which act as noise, and create low contrast areas that are very difficult to fix after the scanning is complete. To address this situation a light interference, sealed box has been designed to eliminate dust particles and ambient light from corrupting the scanning procedure.

4.2 X-ray CT system

The X-ray computed tomography (CT) system is the "gold standard" of reconstructions. This system is a desktop version of typical CAT scanners used in medical facilities which provide high resolution detailed reconstructions, while maintaining the internal structure

of the scanned object. The scanning system used for this work is the SkyScan 1072 X-ray microtomograph seen in Figure 4-3

Figure 4-3: Skyscan 1072 X-ray microtomograph.

To reconstruct a 3-D object, 3-D information is required. 2-D information cannot be used directly, thus, processes like algebraic reconstruction have been developed in an attempt to create the 3-D information from the 2-D projection data. To reconstruct a 3-D object, an infinite set of cross sections are needed such that when they are stacked they would form the 3-D structure. An X-ray system works by producing 2-D shadow images, as seen in Figure 4-4, of the complete internal structure of a 3-D object.

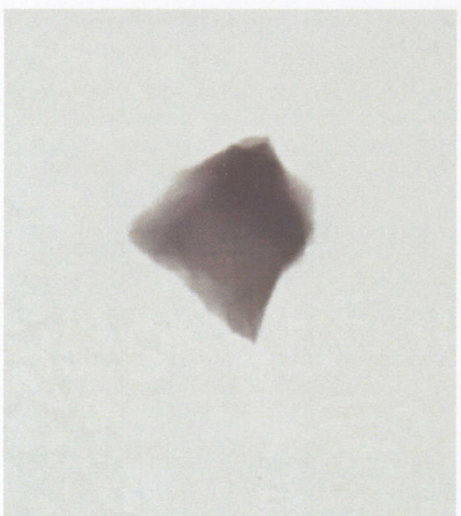

Figure 4-4: x-ray projection of a Michigan Dune sand particle.

The captured 2-D shadow images are created as the X-rays pass through the object and the gray level value is recorded which corresponds to the radio density of the object. As the object is rotated around a fixed axis more shadow images contribute information of the internal structure of the object. The simplest case can be seen in Figure 4-5 for parallel beam computed tomography.

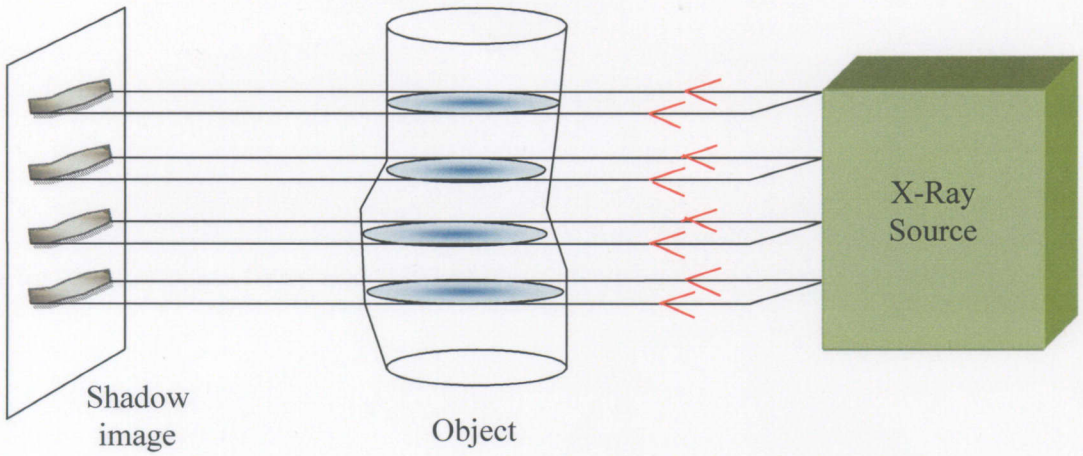

Figure 4-5: Illustration of parallel beam x-ray capture of a shadow projection for one angle, fewer slices are shown for illustration purposes. In practice, shadow images appear as in Figure 4-4.

The x-ray system will rotate the object for 180° and use the shadow projections to create the cross sections. Only 180° of rotation in necessary to acquire the entire structure of the object since X-rays pass completely through the object, thus any angle past 180° becomes redundant data, necessary only when the upmost accuracy is required.

4.3 OM system

The optical microscopy (OM) system evaluates multiple particles of the same mix simultaneously and then uses that data to synthesize a particle which is indicative of a specific aggregate mixture. The OM images are captured by scattering particles on a slide dish, using a Nikon Coolpix950 2 Megapixel camera and a Nikon TS100 microscope. Figure 4-6 is a photograph of the system setup.

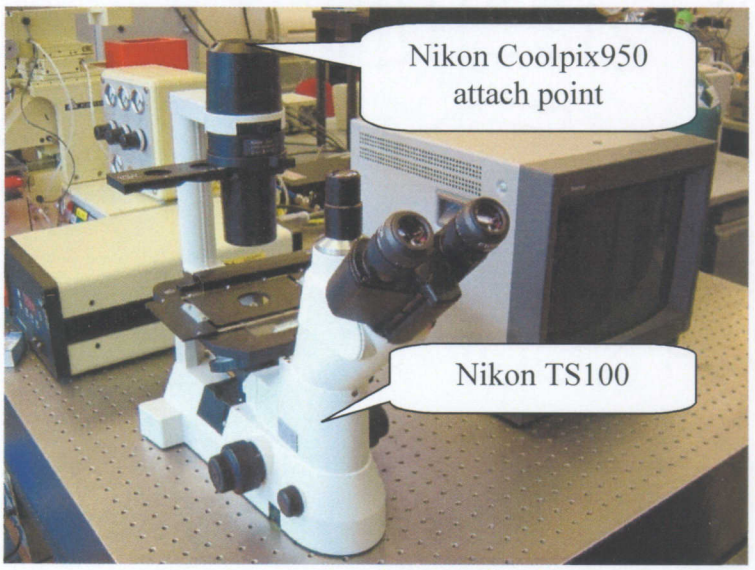

Figure 4-6: OM system setup. The screen to the right of the microscope is used to view the particles and is attached to the digital camera.

The unprocessed images that are taken from this setup can be seen in Figure 4-7. The image background is set to green for easy removal, and better contrast. Images are also processed such that the centroid of the object is the same for all the images.

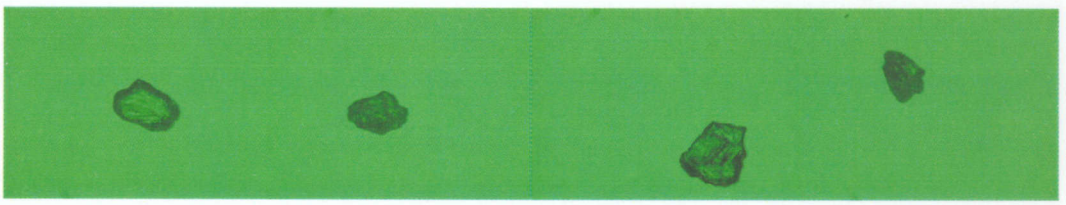

Figure 4-7: Daytona sand particles captured using the OM system setup seen in Figure 3-10.

It is these images, after processing, that will ultimately be substituted for the OT images used with the ART algorithm, allowing for a synthesized composite particle to be created.

4.4 Online database

The comprehensive online database houses the seven different particle aggregates that have been evaluated. This database allows the work done in this thesis to be shared with collaborating universities and will be hosted through the Rowan University college of engineering. The database is split into two primary categories; the computed tomography and optical microscopy systems. Figure 4-8 shows the hierarchy of the online database.

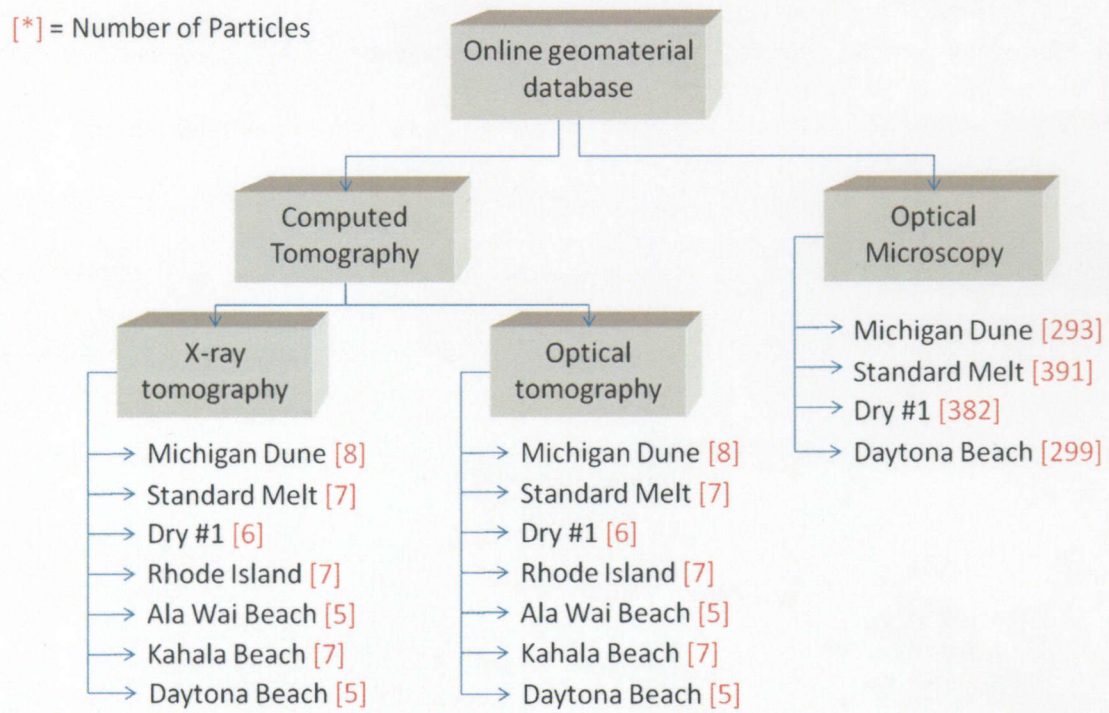

Figure 4-8: Hierarchy to illustrate the different systems as well as the particle groups that make up the online geomaterial database.

Each block in the above diagram contains from start to finish all of the 3-D modeling as well as accompanying raw data. The computed tomography → X-ray tomography block contains the following images and models as seen in Figure 4-9.

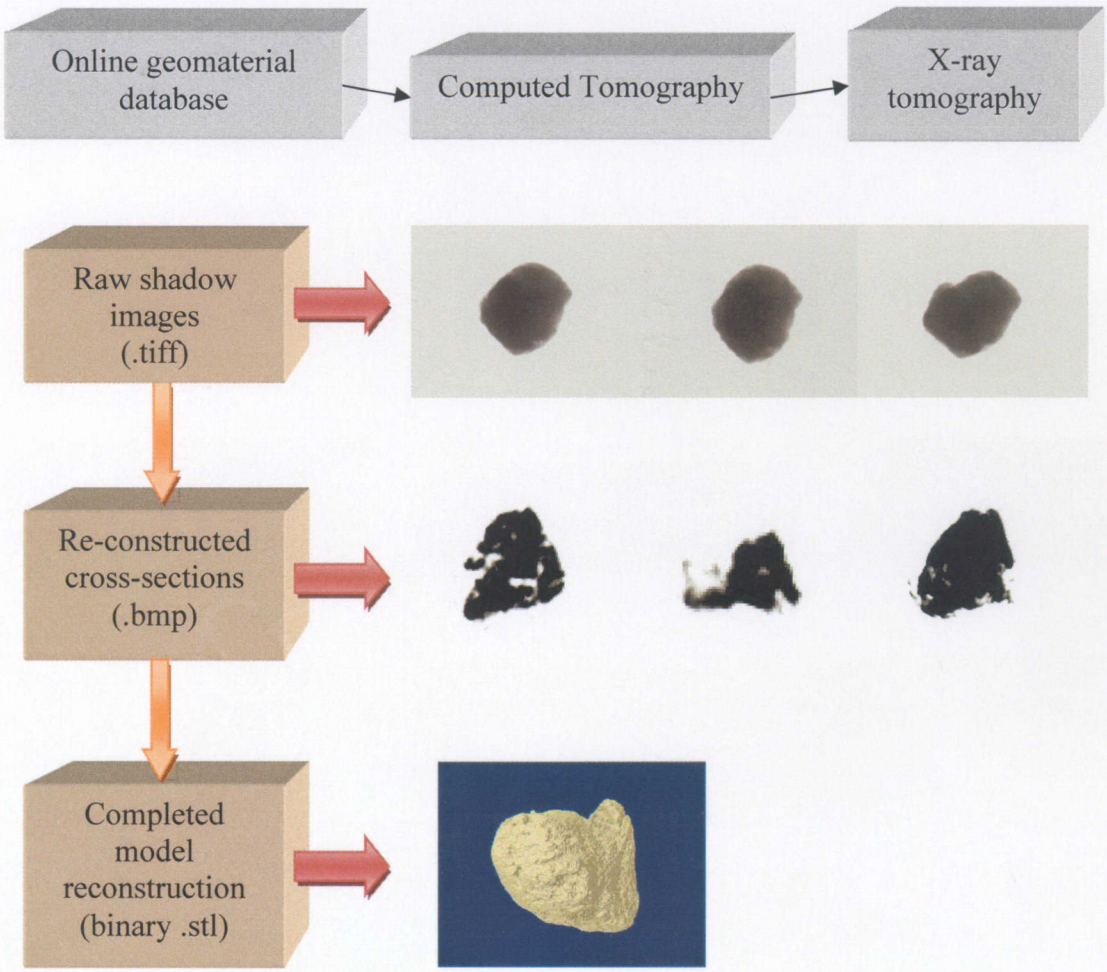

Figure 4-9: Layout of the X-ray tomography database.

The optical tomography folder is set up in a similar way, with the primary difference being the inclusion of the algorithms used to process the raw images and the

resulting MATLAB data files. These files have been specifically written such that a user only has to provide which aggregate mixture is being used, and then all the processing and model creation is completed. All MATLAB model files have been supplemented with more detailed visual reconstructions. This was accomplished by converting the models using MAYA, a 3-D modeling program. The supplemental models will allow for programs that are specifically designed for 3-D modeling to visualize the data. Figure 4-10 shows the overall layout of the optical tomography folder.

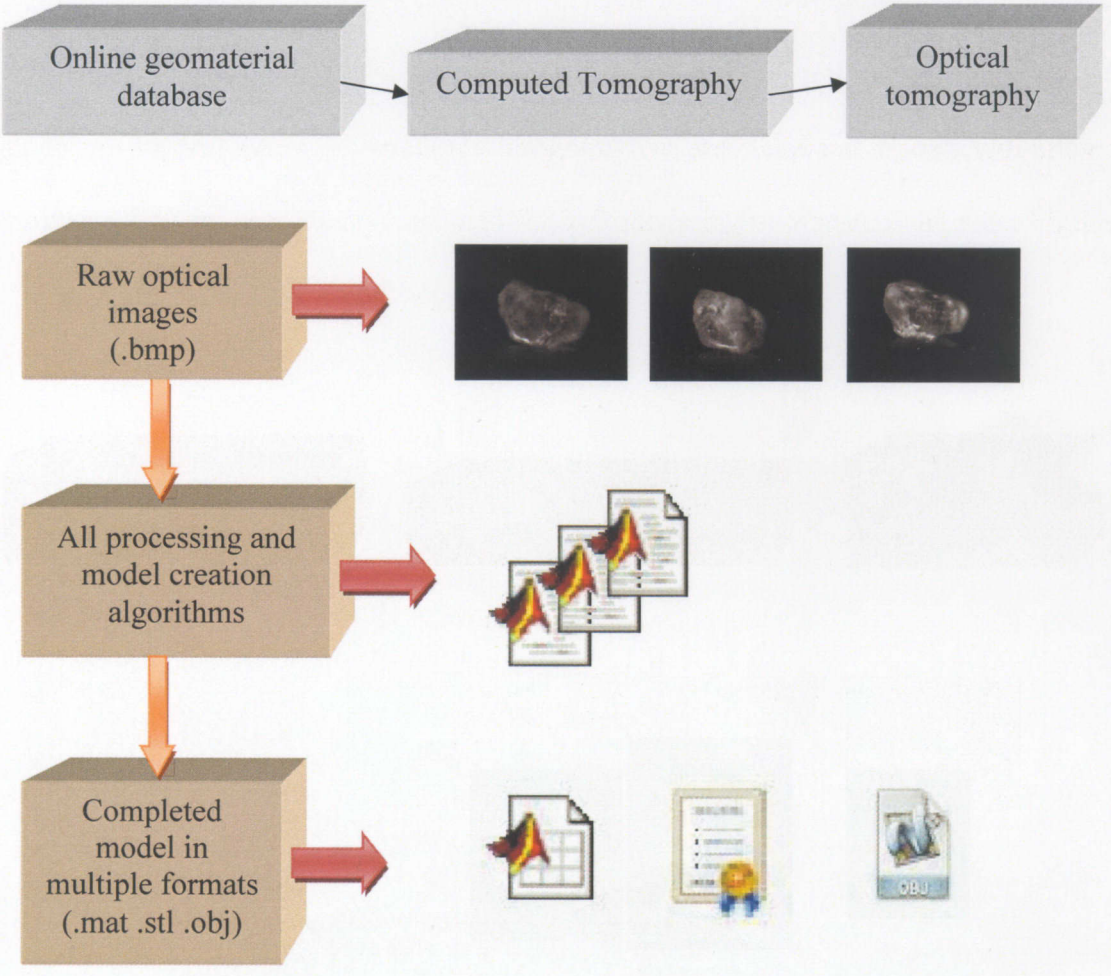

Figure 4-10: Layout of the optical tomography database, and supplied components.

The final subset of the online database is the optical microscopy system. This set of data includes all of the raw images captured with the OM system as well as an assortment of processing code. Figure 4-11 shows this layout.

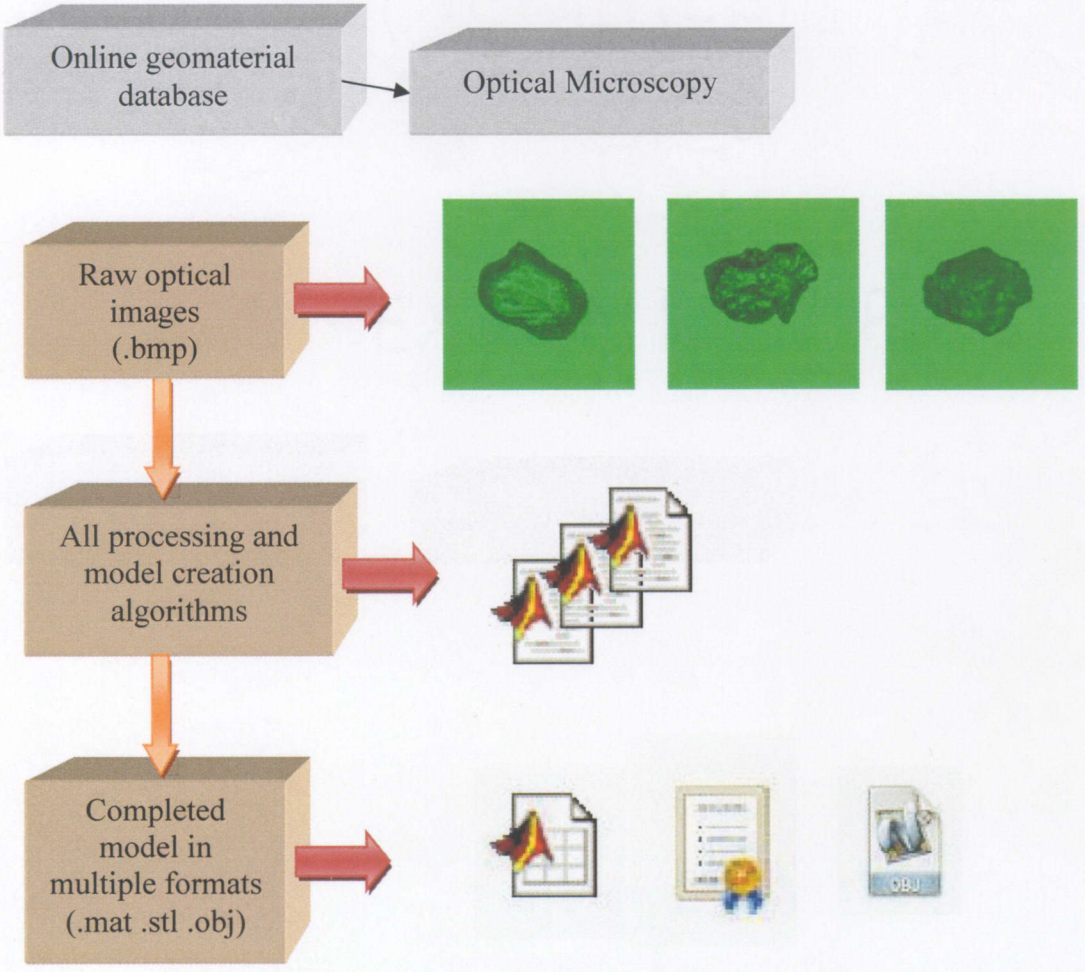

Figure 4-11: Illustration of the optical microscopy subset of the online geomaterial database.

4.5 Synthesis results

A total of four aggregate sand mixtures will be used to study the effects of the new synthesis procedure; Daytona Beach, Dry #1, Michigan Dune, and Standard Melt. Each mixture contains multiple test cases, and will be accompanied by an ellipsoid model which is generated by taking the images that make up the 3-D model and looking at the variances of the first three descriptors, using the data to create a radius in a certain direction. The x direction is controlled by the variance of the first descriptor, the y direction, by the variance of the second descriptor, the z direction, by the variance of the third descriptor and finally the center of the ellipsoid is the mean of the three descriptors. This can be seen illustrated in Figure 4-12.

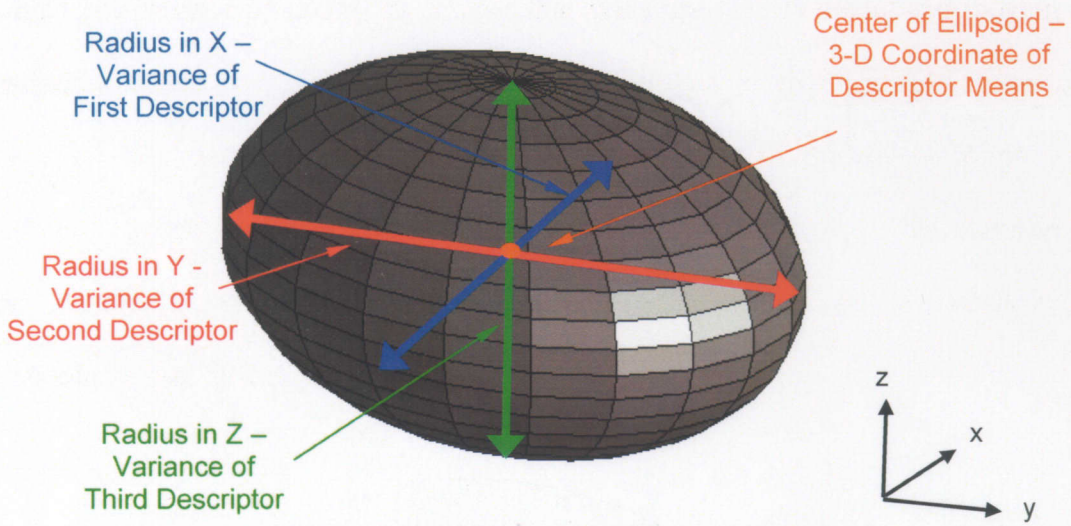

Figure 4-12: Illustration of the ellipsoid model.

4.5.1 Daytona Beach

The naming standard for the particles used in the database is the date in which the particles were scanned. The first particle seen in Figure 4-13, is DB 5/16/2005. The three

particle reconstructions seen in Figure 4-13, show the "true" X-ray reconstruction versus the previously validated OT reconstruction versus the OM reconstructions, whose projections were chosen based upon the best possible fit to the corresponding angle of the OT projections.

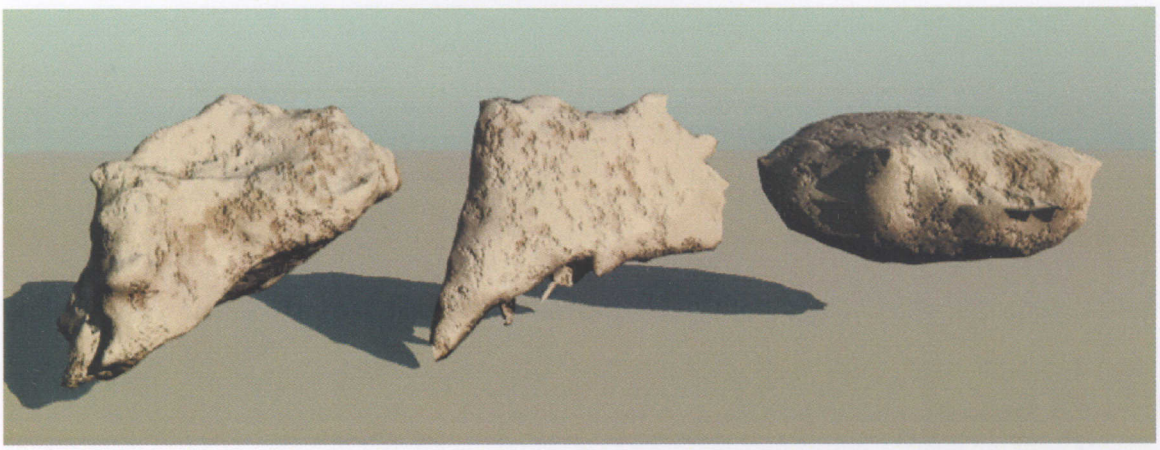

Figure 4-13: DB 5/16/2005- From left to right: X-ray CT, OT and synthesized OM reconstructions.

The following Figures 4-14, and 4-15 are the ellipsoid models corresponding to the three reconstructions.

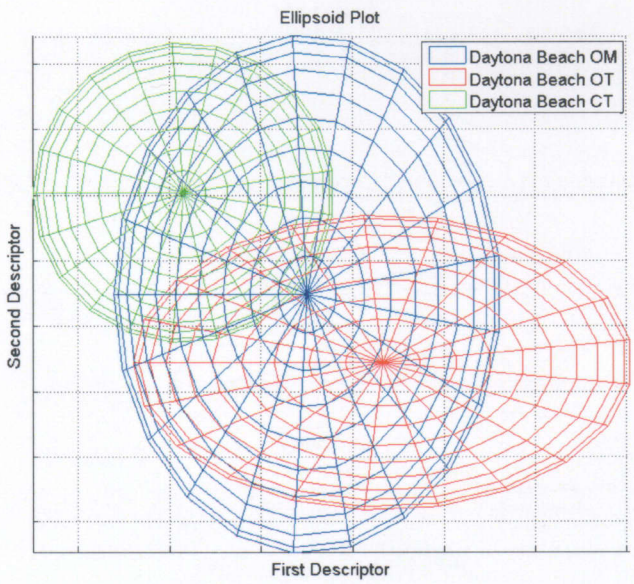

Figure 4-14: The DB 5/16/2005 ellipsoid model illustrating the X-ray CT, OT, and OM descriptor variances.

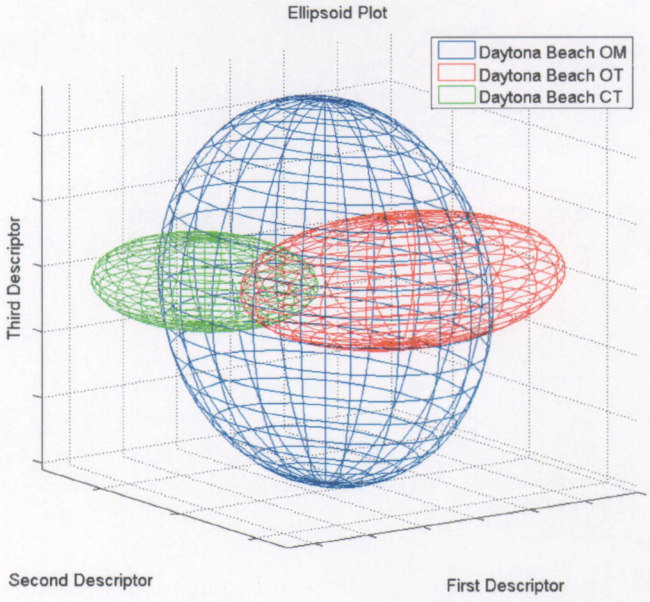

Figure 4-15: Alternate view of DB 5/16/2005 ellipsoid model illustrating the X-ray CT, OT, and OM descriptor variances.

The next Daytona Beach particle, DB 5/31/2005 can be seen in Figure 4-16.

Figure 4-16: DB 5/31/2005- From left to right: X-ray CT, OT and synthesized OM reconstructions.

The corresponding ellipsoid model can be seen in Figures 4-17 and 4-18, Figure 4-18 is an alternate view of the same ellipsoid model seen in Figure 4-17.

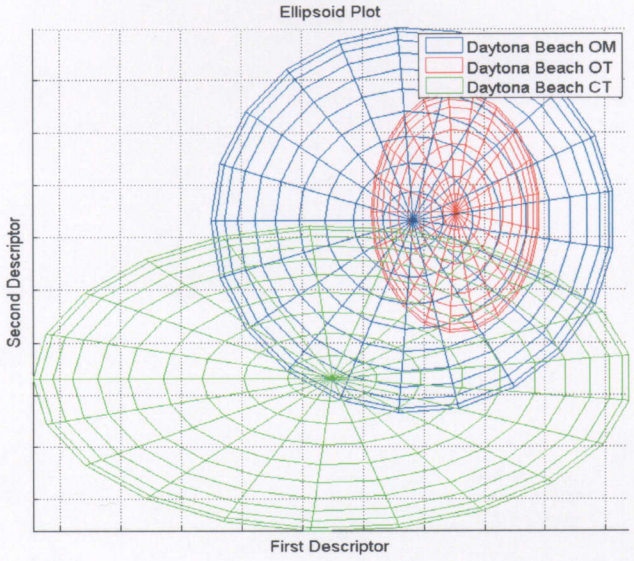

Figure 4-17: The DB 5/31/2005 ellipsoid model illustrating the X-ray CT, OT, and OM descriptor variances.

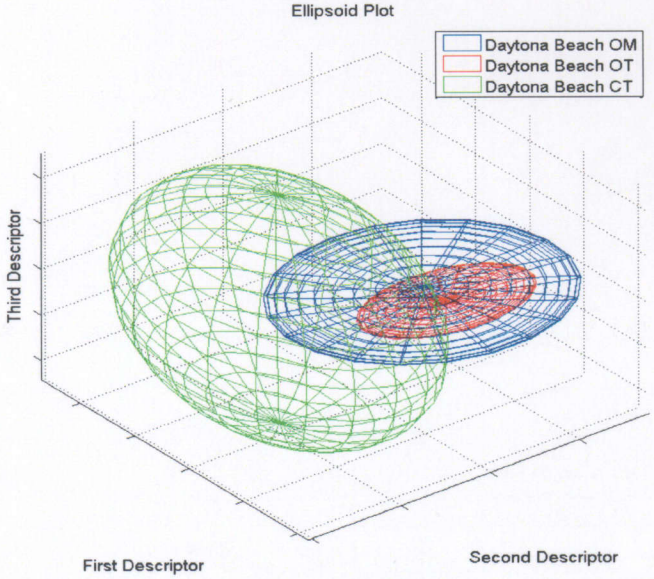

Figure 4-18: Alternate view of DB 5/16/2005 ellipsoid model illustrating the X-ray CT, OT, and OM descriptor variances.

The final synthesis reconstruction for the Daytona Beach particle mix is seen in Figure 4-19.

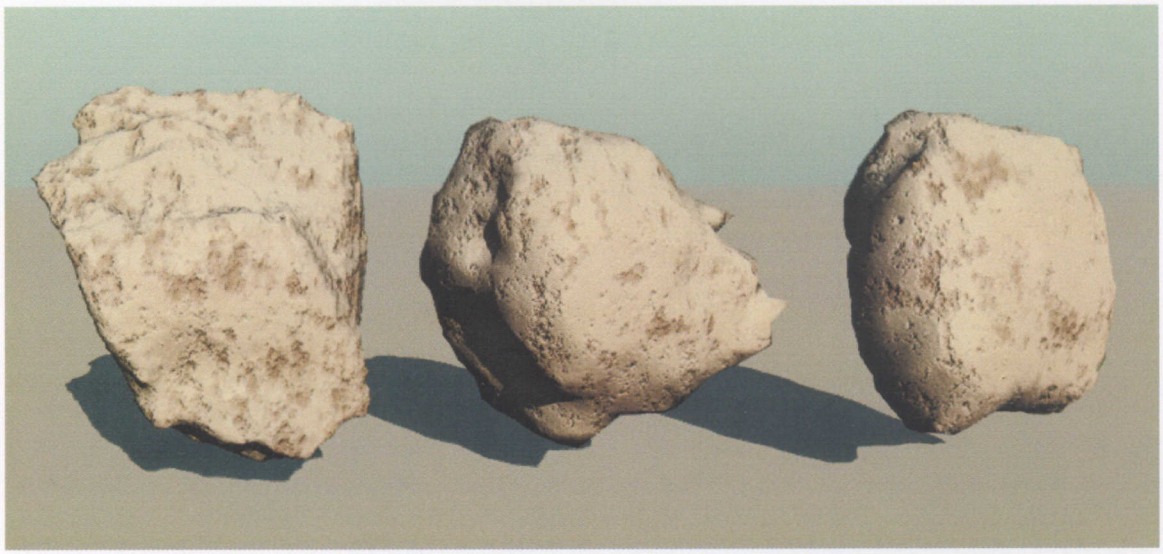

Figure 4-19: DB 7/13/2005- From left to right: X-ray CT, OT and synthesized OM reconstructions.

As with the previous reconstructions, Figures 4-20 and 4-21 show different views of the ellipsoid model corresponding to DB 7/13/2005.

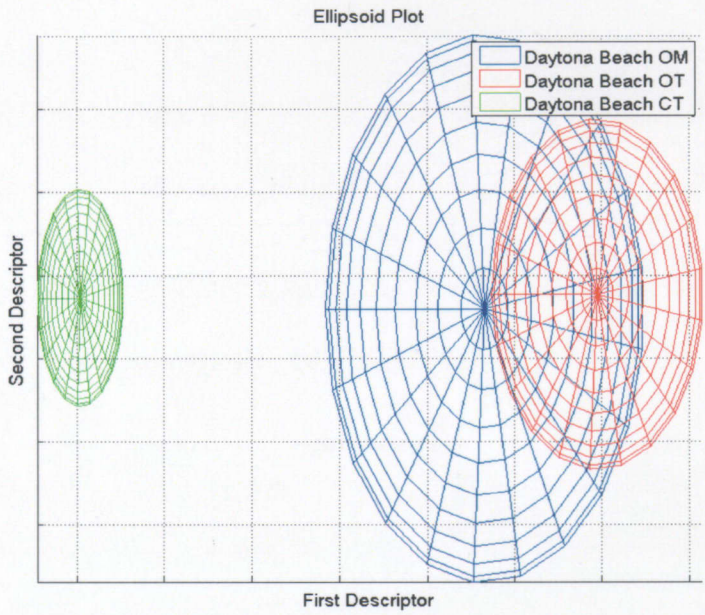

Figure 4-20: The DB 7/13/2005 ellipsoid model illustrating the X-ray CT, OT, and OM descriptor variances.

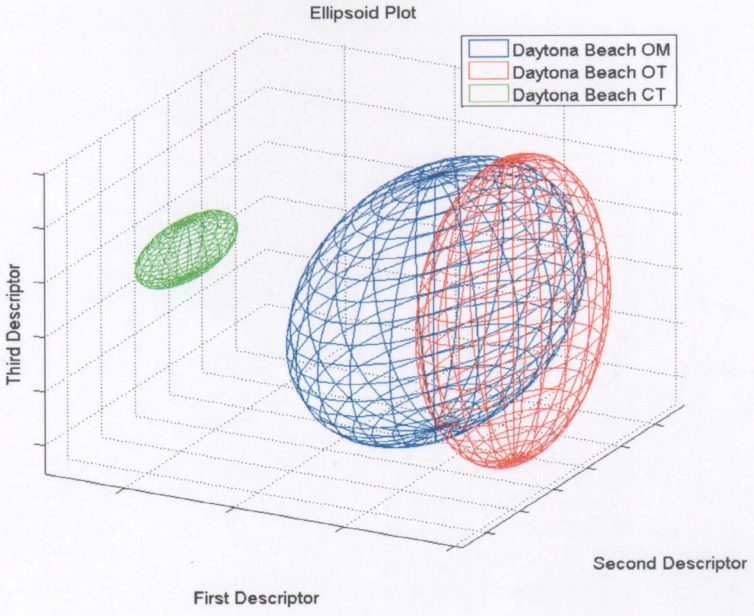

Figure 4-21: Alternate view of DB 7/13/2005 ellipsoid model illustrating the X-ray CT, OT, and OM descriptor variances.

4.5.2 Dry #1

The next mix that was tested with the new synthesis procedure was the Dry #1 mixture.

Figure 4-22 shows the DY1 5/3/2005 sand particle.

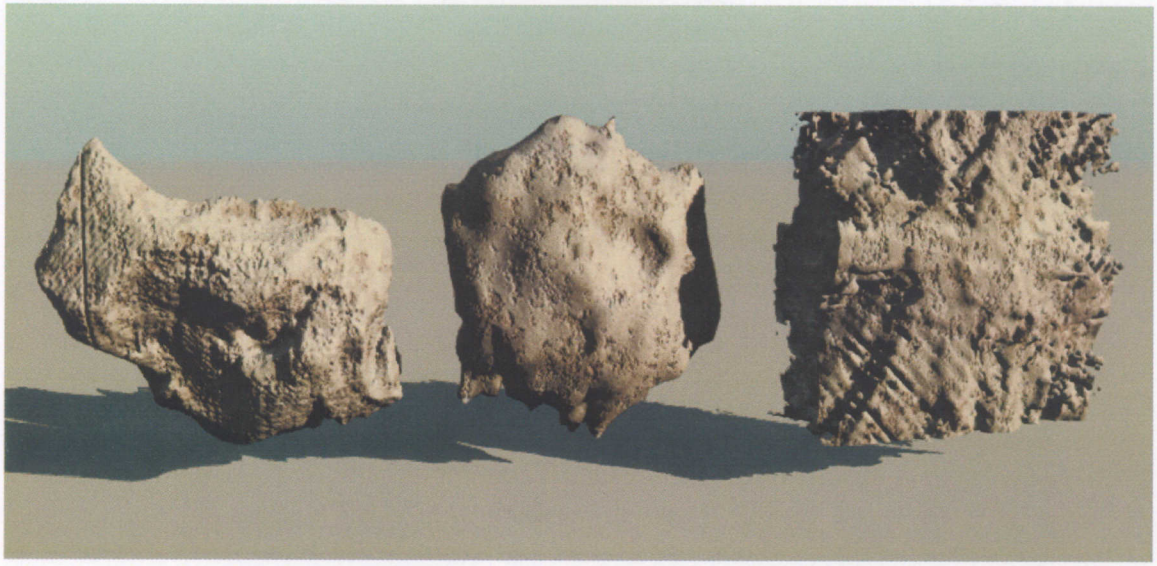

Figure 4-22: DY1 5/3/2005- From left to right: X-ray CT, OT and synthesized OM reconstructions.

Figure 4-22 shows the first failed reconstruction of the synthesized particle. The following Figures 4-23 and 4-24 show the ellipsoid model of Figure 4-22.

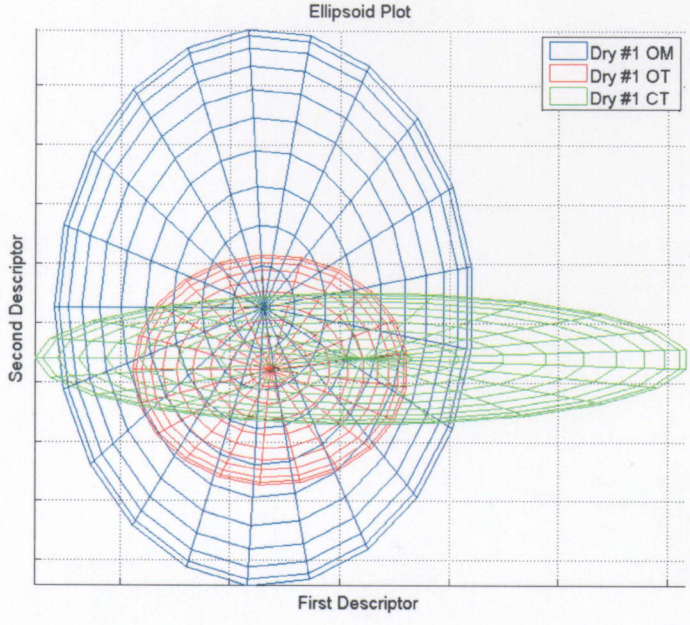

Figure 4-23: The DY1 5/3/2005 ellipsoid model illustrating the X-ray CT, OT, and OM descriptor variances.

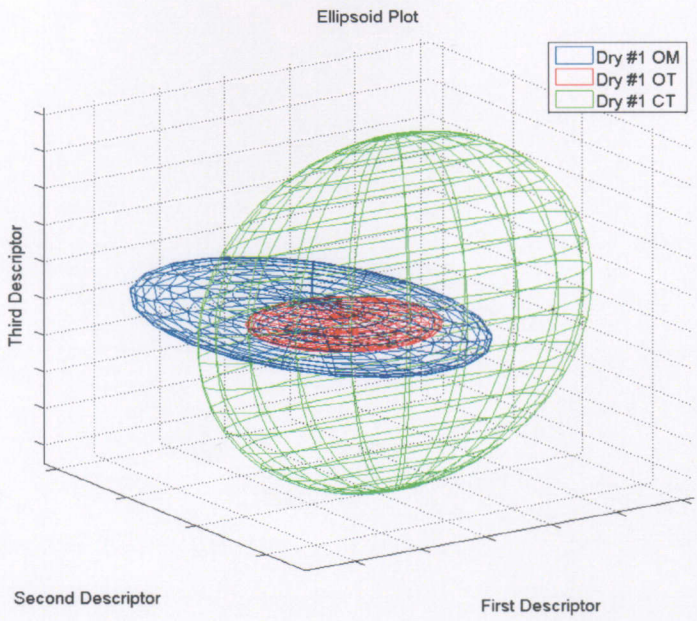

Figure 4-24: Alternate view of the DY1 5/3/2005 ellipsoid model illustrating the X-ray CT, OT, and OM descriptor variances.

Notice how in the above Figures 4-23,24 the ellipsoid model shows that the descriptor variances for the OM particle are not that far off from the X-ray and the OT system descriptors, yet the OM reconstruction has apparently failed. This will be discussed in detail in the next section. The next particle is DY1 6/27/2005.

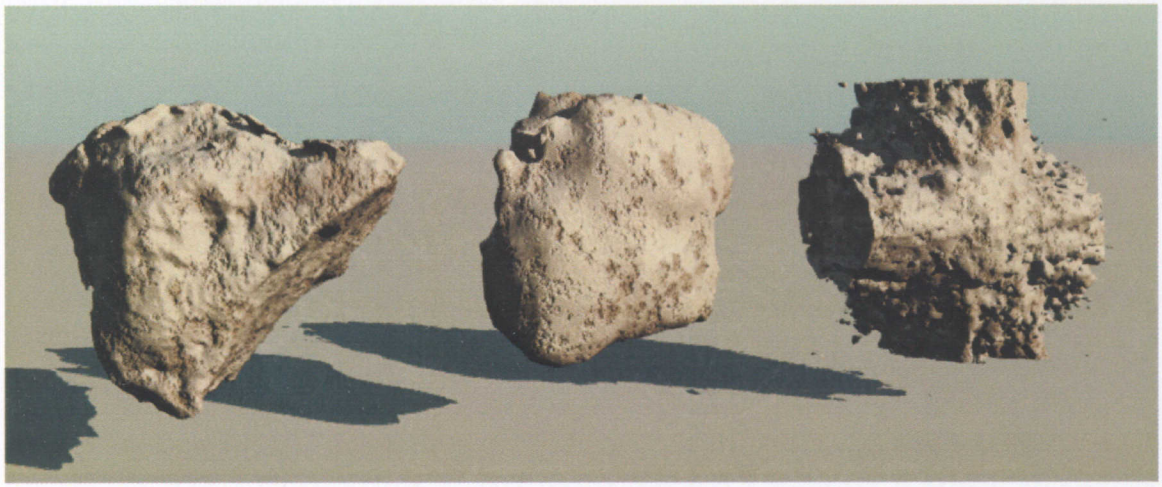

Figure 4-25: DY1 6/27/2005- From left to right: X-ray CT, OT and synthesized OM reconstructions.

Figures 4-26, 27 are the ellipsoid models of the DY1 6/27/2005 particle.

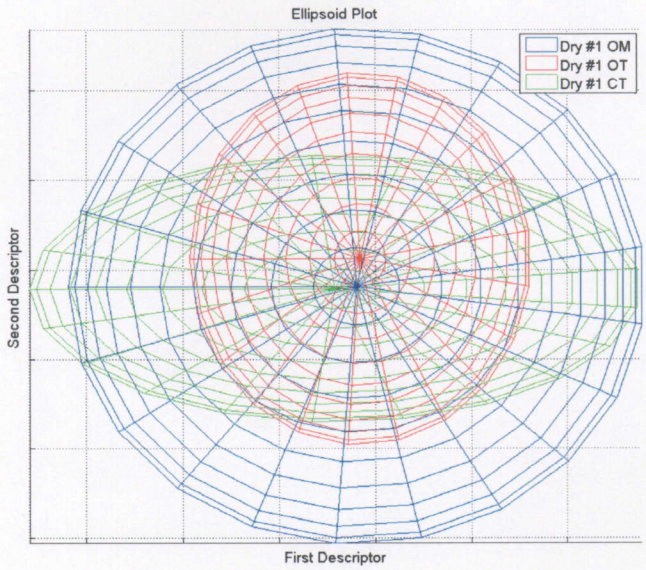

Figure 4-26: The DY1 5/3/2005 ellipsoid model illustrating the X-ray CT, OT, and OM descriptor variances.

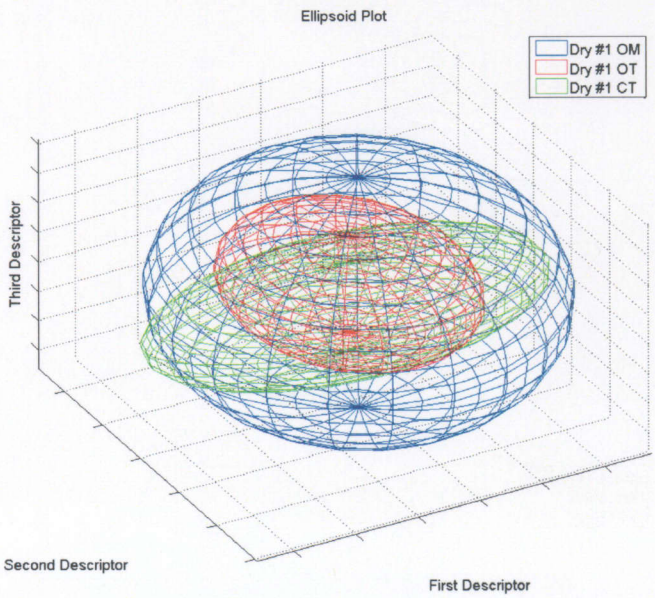

Figure 4-27: The alternate view of the DY1 5/3/2005 ellipsoid model illustrating the X-ray CT, OT, and OM descriptor variances.

The final particle in this mix that will be evaluated is the DY1 7/13/2005 particle, which can be seen in Figure 4-28.

Figure 4-28: DY1 7/13/2005- From left to right: X-ray CT, OT and synthesized OM reconstructions.

The following Figures 4-29, 30 are views of the DY1 7/13/2005 sand particle.

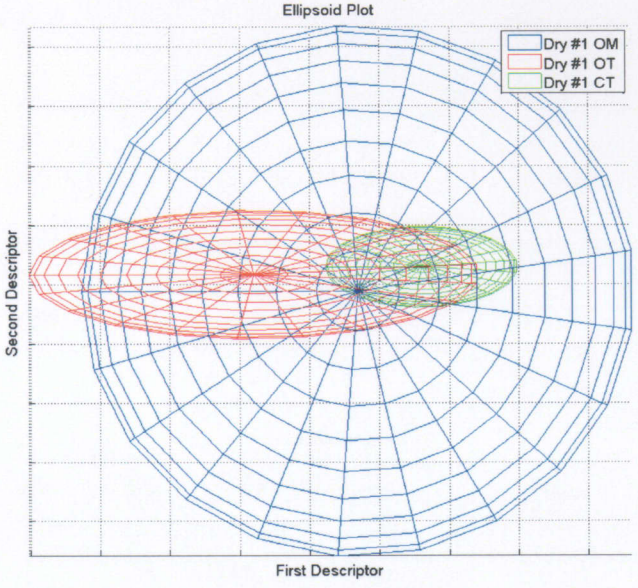

Figure 4-29: The DY1 7/13/2005 ellipsoid model illustrating the X-ray CT, OT, and OM descriptor variances.

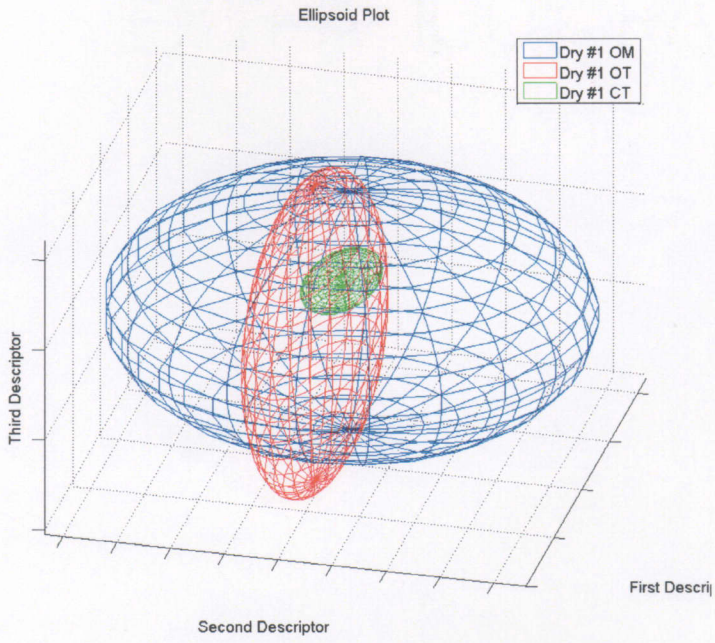

Figure 4-30: The alternate view of the DY1 7/13/2005 ellipsoid model illustrating the X-ray CT, OT, and OM descriptor variances.

4.5.3 Michigan Dune

The Michigan Dune aggregate mixture synthesis test consists of six individual particles. The forth particle exhibits a behavior unlike any of the other particles in this test scenario, and thusly prompts the work in section 4.6. The first particle MD 4/26/2005 can be seen in Figure 4-31.

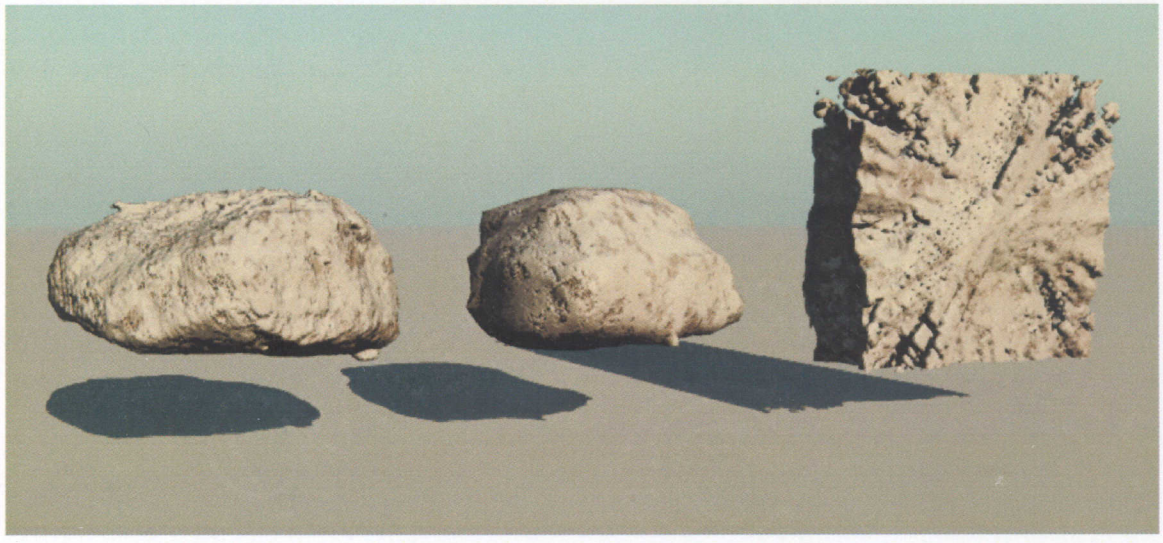

Figure 4-31: MD 4/26/2005- From left to right: X-ray CT, OT and synthesized OM reconstructions.

The resulting ellipsoid model can be seen in Figures 4-32, 33

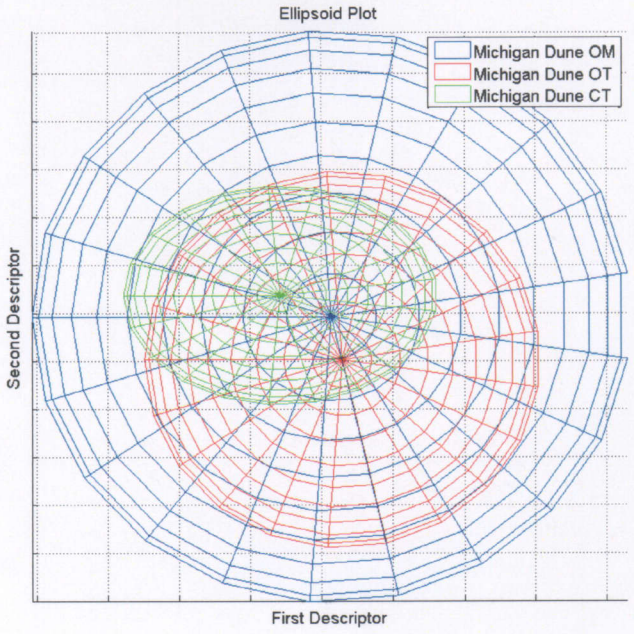

Figure 4-32: The MD 4/26/2005 ellipsoid model illustrating the X-ray CT, OT, and OM descriptor variances.

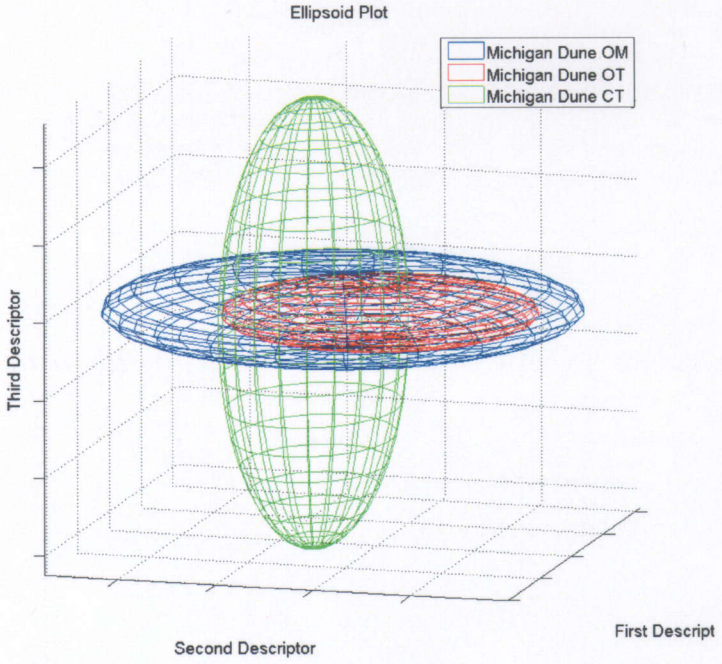

Figure 4-33: The alternative view of the MD 4/26/2005 ellipsoid model illustrating the X-ray CT, OT, and OM descriptor variances.

MD 5/3/2005 can be seen in Figure 4-44.

Figure 4-34: MD 5/3/2005- From left to right: X-ray CT, OT and synthesized OM reconstructions.

Figures 4-35, 36 are the alternative views of the ellipsoid model describing Figure 4-34.

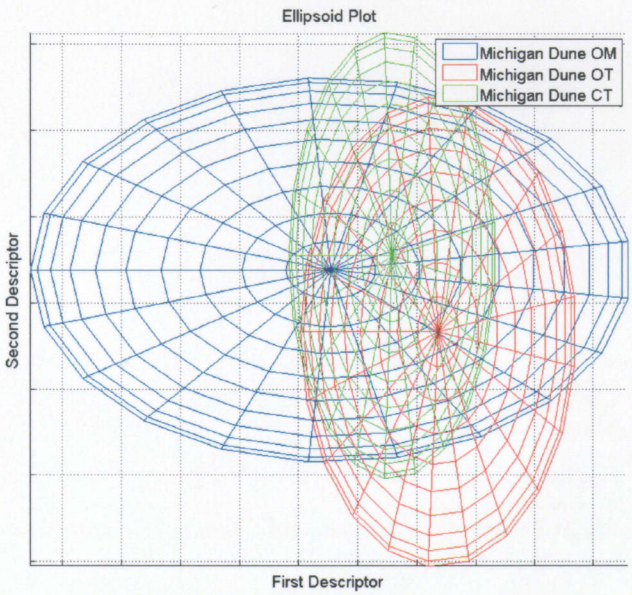

Figure 4-35: The MD 5/3/2005 ellipsoid model illustrating the X-ray CT, OT, and OM descriptor variances.

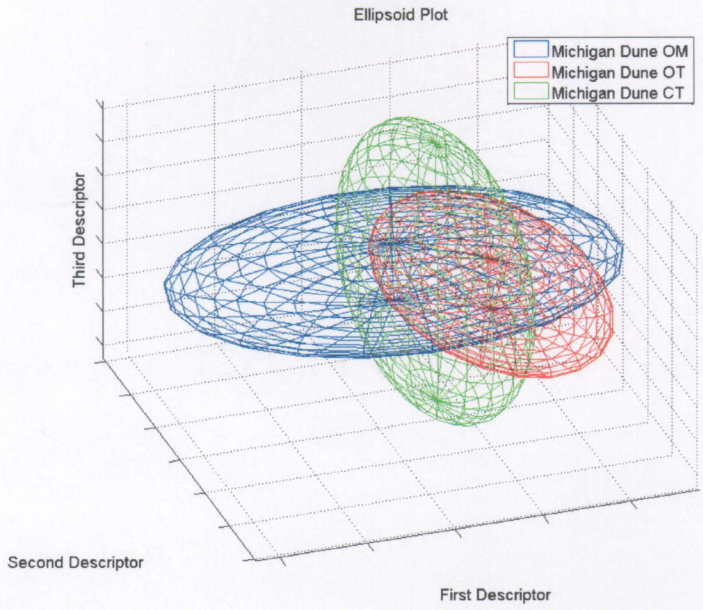

Figure 4-36: The alternative view of the MD 5/3/2005 ellipsoid model illustrating the X-ray CT, OT, and OM descriptor variances.

Figure 4-37 shows the MD 5/31/2005 sand particle.

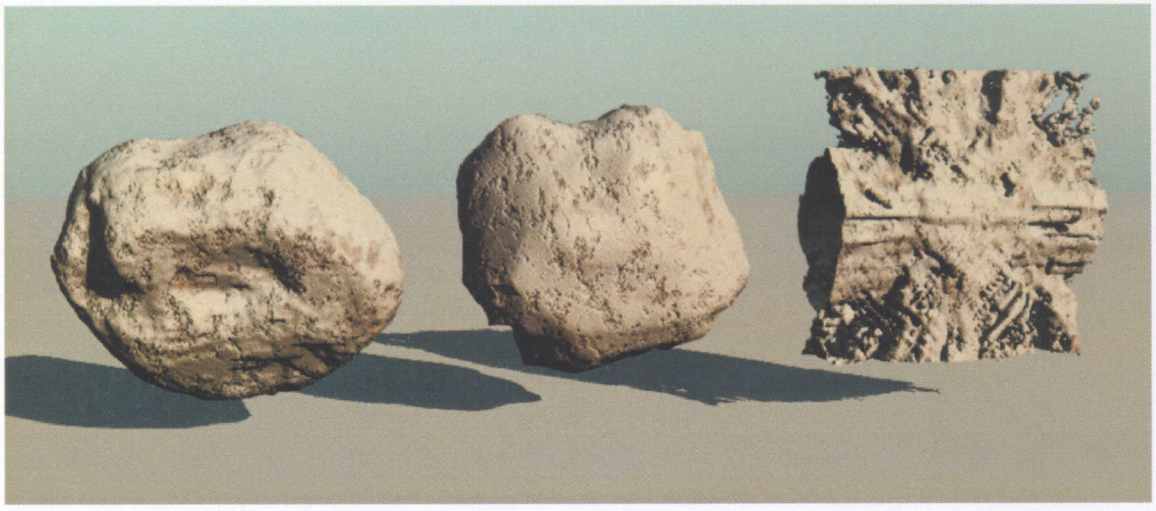

Figure 4-37: MD 5/31/2005- From left to right: X-ray CT, OT and synthesized OM reconstructions.

Figures 4-38, 39 are the alterative angles of the ellipsoid model.

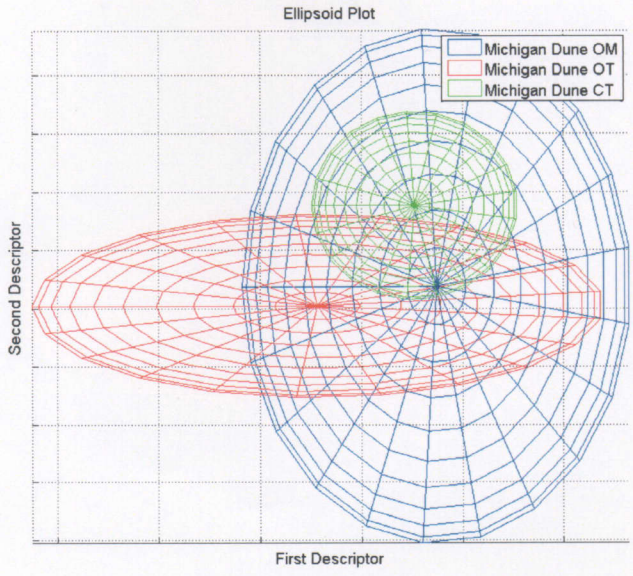

Figure 4-38: The MD 5/31/2005 ellipsoid model illustrating the X-ray CT, OT, and OM descriptor variances.

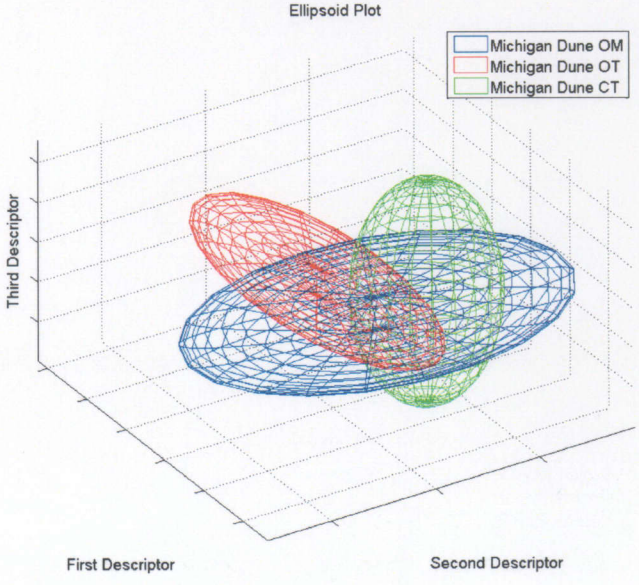

Figure 4-39: The alternative view of the MD 5/31/2005 ellipsoid model illustrating the X-ray CT, OT, and OM descriptor variances.

The forth particle to be analyzed is the MD 7/6/2005 which to this point stands out because it is the only MD particle to have a valid reconstruction, as mentioned

previously this resulted prompted the future work in section 4.6 of this thesis and is seen in Figure 4-40

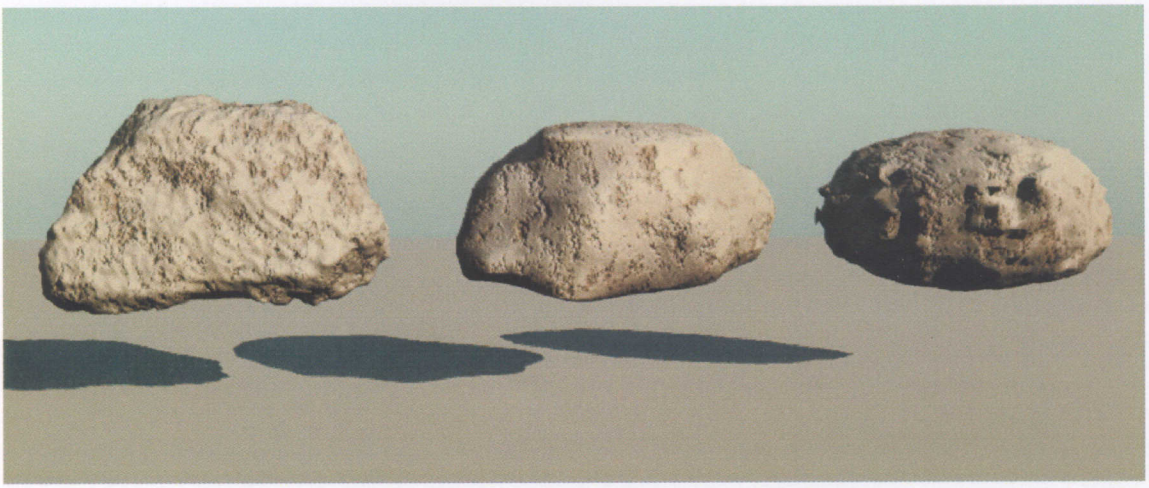

Figure 4-40: MD 7/6/2005- From left to right: X-ray CT, OT and synthesized OM reconstructions.

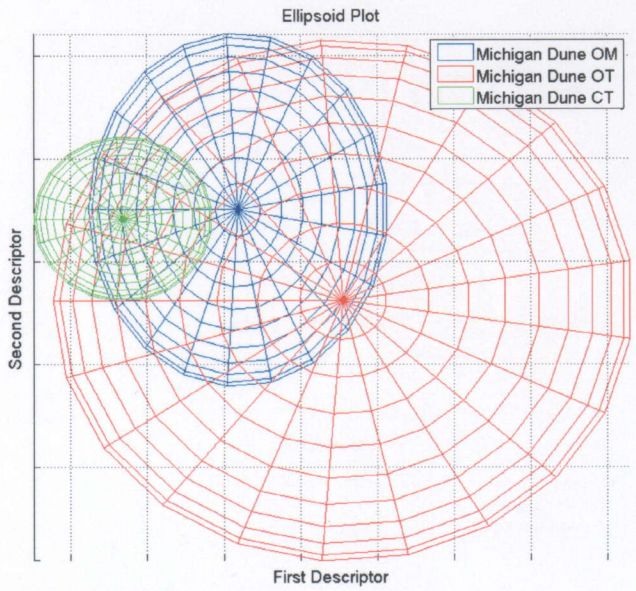

Figure 4-41: The MD 7/6/2005 ellipsoid model illustrating the X-ray CT, OT, and OM descriptor variances.

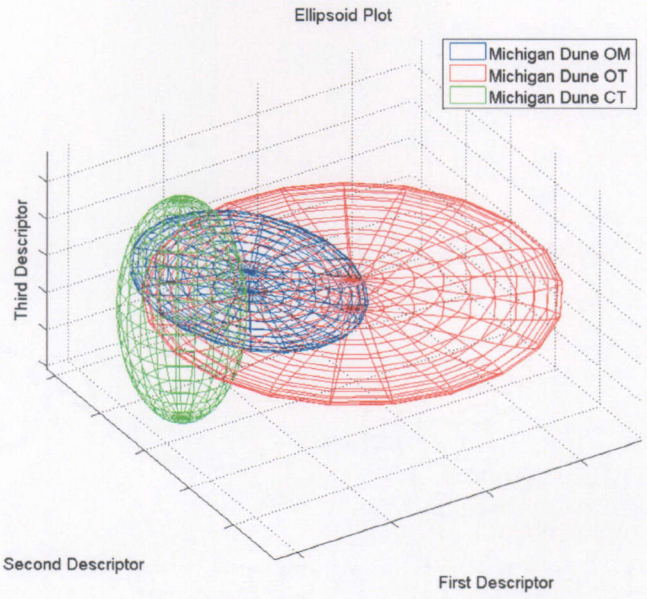

Figure 4-42: The alternative view of the MD 7/6/2005 ellipsoid model illustrating the X-ray CT, OT, and OM descriptor variances.

MD 7/11/2005 is seen in Figure 4-43.

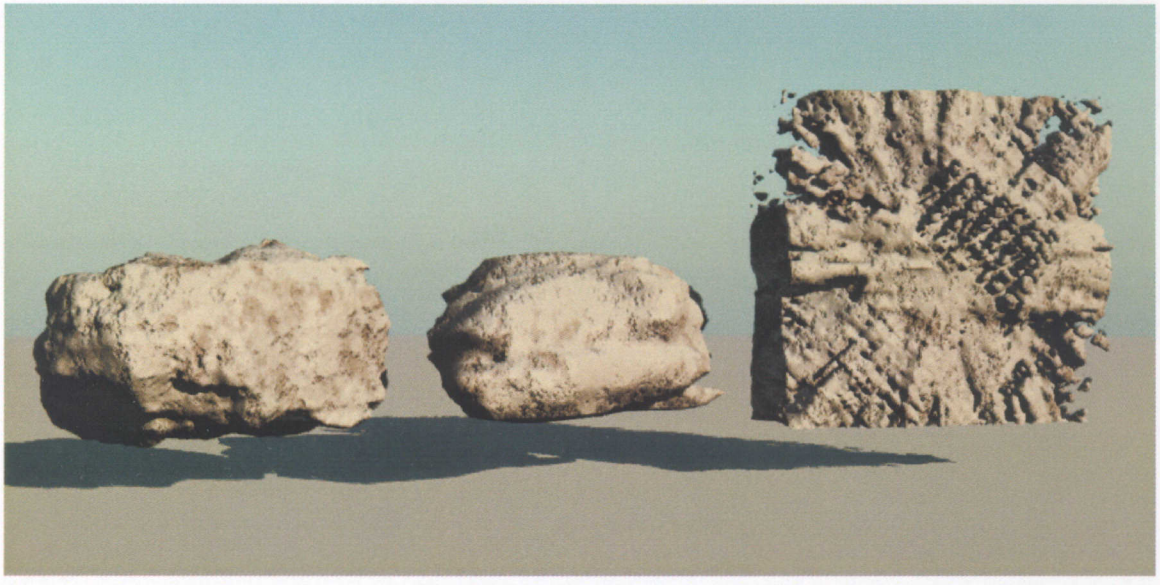

Figure 4-43: MD 7/11/2005- From left to right: X-ray CT, OT and synthesized OM reconstructions.

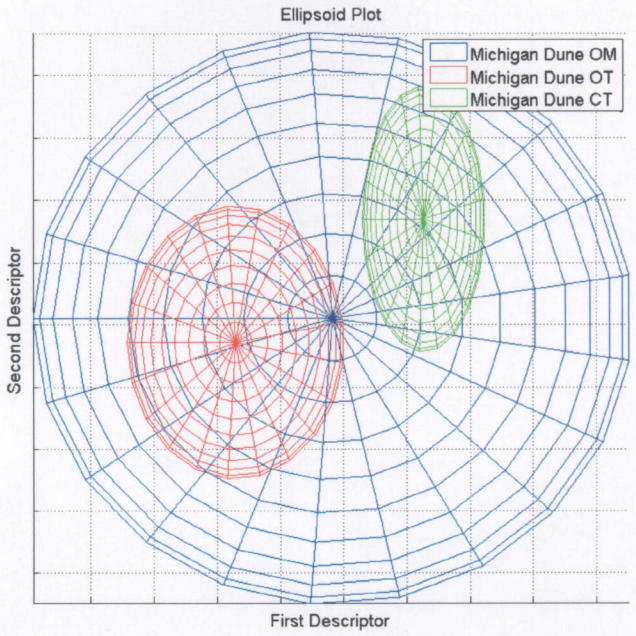

Figure 4-44: The MD 7/11/2005 ellipsoid model illustrating the X-ray CT, OT, and OM descriptor variances.

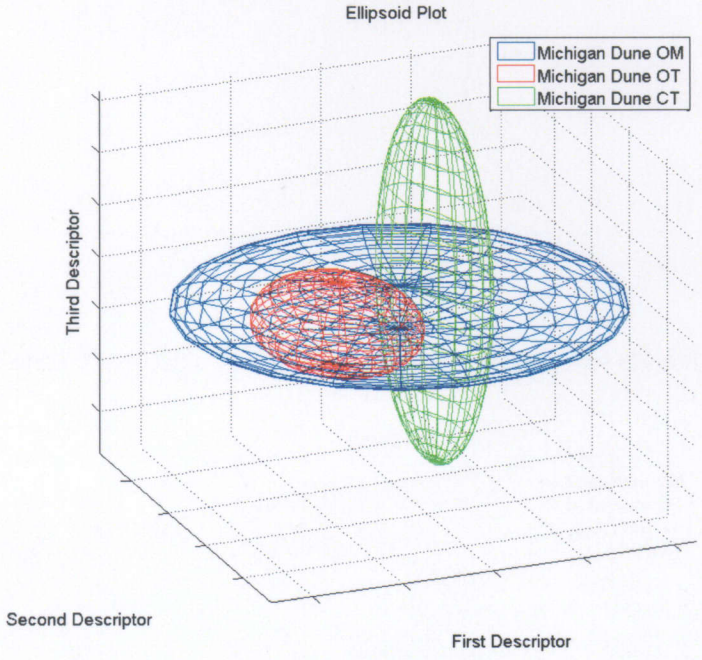

Figure 4-45: The alternative view of the MD 7/11/2005 ellipsoid model illustrating the X-ray CT, OT, and OM descriptor variances.

The final particle to be addressed in the Michigan dune sub chapter is MD 718/2005 seen in Figure 4-46.

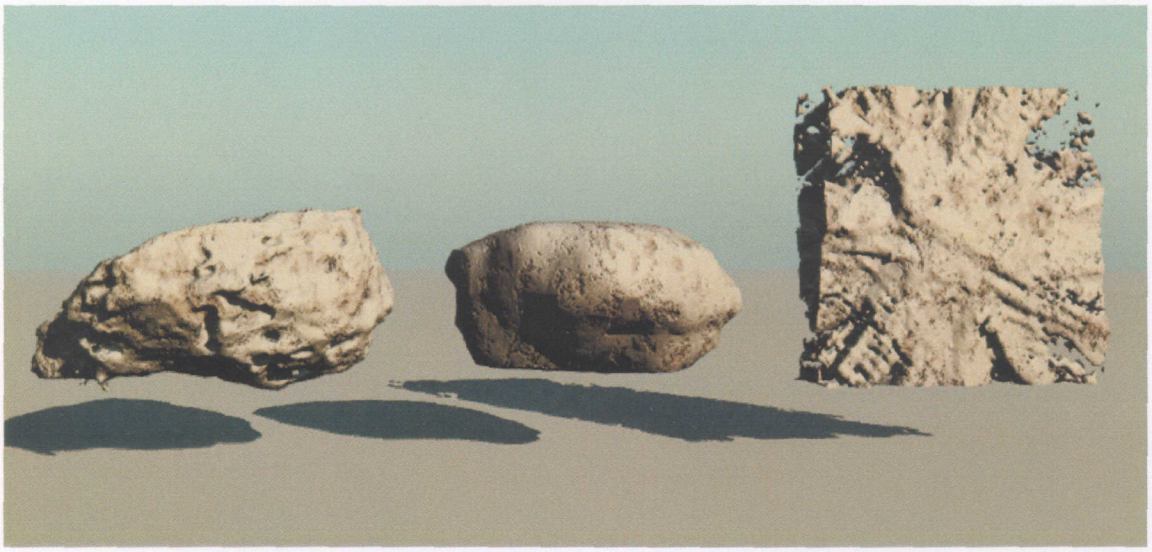

Figure 4-46: MD 7/18/2005- From left to right: X-ray CT, OT and synthesized OM reconstructions.

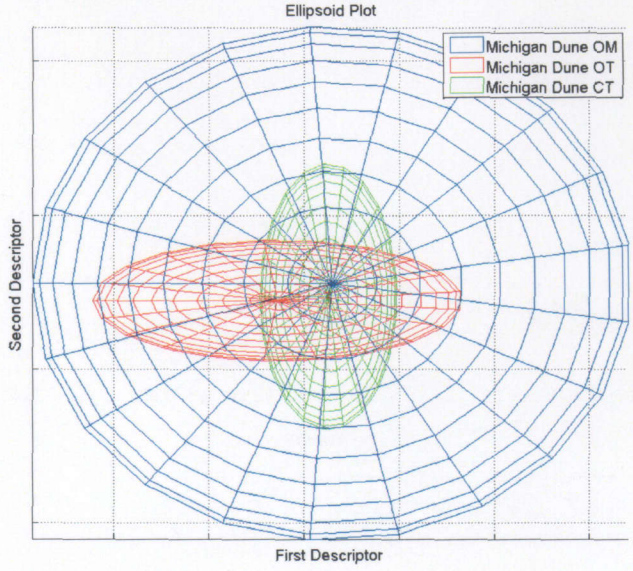

Figure 4-47: The MD 7/18/2005 ellipsoid model illustrating the X-ray CT, OT, and OM descriptor variances.

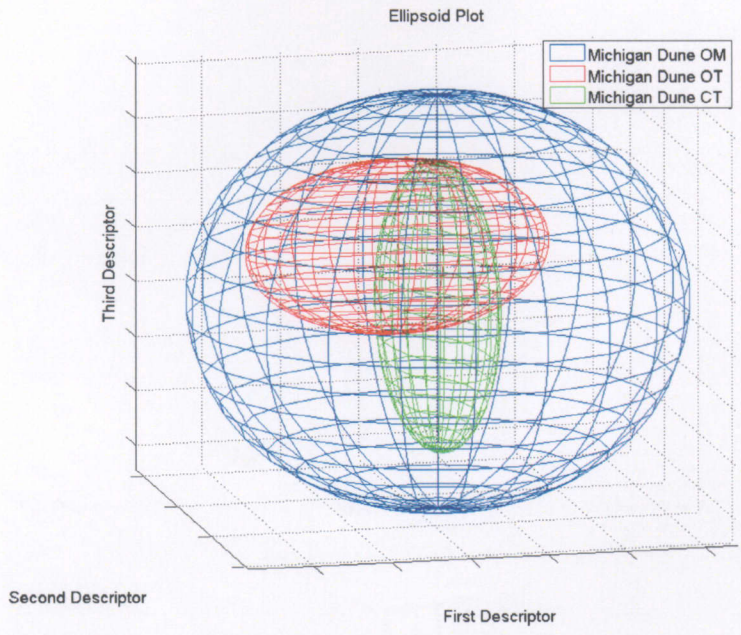

Figure 4-48: The alternative view of the MD 7/18/2005 ellipsoid model illustrating the X-ray CT, OT, and OM descriptor variances.

4.5.4 Standard Melt

The final sand mixture that was tested with the synthesis procedure is the Standard Melt aggregate mixture. Figure 4-49 is of the SM 5/12/2005.

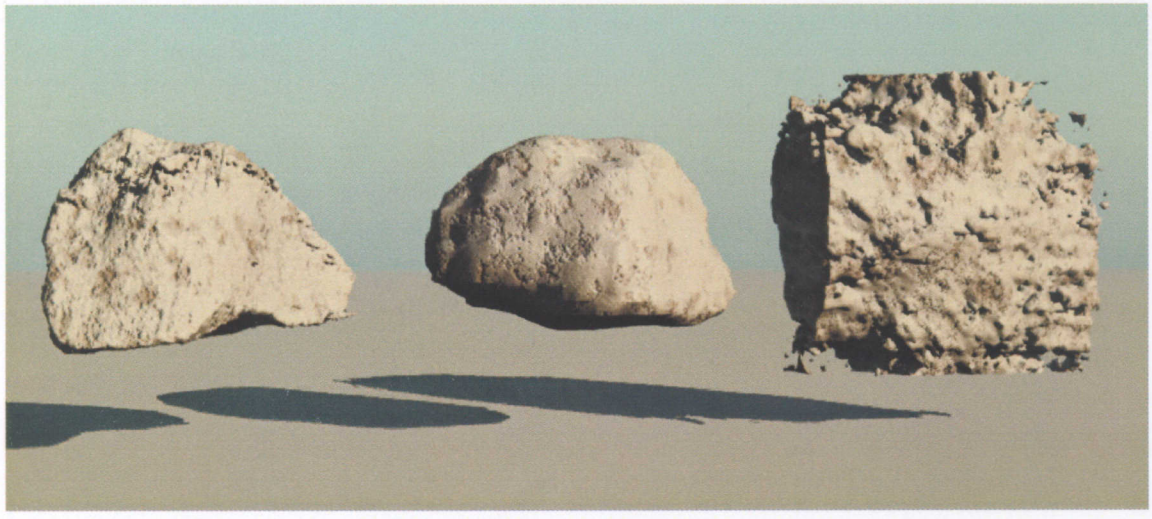

Figure 4-49: SM 5/12/2005- From left to right: X-ray CT, OT and synthesized OM reconstructions.

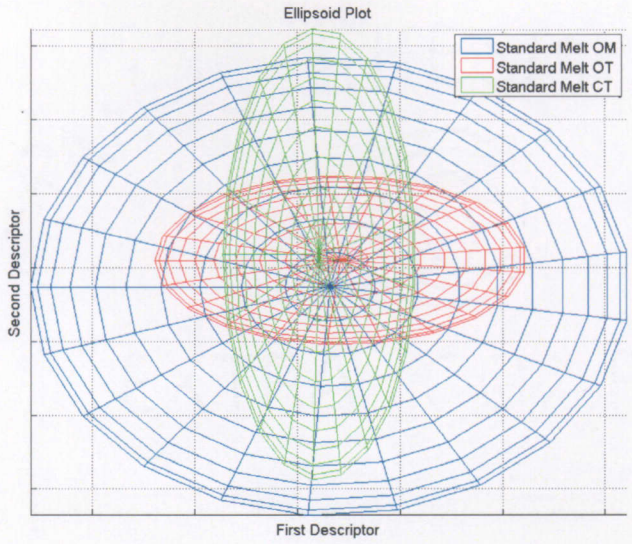

Figure 4-50: The SM 5/12/2005 ellipsoid model illustrating the X-ray CT, OT, and OM descriptor variances.

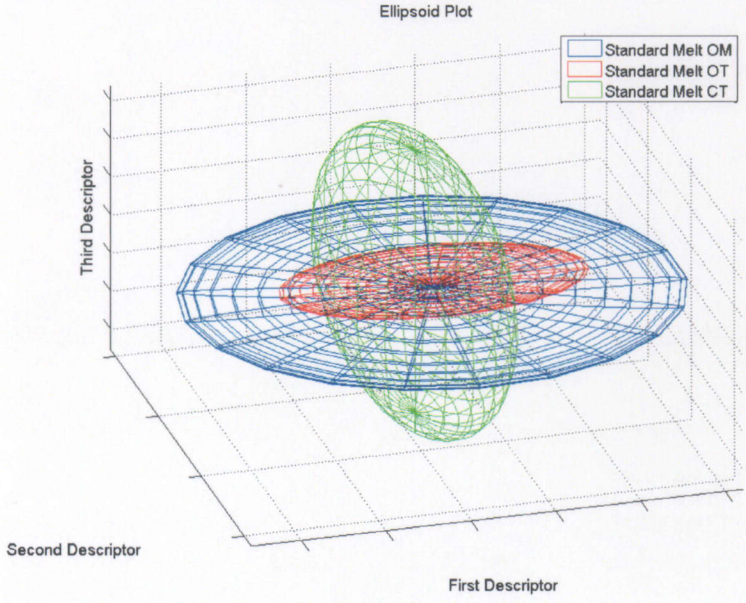

Figure 4-51: The alternative view of the SM 5/12/2005 ellipsoid model illustrating the X-ray CT, OT, and OM descriptor variances.

The next particle is SM 7/6/2005 and is seen in Figure 4-52.

Figure 4-52: SM 7/6/2005- From left to right: X-ray CT, OT and synthesized OM reconstructions.

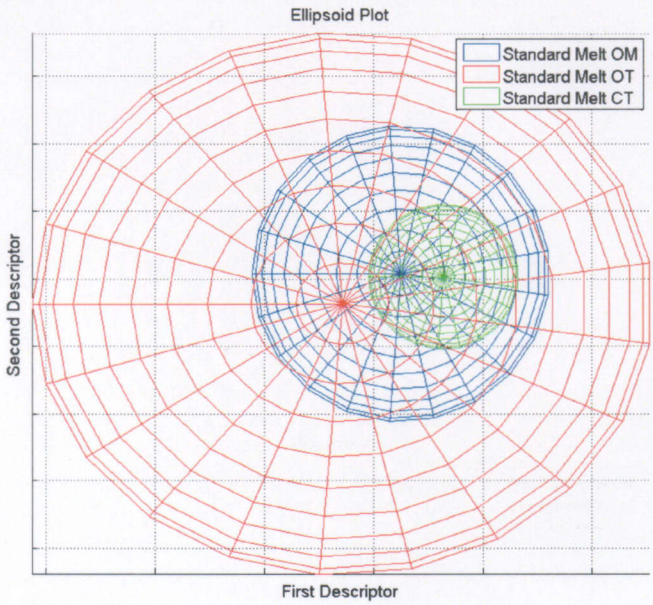

Figure 4-53: The SM 7/6/2005 ellipsoid model illustrating the X-ray CT, OT, and OM descriptor variances.

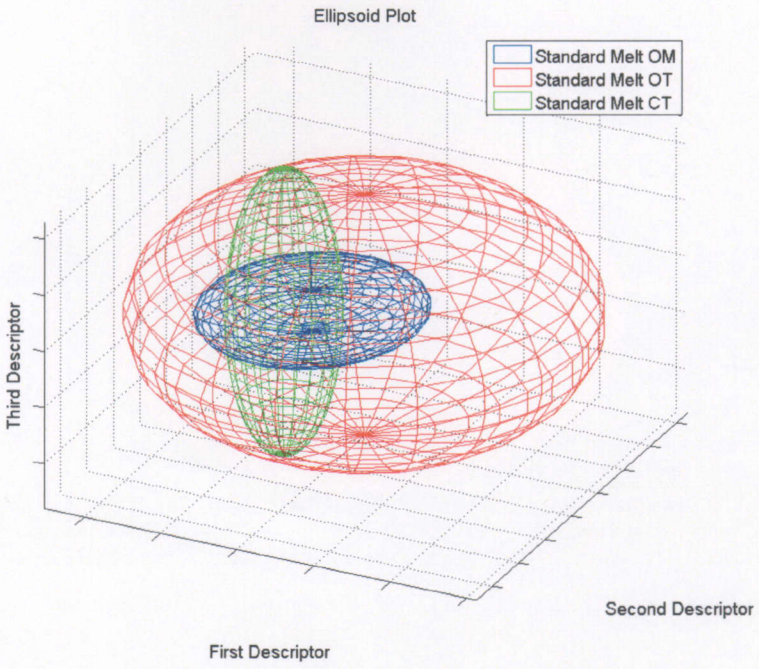

Figure 4-54: The alternative view of the SM 7/6/2005 ellipsoid model illustrating the X-ray CT, OT, and OM descriptor variances.

Figure 4-55 illustrates the SM 8/18/2005 sand particle.

Figure 4-55: SM 8/18/2005- From left to right: X-ray CT, OT and synthesized OM reconstructions.

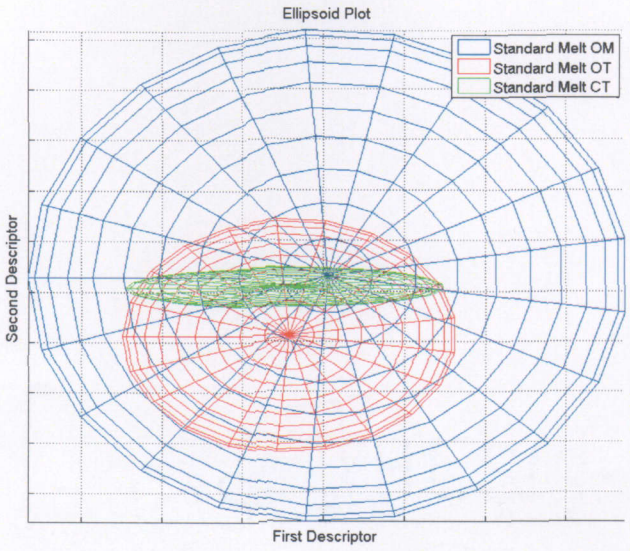

Figure 4-56: The SM 8/18/2005 ellipsoid model illustrating the X-ray CT, OT, and OM descriptor variances.

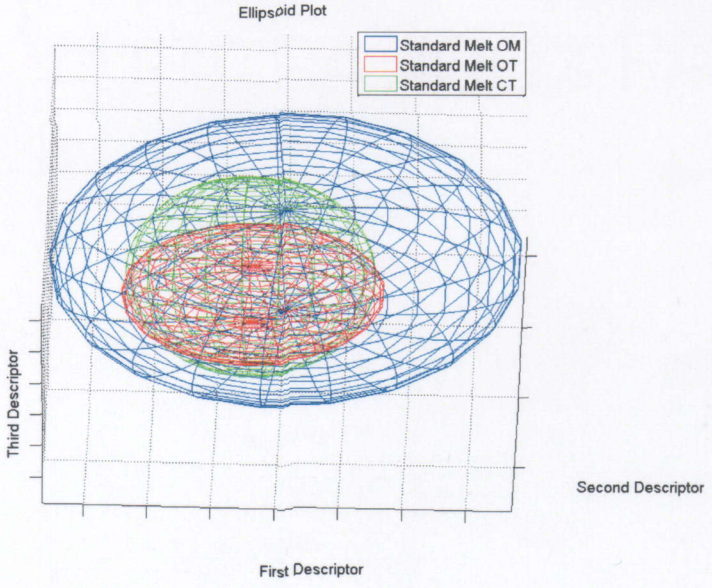

Figure 4-57: The alternative view of the SM 8/18/2005 ellipsoid model illustrating the X-ray CT, OT, and OM descriptor variances.

The final image tested in the Standard melt aggregate mixture is SM 8/22/2005 and is seen in Figure 4-58.

Figure 4-58: SM 8/22/2005- From left to right: X-ray CT, OT and synthesized OM reconstructions.

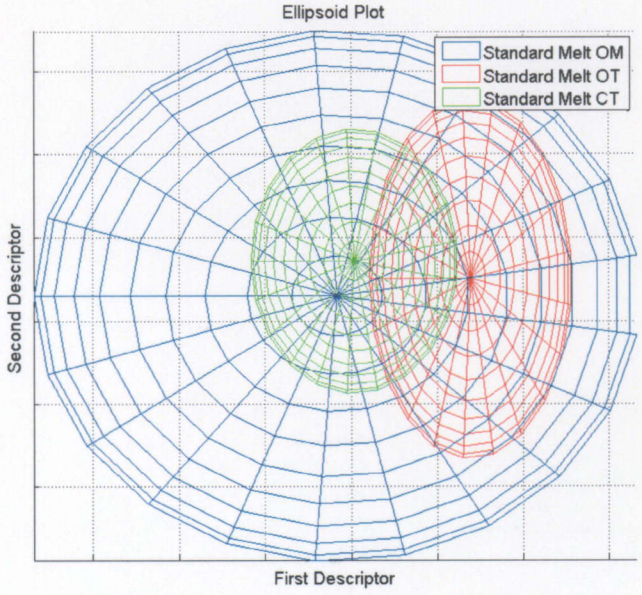

Figure 4-59: The SM 8/22/2005 ellipsoid model illustrating the X-ray CT, OT, and OM descriptor variances.

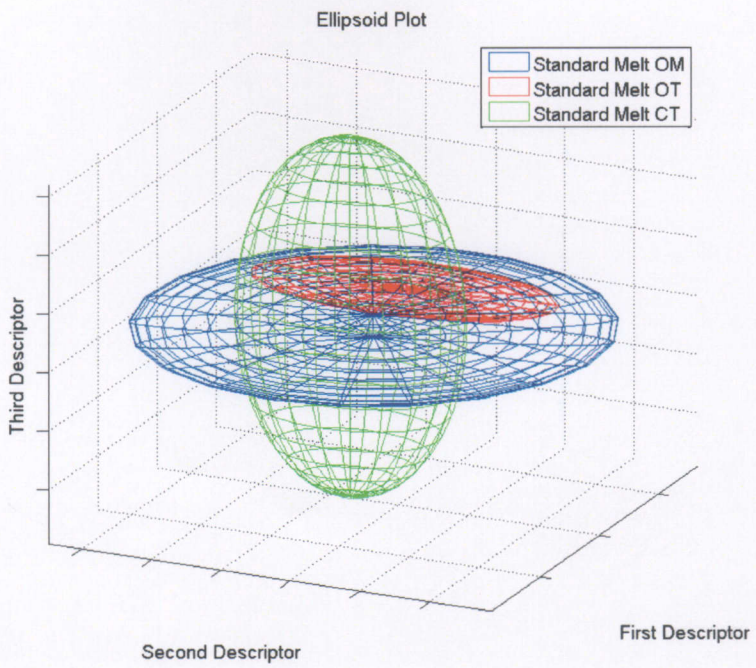

Figure 4-60: The alternative view of the SM 8/22/2005 ellipsoid model illustrating the X-ray CT, OT, and OM descriptor variances.

4.6 Validation tests

This set of testing looks at the feasibility of using the Fourier descriptors to match OM particle projections to that of OT projections specific to a single particle. The methodology is that previous work to synthesize models based on randomly selecting OM images proved to have significant failures across all the different sand mixtures. The thought was that the random selection was picking outliers that were not indicative of the overall shape characteristics of the mixture. By using the Fourier descriptors we are able to isolate the boundary of the OT projection and match it to the best fit OM projection. Since the OT method using ART is successful for generating particles, it was assumed that the images of the OT particles could be used to find the best correlated match to the OM images which then would yield a set of OM images that would reconstruct with the

success of the OT dataset. Michigan Dune was the anomaly such that every group either reconstructed every particle or none and in the Michigan Dune set there was only one complete reconstruction. The synthesis verification came from a need to investigate whether the properties of the Fourier transform would not be advantageous in this experiment, namely scale and rotation invariance. The Fourier transform is proved to be scale and rotation independent, meaning that the orientation of the boundary, the starting point, or the overall size has no effect on the generated descriptors which would leave images in essence that have a similar boundary as the OT image, but may be large in size compared to the other images in the dataset. Figure 4-61 shows a set of OT images from a single particle and the selected OM images to be used in synthesizing a 3-D model.

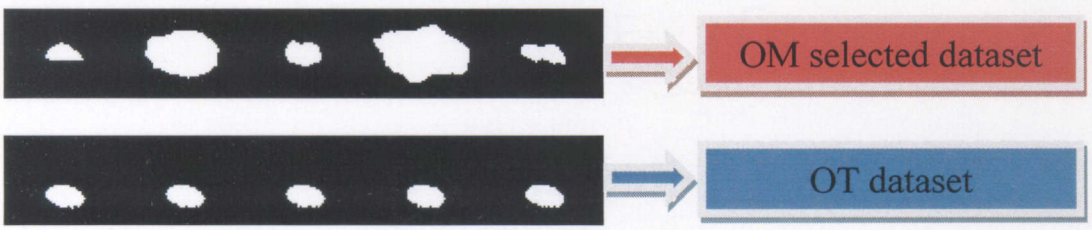

Figure 4-61: Illustrates the difference in sizes of the selected OM projections.

The large difference in size between the projections causes the back projection of the cross-section to fail where projection angles will no longer contain information. Figure 4-62 visually illustrates the problem.

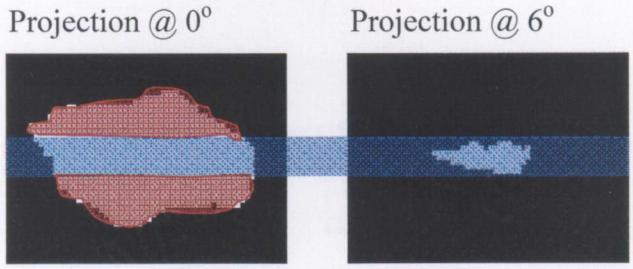

Figure 4-62: Red- illustrates the lost information when calculating the cross section; Blue- shows the retained information

As can be seen in Figure 4-62, the synthesis process is done by stacking the cross sectional layers. In this case the first projection has information at locations that are non-existent at the next projection angle, which ultimately is the case for many of the images.

To test whether the ART can handle situations where the scale and rotation of the boundaries are significantly different between projection angles, Michigan Dune MD 7/6/2005 has been chosen since its OM reconstruction was the only one for that mix to reconstruct and SM 7/6/2005 will be chosen since its OM reconstruction failed. The test will be conducted using the OT projections since that the OT reconstructions for both cases were successful. By altering the images to simulate large scale and rotation variances, we will be able to see if the ART algorithm can still successfully reconstruct the models, and whether the models are significantly different from the unaltered OT models. Three different tests will be performed on the two sand particles; 1) the boundaries of the OT particles will be individually randomly re-scaled larger and smaller than the originals, 2) the boundaries will be individually randomly rotated to simulate conditions found in the OM dataset, 3) and finally the boundaries will be individually randomly rescaled and rotated.

4.6.1 Boundary re-scaling

Figure 4-63 shows the original and the modified OT images for the two particles.

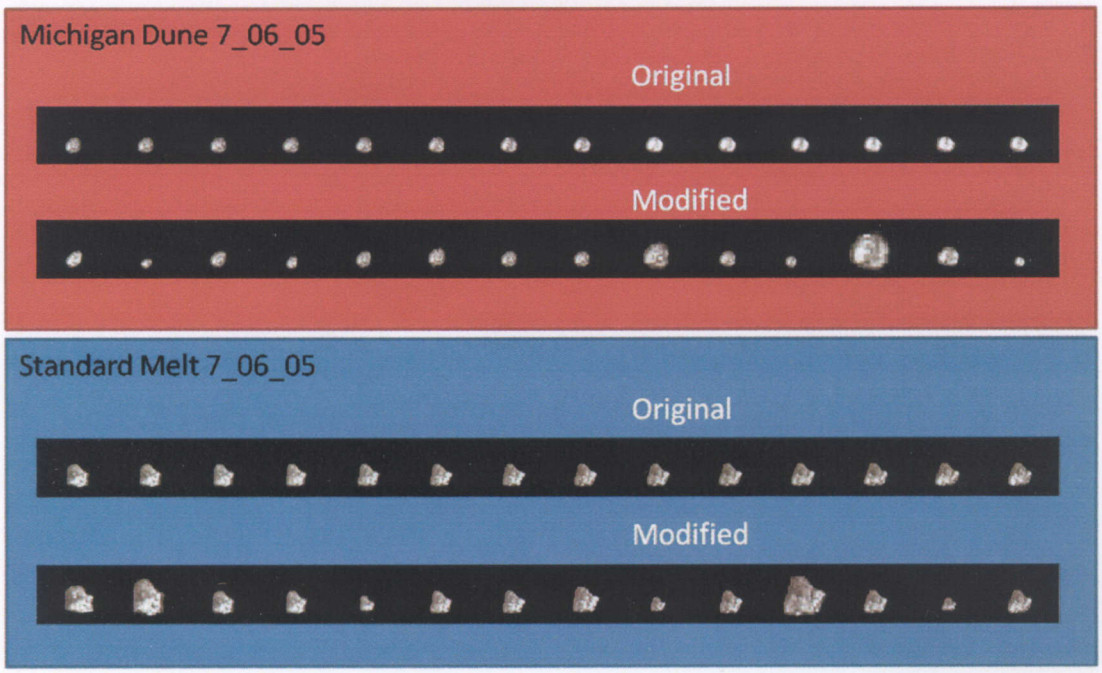

Figure 4-63: Original versus the modified images for the rescale test.

Figure 4-64 shows the results of the rescaling on the MD 7/6/2005.

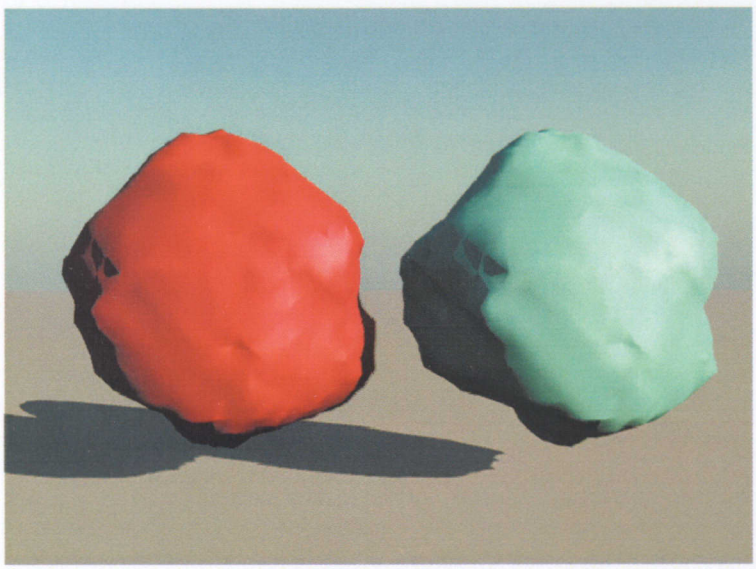

Figure 4-64: MD 7/6/2005 Red- unaltered original model, light blue- rescaled dataset.

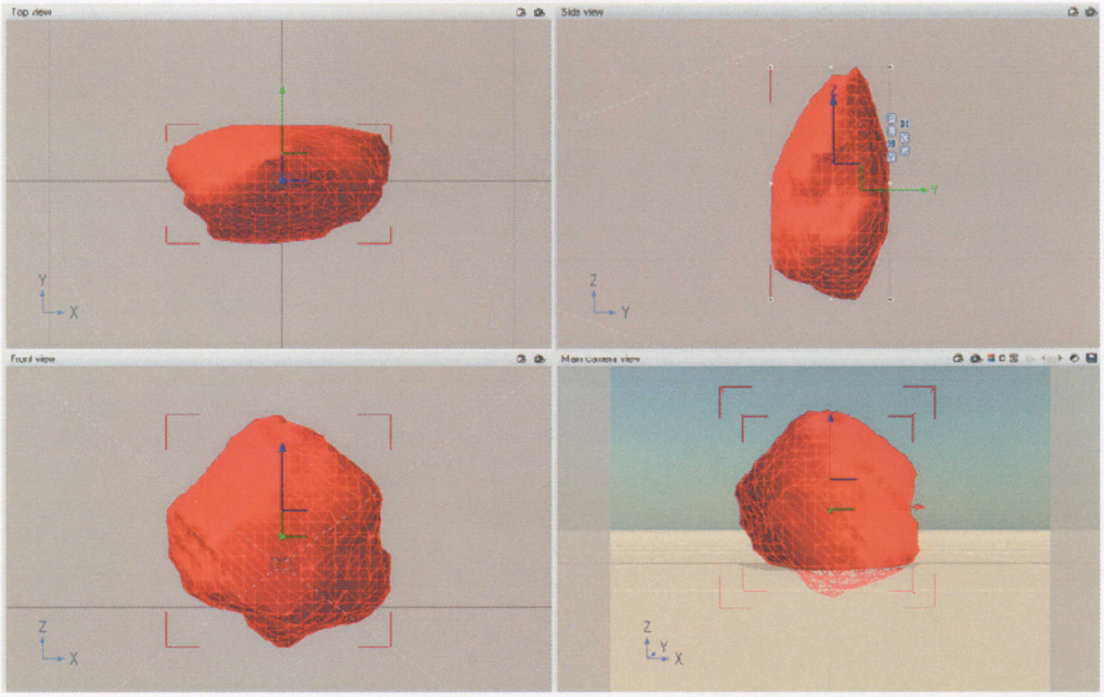

Figure 4-65: Difference mapping of the two models, notice how only red is seen showing that the original model and the modified model have near zero difference.

The Michigan Dune sand particle contained no apparent difference after rescaling the particles. Figure 4-66 shows the results on rescaling the SM 7/6/2005.

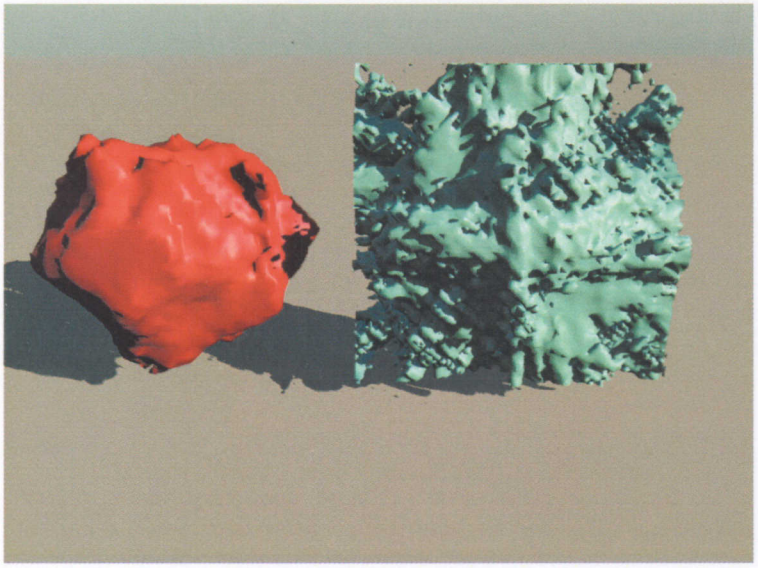

Figure 4-66: SM 7/6/2005 Red- unaltered original model, light blue- rescaled dataset.

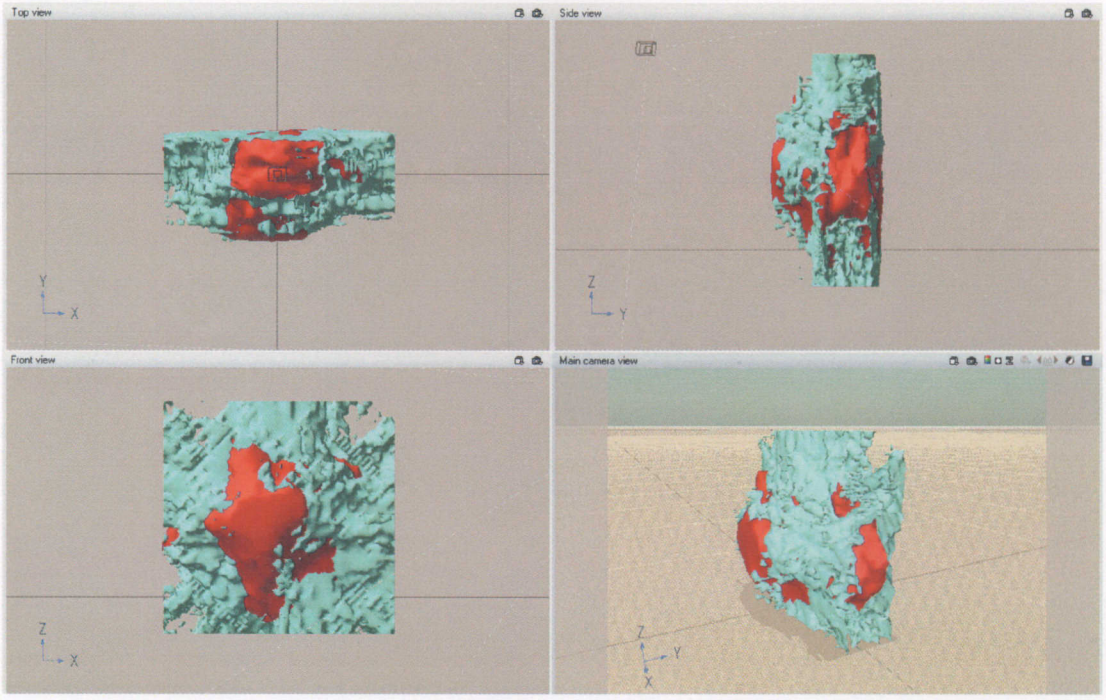

Figure 4-67: Difference mapping of the two models.

The Standard Melt particles' reconstruction fails when rescaling is done to the original OT data set, unlike what happened on the Michigan Dune sand particle. The interesting effect of the SM particle is that the original object appears as if it can be contained inside the failed reconstruction which will be explained in detail in section 4.7 discussion of results.

4.6.2 Boundary rotation

The next test that was preformed was rotating the objects boundary randomly and re-performing the reconstruction. A preview of the image dataset used can be seen in Figure 4-68.

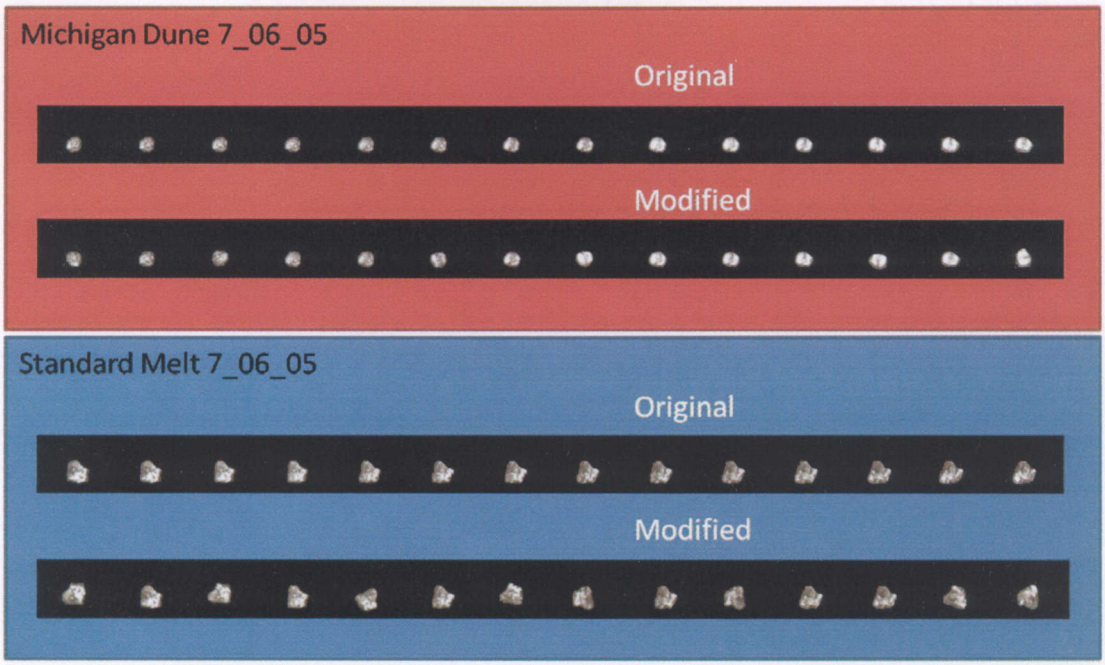

Figure 4-68: Original versus the modified images for the rotation test.

Figure 4-69 shows the results of random rotation on the MD 7/6/2005.

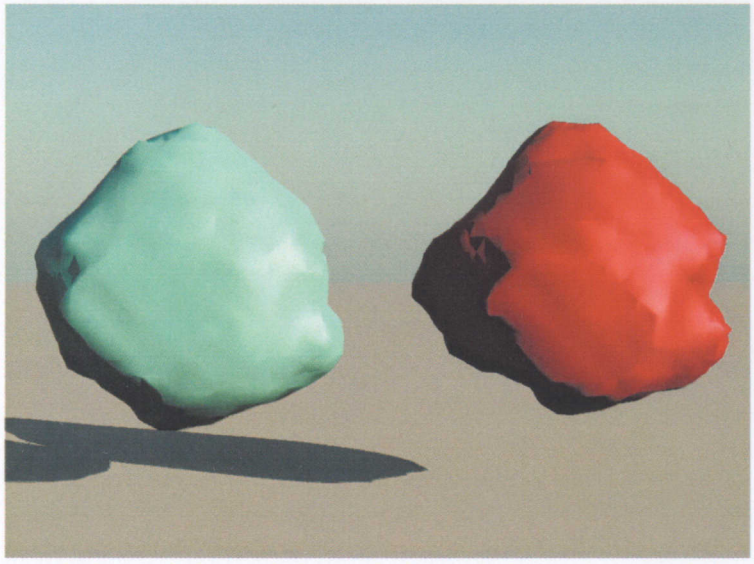

Figure 4-69: MD 7/6/2005 Red- unaltered original model, light blue- rotated boundary dataset.

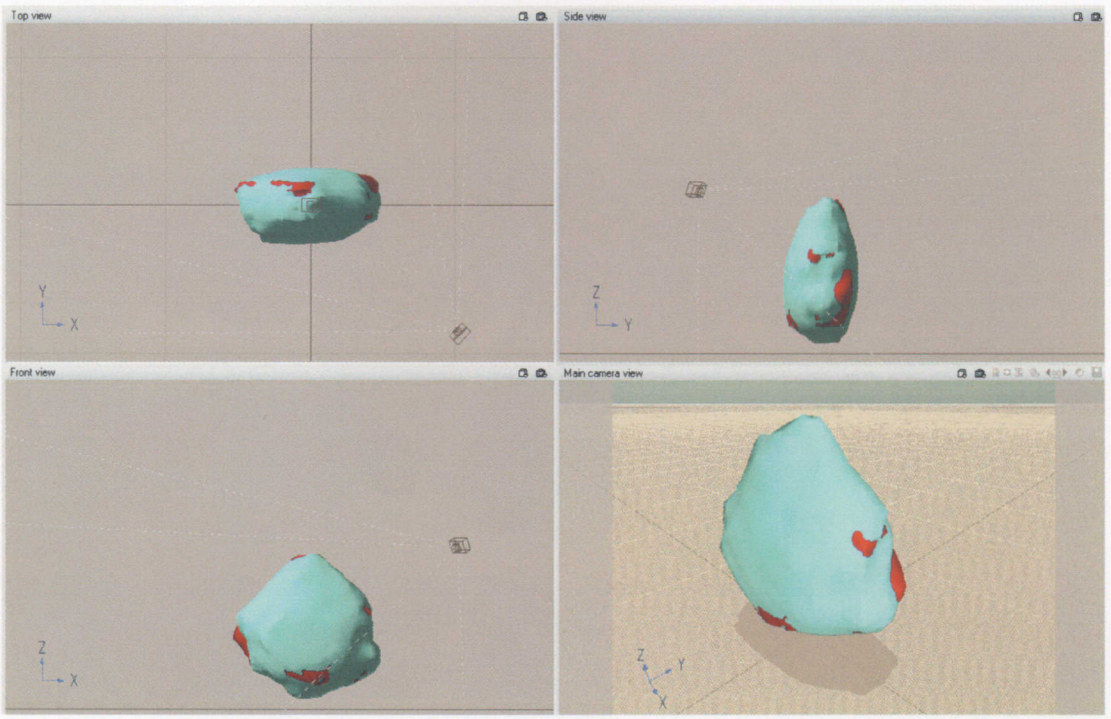

Figure 4-70: Difference mapping of the two models.

This time the Michigan Dune particle shows a higher level of difference than in the previous test, showing that rotation has a larger effect on the reconstruction than does the scale of the boundary. The test results for SM 7/6/2005 are seen in Figure 4-71.

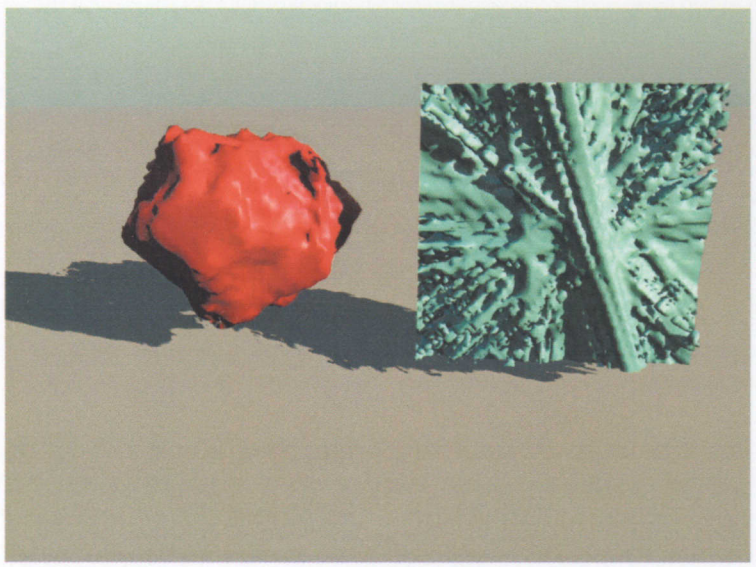

Figure 4-71: SM 7/6/2005 Red- unaltered original model, light blue- rotated boundary dataset.

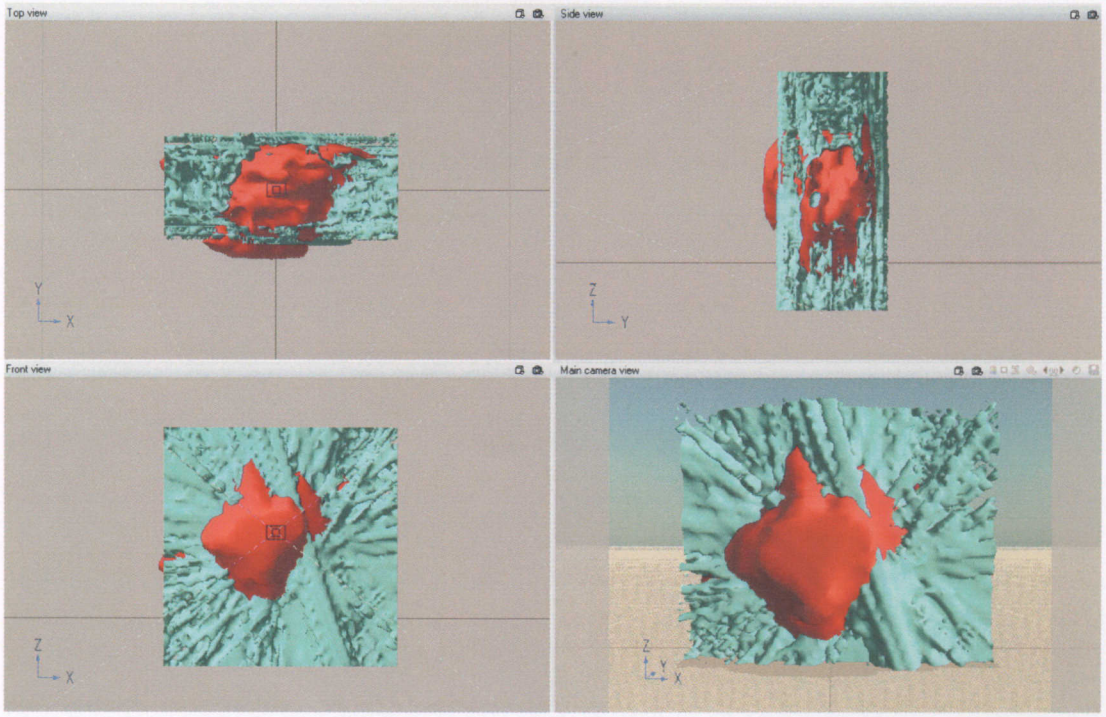

Figure 4-72: Difference mapping of the two models.

For SM 7/6/2005 the effects of the boundary rotation show an important clue into the inherent problem of the reconstructions.

4.6.3 Boundary rotation and re-scaling

The final test case is the random rotation and rescaling of the boundaries. The dataset used can be seen in Figure 4-73.

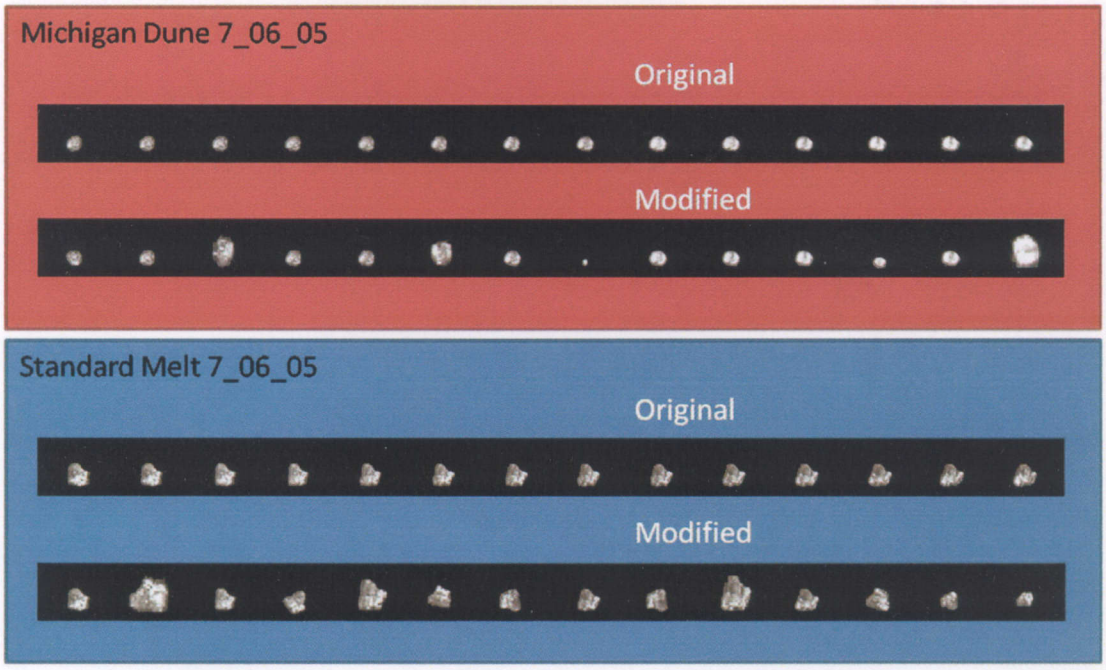

Figure 4-73: Original versus the modified images for the rotation and rescaling test.

Figure 4-74 shows the results of random rotation random rescaling on the MD 7/6/2005.

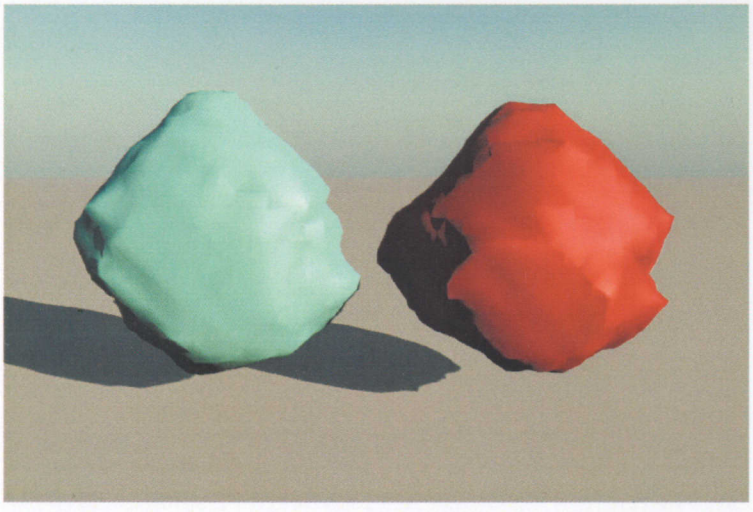

Figure 4-74: MD 7/6/2005 Red- unaltered original model, light blue- rotated-rescaled dataset.

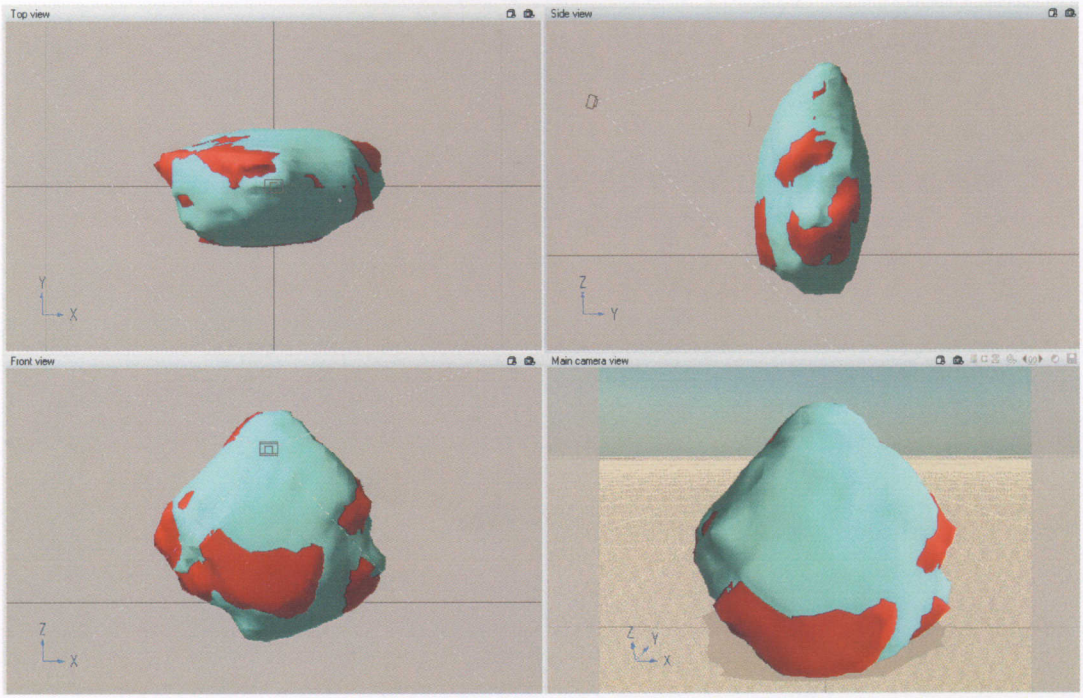

Figure 4-75: Difference mapping of the two models.

As with previous testing the significant altering of the MD 7/6/2005 dataset failed in causing the reconstruction errors seen in the synthesis problem. The results on the Standard Melt, SM 7/6/2005 can be see below in Figure 4-76.

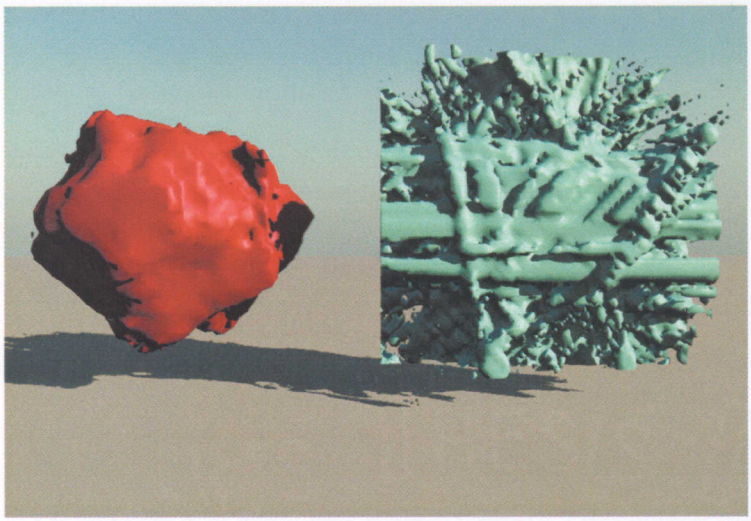

Figure 4-76: SM 7/6/2005 Red- unaltered original model, light blue- rotated-rescaled dataset.

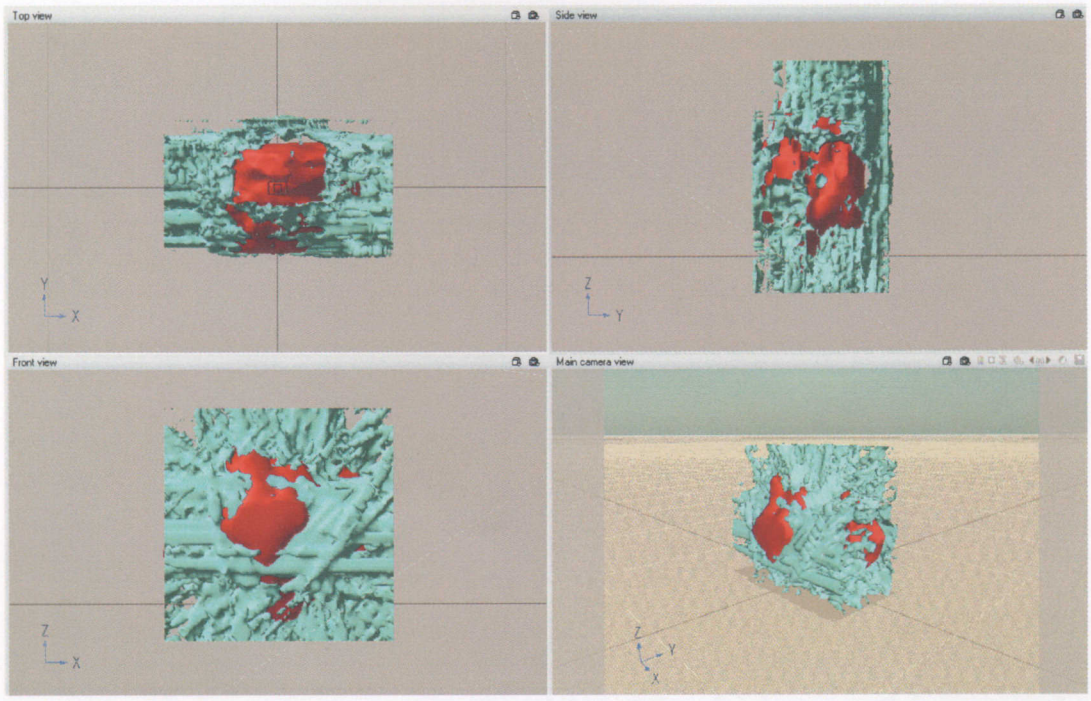

Figure 4-77: Difference mapping of the two models.

As with previous tests the Standard Melt particle again failed in providing a successful reconstruction.

4.7 Discussion of results

The enhanced synthesis procedure showed improvement in the total number of successful reconstructions, specifically in the Daytona Beach mixture where previous work showed for 1 out of 4 reconstructions, the new procedure has increased that number to 3 out of 4. The other mixes had no significant difference in the number of successful reconstructions. Michigan Dune 7/6/2005, was the only particle in the mix to have a successful OM reconstruction. When looking at the images that made up the OT image set, it became clear that the sand particle was much more spherical than the other models

in the mix, which was what prompted the validation tests that would look at the OT dataset. By taking the OT data set, which is known to produce accurate reconstructions, the dataset was altered to induce the scenario seen in the OM dataset, whose particles range in overall size as well as having no specific orientation. The goal was to see whether the selection procedure, being both scale and rotation invariant was the root cause to the failed reconstructions, or whether the aggregate mixtures overall shape characteristics was at fault. The results of the validation test section showed that no matter the size difference in the projections or the rotation of the boundary that the reconstruction would still complete a successful model. This work was validated by aligning the models together to view any difference in the two reconstructions. It was observed that scale provided very little difference in the reconstruction. Conversely, rotation showed a much more significant difference; however, this difference was not large enough to cause a significant disparity when compared to the original. The Standard Melt particle gave the best insight into the reconstruction problem, with all the tests providing complete failures. It was noted in the Michigan Dune scale test that the scale had very little to do with the end result of the model. The primary difference between the Michigan Dune particle and the Standard Melt particle is the angularity of the basic shapes. Figure 4-78, 79 shows a selection of projections from the two mixes.

Figure 4-78: Standard Melt SM 7/6/2005 projections.

Figure 4-79: Michigan Dune MD 7/6/2005 projections.

The jagged edges that are observed are not only contained to the Standard Melt Mixture, and are also the root cause for reconstruction failure. The ART works by creating projections of the cross sections of the particle and was designed to be tolerant to noisy as well as missing data. The problem in the synthesis approach is that there is too much missing data at multiple projection angles. Take for example one of the areas where missing data can occur. Figure 4-80 describes this problem.

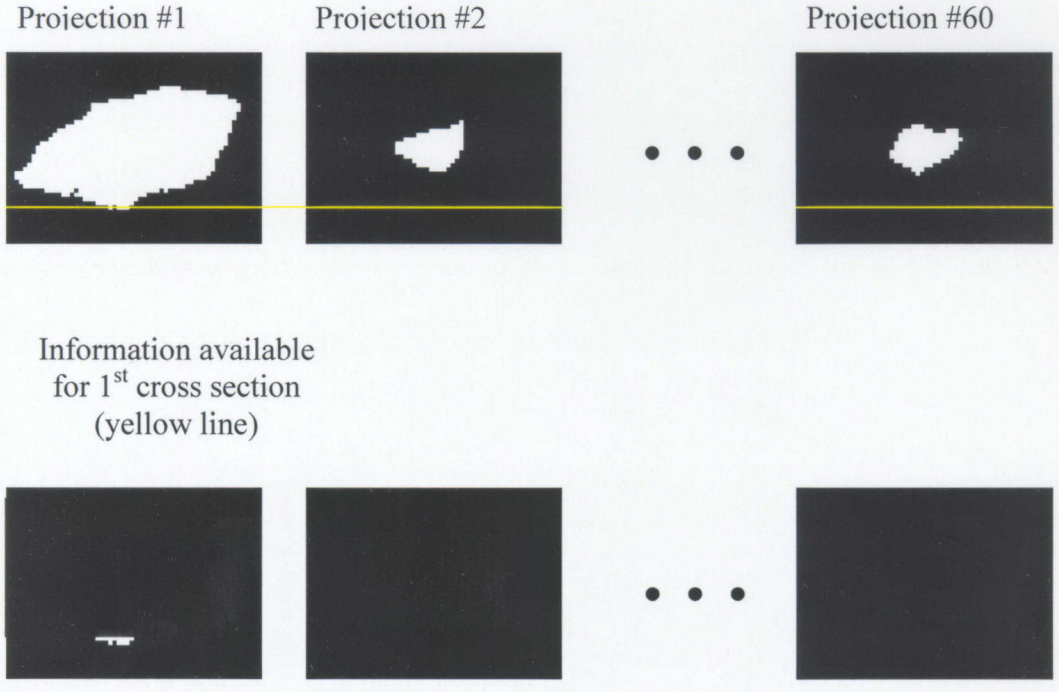

Figure 4-80: Illustration of the lack of information available to ART for the cross section creation.

It can be observed in some failed reconstructions, that ART does succeed in creating proper cross sections in the middle section of the models. This anomaly happens because all models are centered in the preprocessing procedure, so it is more likely that there would be less missing data towards the middle region of the projections, and more missing data the farther you get away from the center. The second problem that the synthesis procedure faces is the information that is located within the angular information of the OT projections. Using Fourier descriptors to find the best boundaries compared to OT projection angles, only gets back a small subset of that data. When looking at an OT projection dataset as seen in its entirety in Figure 4-81, the projections though differing still have continuity between the many angles and any drastic changes occur over time, this however is not the case when a selected set of OM images is observed as in Figure 4-82.

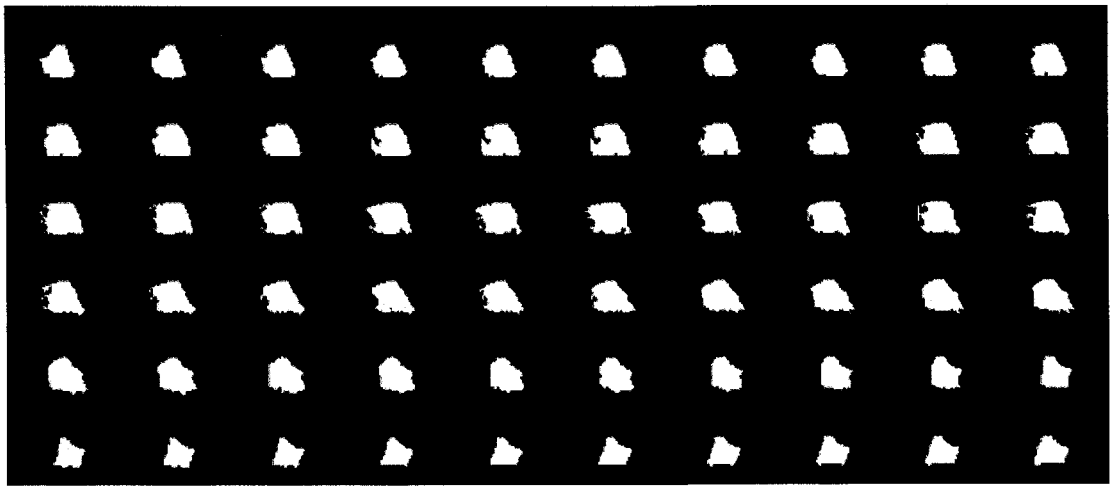

Figure 4-81: OT dataset with images represented at every 6°.

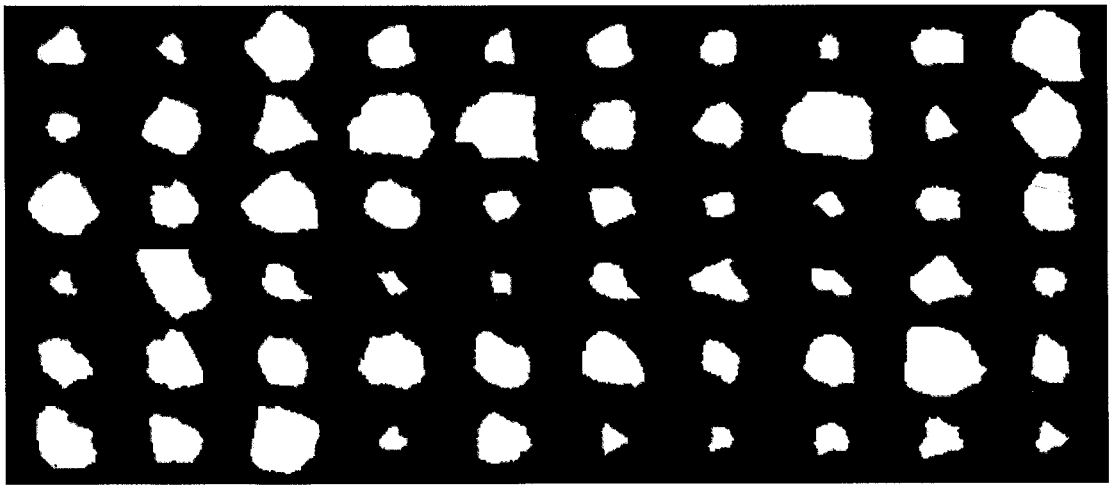

Figure 4-82: OM selected dataset representing the 6° increments of the OT dataset seen in the previous figure.

Notice the large dissimilarities of the overall continuity between the projection angles. Even when there is information at each angle the length of that information can vary much more drastically than what is observed with the OT dataset. The comparison in Figure 4-83 illustrates this important difference.

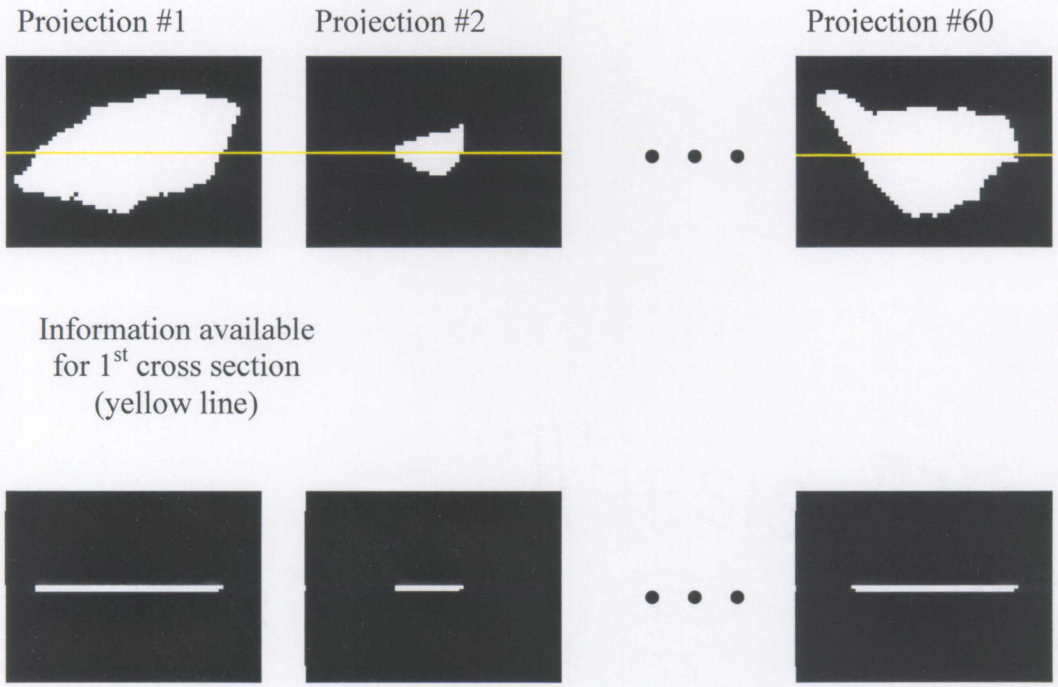

Figure 4-83: Illustration of the lack of information available to ART for the cross section creation (situation #2).

This section was used to illustrate the two situations that cause problems in the reconstruction of 3-D models using ART, when trying to synthesize 3-D composite models which are statistically different from other aggregate composite models.

CHAPTER 5 : CONCLUSIONS

The characterization and synthesis of 3-D shapes are challenging tasks, compared to their 2-D counterparts. When the situation calls for characterizing and synthesizing three-dimensional shapes of a mixture of particles, as is the case in geomaterial aggregates, the problem becomes particularly complex. The only reasonable approaches open to an investigator are to use statistical techniques to characterize the shapes of particle aggregates and a constrained optimization scheme for model synthesis. In this thesis, previously used methods for geomaterial particle aggregate description have been re-validated, and an optimization technique based upon the Euclidean distance metric has been developed and tested for synthesizing 3-D particle models from an assemblage of 2-D optical microscopy and tomography images.

5.1 Summary of accomplishments

The principal accomplishments of this research work include:

1. The design and development of an optical tomography system for capturing 2-D facets of single 3-D particles selected from an aggregate mixture. The design constraints included the size of the particle, its positioning, the magnification of the imaging system, and synchronization of the rotational control and image capture mechanisms.
2. The development of an exhaustive database of optical and X-ray, microscopy and tomography images of particles from the following sand mixtures: Michigan Dune, Standard Melt, Rhode Island, Dry #1, Ala Wai Beach, Kahala Beach and

glass beads (as control). This structured, on-line database is intended to be shared by the research community and can be used as a basis for developing and comparing shape characterization and synthesis algorithms.

3. The re-validation of previously the developed Fourier-descriptor-based 3-D shape characterization technique by exercising it on the enhanced database of geomaterial aggregate mixtures. The "ellipsoid model" continues to provide an indication of the efficacy of the 3-D shape characterization based on a statistical assemblage of 2-D shape descriptors.
4. The design, development and testing of an optimization technique based upon the Euclidean distance metric for synthesizing composite 3-D particle models from 2-D images of multiple particles of a single aggregate mixture. This technique is exercised on the database of sand particles, and the synthesis results are compared with optical tomography and X-ray tomography (the "gold" standard) reconstructions. Both statistical (ellipsoid model) and visual comparisons are made – and information is obtained when the technique succeeds, and perhaps more importantly, when the technique fails to provide a valid reconstruction.

5.2 Conclusions on the use of the optimization technique for particle synthesis

The X-ray and optical tomography methods that are used to synthesize particle models are "true" tomography methods in that actual projective images of single particle are used to reconstruct the original 3-D shape. The optical microscopy images, on the other hand, consist of 2-D images of multiple particles from an aggregate mix scattered on an image

plane. The premise, that these 2-D images have statistically significant shapes and can be used to provide 3-D shape descriptors for the aggregate mixture, has been repeatedly validated. However, the particle synthesis is another matter entirely – since the 2-D images are not the projections from a single 3-D shape. This is not "reconstruction" in the true sense, but a composite 3-D representation of the shapes of all the particles in the aggregate mixture. The situation is further complicated by the fact that the ART algorithm has been chosen as the method for synthesizing this composite shape. As described in a previous chapter, ART requires accurate and explicit measurements of project angles to work correctly. This information does not exist when 2-D images of multiple particles in a statistically homogeneous mixture are presumed to represent the 2-D projections of a single particle. The desire to accomplish this task stems from the fact that optical microscopy is a relatively inexpensive technique compared to optical tomography; X-ray tomography remains prohibitively expensive – hence its designation as a gold standard.

The optimization method based on the Euclidean distance metric for synthesizing a composite 3-D shape intended to be representative of all the 3-D shapes in an aggregate mixture, operates by selecting a subset of the 2-D images of multiple particles in the image plane. The 2-D image subset is constrained to be most representative of 2-D projections from a presumed 3-D particle. The synthesis process for the composite 3-D particles involves ascribing pseudo-angles to selected image subset – the so called "projections."

Results demonstrating the success of this technique are shown to depend on the statistics of the particle mixtures. For those aggregate mixtures that have fairly

homogeneous shapes, the algorithm is successful in synthesizing particles that are similar in shape to the optical and X-ray tomography methods. For particularly angular particles, with a predominant axis of elongation, the method fails to generate any reasonable approximation to the particle shape. The ellipsoid models for such reconstructions are particularly revealing – the lengths of the ellipsoid axis are representative of the statistical similarity of the particle shapes. Longer axes indicate that the particles are more dissimilar. It is to be expected, in such cases, that multiple 2-D images of multiple particles in a mixture, cannot be reasonably expected to provide an estimate of a composite 3-D shape that resembles the individual particles.

5.3 Recommendations for future work

The optimization algorithm could doubtlessly use some improvement in its application. Currently, the minimum Euclidean distance is the chosen constraint – there are numerous other constraints that could be chosen. The optimization method could be varied. Furthermore, optical microscopy images obtained by scattered multiple particles across an image plane do not take into account the preferred directions in which 3-D particles fall. Suspending the particles in a colloid could minimize these effects. However, all of these techniques add cost – either in computational complexity, or hardware for a technique intended to be a simple, inexpensive and effective way of capturing 3-D shape information from an aggregate mixture using optical microscopy. An analysis of the cost-accuracy trade-off would suggest that instead of refining the synthesis technique for optical microscopy, it may be most appropriate to restrict its use for those particle shapes

where the method is shown to be statistically valid. If more accuracy is desired, then optical tomography should be the recommended approach.

All of the techniques explored in this thesis – optical microscopy, optical tomography and X-ray tomography provide a multi-pronged approach towards solving the fundamental problem of characterizing 3-D particle shapes in aggregate mixtures. A judicious application of the relevant method is essential for addressing the application area – the synthesis of 3-D discrete element models of particle mixtures to predict contact forces and ultimately, the shear strength.

REFERENCES

[1] B. Sukumaran, *Study of the Effect of Particle Characteristics on the Flow of Behavior and Strength Properties of Particulate Materials*, Ph.D. Dissertation, Purdue University, 197 p., 1996.

[2] A. Ashmawy, B. Sukumaran, V. Vinh Hoang, "Evaluating the Influence of Particle Shape on Liquefaction Behavior Using Discrete Element Modeling," in *Proc. Offshore and Polar Engineering Conference, 2003,* pp. 542-550.

[3] M. Clark, "Quantitative shape analysis: a review," *Mathematical Geology*, vol. 13, pp. 303-319, 1981.

[4] J. Corriveau, *Three-dimensional Shape Characterization for Particle Aggregates Using Multiple Projective Representations*, Rowan University MS Thesis, 2004

[5] P. Barrett, "The shape of rock particles," *Sedimentology*, pp. 291-303, 1980.

[6] E. Bowman, K. Soga, T. Drummond, "Particle shape characterisation using Fourier analysis," *Geotechnique*, pp. 545-554, 2001.

[7] E. Garboczi, "Three-dimensional mathematical analysis of particle shape using X-ray tomography and spherical harmonics: Application to aggregates used in concrete," *Cement and Concrete Research*, vol. 32, pp. 1621-1638, 2002.

[8] E. Garboczi, N. Martys, H. Saleh, R. Livingston, "Acquiring, analyzing, and using complete three-dimensional aggregate shape information," *Proc. Center for Aggregates Research*, Austin, Texas, April 22-25, 2001.

[9] B. Sukumaran and A. Ashmawy, "Quantitative characterization of the geometry of discrete particles," *Geotechnique* , vol. 51, No. 7, pp. 619-627, 2001.

[10] D. Barrot, *An Algebraic Reconstruction Technique (ART) for the Synthesis of Three-Dimensional Models of Particle Aggregates from Projective Representations*, Rowan University MS Thesis, 2005

[11] J. Boon, D. Evans, H. Hennigar, "Spectral information from Fourier analysis of digitized grain profiles," *Mathematical Geology*, vol. 14, pp. 589-605, 1982.

[12] R. Gonzalez and R. Woods, *Digital Image Processing*, 2nd edition, Prentice Hall, Upper Saddle River, NJ, 2001.

[13] Y. Abu-Mostafa and D. Psaltis, "Image normalization by complex moments," *IEEE Trans. Pattern Anal Mach Intell,* pp. 46-55, Jan. 1985.

[14] F. Sadjadi and E. Hall, "Three-dimensional moment invariants," *IEEE Trans. Pattern Anal. Machine Intelligence*, PAMI-2(2), 127-136, March 1980.

[15] Y. Li, "Reforming the theory of invariant moments for pattern recognition," *Pattern Recognition,* vol. 25, pp. 723-730, 1992.

[16] R. Duda, P.Hart, D. Stork, *Pattern Classification*, 2nd edition, Wiley-Interscience, New York, NY, 2001.

[17] A. C. Kak, M. Slaney, *Principles of Computerized Tomography*, Society for Industrial and Applied Mathematics, 2001, pp49-60, 275-285.

[18] S. Kaczmarz, "Angenaherte auflosung von systemen linearer gleichungen," *Bull. Acad. Pol. Sci. Lett. A*, vol. 6-8A, pp. 355-357, 1937.

[19] K. Tanabe, "Projection method for solving a singular system," *Numer. Math.*, vol. 17, pp. 203-214, 1971.

[20] K. Mueller, R. Yagel, J. J. Wheller, "A fast and accurate projection algorithm for 3-D cone-beam reconstruction with the algebraic reconstruction technique (ART)", *SPIE Medical Imaging Conference, San Diego*, Feb. 1998.